THESIS

AN ALGORITHM FOR ACCURATE IONOSPHERIC TOTAL ELECTRON CONTENT AND

RECEIVER BIAS ESTIMATION USING GPS MEASUREMENTS

Submitted by

Harrison W Bourne

Department of Electrical and Computer Engineering

In partial fulfillment of the requirements

For the Degree of Master of Science

Colorado State University

Fort Collins, Colorado

Spring 2016

Master's Committee:

    Advisor: Yu (Jade) Morton

    Mazdak Arabi
    Sonia Kreidenweis-Dandy
    Frank Van Graas

ABSTRACT

An Algorithm for Accurate Ionospheric Total Electron Content and Receiver Bias Estimation using GPS Measurements

The ionospheric total electron content (TEC) is the integrated electron density across a unit area. TEC is an important property of the ionosphere. Accurate estimation of TEC and TEC spatial distributions are needed for many space-based applications such as precise positioning, navigation, and timing. The Global Positioning System (GPS) provides one of the most versatile methods for measuring the ionosphere TEC, as it has global coverage, high temporal resolution, and relatively high spatial resolution. The objective of this thesis is to develop an algorithm for accurate estimation of the TEC using dual-frequency GPS receiver measurements and simultaneously estimate the receiver hardware bias in order to mitigate its effect on the TEC. This method assumes the TEC in the portion of sky visible to the receiver can be represented as a two dimensional sheet with an absolute value and spacial gradients with respect to latitude and longitude. A code-phase multipath noise estimation algorithm is integrated with the TEC estimation process to mitigate environmental multipath contamination of the measurements. The integrated algorithm produces an approximate map of local TEC using a single dual-frequency receiver while minimizing both multipath induced errors and the receiver hardware bias. The goal of this method is to provide an accurate map of the ionosphere TEC, in the region local to the receiver, without the need for a network of receivers and in the absence of knowledge of the receiver hardware induced bias. This thesis describes the algorithm, its implementation, and attempts to validate the method through comparison with incoherent scatter radar (ISR) data from low, mid, and high latitude locations.

List of Figures

CHAPTER 1

INTRODUCTION AND BACKGROUND

1.1. THE IONOSPHERE

The ionosphere is a region of the upper atmosphere which extends from approximately 50 km to more than 1000 km above the Earth's surface. The ionosphere is distinguished from other regions of the atmosphere because it is ionized by solar radiation, mostly in the UV region of the spectrum [1]. The concentration of free electrons produced by the ionization varies with altitude, location, time of day, season, and amount of solar and geomagnetic activity. Because the ionization is driven by the Sun's radiation, the state of the ionosphere is primarily a function of the intensity of solar input [2].

The ionosphere is considered to be composed of a number of layers, known as the D, E, F1, and F2 regions. Each of these regions covers a certain altitude range and is characterized by the ions which predominate in that region. The D region is the closest to earths surface extending from 60 km to 90 km and primarily contains ions of nitric oxide. At night the D layer becomes almost nonexistent due to the reduction in radiation input, meaning recombination outpaces ionization resulting in a significant reduction in the number of ions and free electrons. Continuing upward, next is the E layer which extends from 90 km to 150 km, and primarily consists of ions of molecular oxygen. Similarly to the D region the E region significantly weakens during the night but is still present at higher altitudes. The F region, from 150 km to more than 500 km, is where the majority of ions and free electrons are present, mostly in the form of atomic Oxygen. During the day the F layer has two distinguishable layers, know as F1 and F2. The F2 layer is the dominant of the two and is present during both the night and day while F1 is only present during the day. The F layer, specifically

F2, has the highest electron density in the ionosphere with the peak density centered around 350 km, which is known as the F2 peak. This region is responsible for the majority of the ionosphere's effect on the propagation of radio waves, reflecting signals in the HF band and below and causing attenuation and propagation delays in higher frequencies. Above the F region the number of free electrons declines exponentially with height. This region is known as the topside, because it is above the F2 peak, and contains ions of lighter elements such as Hydrogen and Helium [3], [4].

The electron density is one of the most important parameters to consider when studying the ionosphere. By measuring the electron density distribution within the ionosphere, pockets of enhanced or depleted ionization and waves propagating through the atmosphere can be detected. Gaining information about these structures, and the large scale changes in electron density, allows for better understanding of space weather which involves Earth's atmosphere, near space, solar activity and Earth's magnetic field, and the interactions between them.

In addition to providing insight into space weather, the study of ionosphere electron content can provide information about storms in the terrestrial atmosphere as discussed in [5] and [6]. Ionosphere disturbances can also be generated by tectonic activity, such as earthquakes and tsunamis, studies of which are presented in [7], [8], and [9]. Ionospheric anomalies have even been observed to occur in advance of earthquakes [10], potentially providing early warning of seismic events. Monitoring of the ionosphere can also be used to detect anthropogenic events, such as large explosions and missile launches, examples of which are presented in [11–13] and [14, 15] respectively.

To make these numerous applications of ionosphere monitoring possible, high accuracy as well as high temporal and spatial resolution estimation of the electron count is required. There are many instruments which can measure electron density such as ionosondes, radars,

sounders on board satellites, rockets, and direct sampling by satellite. However, none has the breadth of coverage provided by GPS.

1.2. IONOSPHERE EFFECT ON GPS

The propagation speed of a radio signal through the ionosphere can be directly related to the number of free electrons along the signals propagation path. Because the focus of this thesis is the effect of the ionosphere on global positioning system (GPS) signals, the discussion of the ionosphere's effect on the signal propagation will be confined to signals in the ultra high frequency (UHF) band which pass through the ionosphere. The signal path can be represented as the total electron content (TEC), which is the number of electrons in a tube of 1 m^2 area extending from the receiver to the satellite. TEC is typically measured in TEC units (TECU) which is 10^{16} electrons per m^2.

$$TEC = \int_S^R n_e(l)dl \tag{1.1}$$

where $n_e(l)$ is the electron density along the signal path which is integrated over the satellite receiver signal path.

The variation in electron density along the signal path results in changes to the refractive index of the medium. The changes over the entirety of the signal path results in the propagation time of the signal being longer than in free space. The increase in propagation time due to the refraction is given by:

$$\Delta\tau = \frac{1}{c}\int_S^R [n(l) - 1]dl \tag{1.2}$$

where c is the speed of light in meters per second and $n(l)$ is the refractive index as it varies along the signal path. The amount of refraction, and therefore propagation delay, of a

signal in the ionosphere is dependent on the frequency of the signal, with lower frequencies experiencing more refraction and higher frequencies less. This means the ionosphere is a dispersive medium for radio frequency (RF) signals, as a glass prism is for light. This fact is important because GPS, like all RF communications, is data modulated on a carrier wave. Because of the modulation, the GPS signal has two refractive indices: one, the phase refractive index (n_p), is for the carrier, and the other, the group refractive index (n_g), is for the modulation [16]. n_g is known as the group refractive index because the modulation can be thought of as being comprised of the superposition of a large group of sinusoids of slightly offset frequencies [1]. The phase refractive index for an RF wave of frequency f approximated to the first order is

$$
\begin{aligned}
n_p &= 1 - \frac{1}{2}\left(\frac{f_p}{f}\right)^2 \\
&= 1 - \frac{e^2}{8\pi^2 m_e \epsilon_0}\frac{n_e}{f^2} \\
&\approx 1 - 40.3\frac{n_e}{f^2}
\end{aligned}
\tag{1.3}
$$

where f_p is the plasma frequency, e is the electron charge, m_e is the electron mass, ϵ_0 is the permittivity of free space, and n_e is the electron density.

From (1.3), the phase delay of a signal, $\Delta\tau_p$, propagating through the ionosphere is

$$
\begin{aligned}
\Delta\tau_p &= \frac{1}{c}\int_S^R [n_p(l) - 1]dl \\
&= -\frac{1}{c}\int \frac{40.3 n_e(l)}{f^2}dl \\
&= -\frac{40.3 TEC}{cf^2}
\end{aligned}
\tag{1.4}
$$

The phase delay of the signal is negative, meaning it is actually an advance, so the carrier is traveling through the ionosphere faster than in vacuum. However, the opposite is true of the

the group delay due to n_g. While the magnitude of the delay is the same, the group delay is an actual delay, not an advance.

$$\Delta\tau_g = \frac{40.3TEC}{cf^2} \tag{1.5}$$

The end result of $\Delta\tau_p$ and $\Delta\tau_g$ in the GPS receiver is that the carrier phase is measured short and the code phase is measured long, which is known as code-carrier divergence. Because GPS receivers use both the code phase and the carrier phase for precise positioning, determining the distance between the receiver and the satellite results in errors in the range estimate due to the ionosphere-induced delays.

The error induced by the ionosphere is the one of the most significant errors in the GPS measurements. This is partially due to the magnitude of the error, which can be up to 36 meters at the zenith (near the equator at the peak of the solar cycle), and the zenith delay is multiplied by an obliquity factor which can be more than three when the satellite is at a low elevation[17]. However, the variability of the ionosphere is really what makes the ionosphere error so problematic. As mentioned earlier, the electron density varies on a diurnal basis, with altitude, with location on the earths surface, with season, and with the solar cycle. In addition, the ionosphere can have short duration variations due to traveling ionospheric disturbances caused by geomagnetic activities, space weather, and other atmospheric wave activities. All these density changes cause variation in the position error of the GPS receiver and can, in extreme cases, result in the receiver losing it ability to track the signal. Because of this, a high performance GPS needs to be designed to have the ability to estimate the ionosphere error [17].

1.3. GPS Electron Content Measurement

As mentioned in the previous section, GPS receivers use the code phase and carrier phase to estimate the range between the receiver and the satellites visible to it. To do this, the receiver compares the time it received the signal to the time imprinted on the signal. To refine the time estimate further, the phase of the code is tracked. The estimated time of flight of the signal derived from tracking the code phase is then used to estimate the range to the satellite, assuming the signal traveled at the free space speed of light. Because the signal actually travels slower in the atmosphere, as discussed earlier, error is introduced in the range measurement. Because the estimate is not the exact geometric range, the measurement is known as the pseudorange, and is described in equation 1.6 below.

Because the code chipping frequency of the civilian GPS signal is only 1.023 Mhz, there is a significant amount of measurement noise in the pseudorange. A far more precise measurement is provided by tracking the carrier phase, equation 1.7, as the frequency of the carrier phase is a thousand times higher. However, the time cannot be stamped on the carrier, as it is on the code, so there is an ambiguity of an unknown number of cycles in the measurement. This means the carrier phase measurement can only provide the change in range since the receiver began tracking the signal. Ideally the receiver would be able to combine the accuracy of the pseudorange measurement with the precision of the carrier phase. Techniques for doing so will be discussed in chapter 2.

$$\rho_{s,f} = r_s + c[\delta t_r - \delta t_s] + T_s + \delta r_s + \epsilon_{\rho,s}$$

$$+ c[b_{r,f} + b_{r,c} + b_{s,f} + b_{s,c}] + I_{s,f} + \tau_{\rho,s,f} + M_{\rho,s,f} + \epsilon_{\rho,s,f}$$

(1.6)

where

$\rho_{s,f}$ = range estimate (pseudorange) for a specific satellite at the frequency f (m)

r_s = true geometric range between the satellite and receiver (m)

δt_r = receiver clock error which is common to all satellites (s)

δt_s = satellite clock error for a specific satellite (s)

T_s = troposphere delay (m)

δr_s = satellite's orbit error projected onto the line of sight (m)

$\epsilon_{\rho,s}$ = other unmodeled errors and noise specific to pseudorange and satellite (m)

$b_{r,f}$ = carrier propagation delay within the receiver hardware (s)

$b_{r,c}$ = code propagation delay within the receiver hardware (s)

$b_{s,f}$ = carrier propagation delay within the satellite hardware (s)

$b_{s,c}$ = code propagation delay within the satellite hardware (s)

$I_{s,f}$ = ionosphere inducted delay (m)

$\tau_{\rho,s,f}$ = antenna delay for specific measurement, satellite, and frequency (m)

$M_{\rho,s,f}$ = multipath error for specific measurement, satellite, and frequency (m)

$\epsilon_{\rho,s,f}$ = other frequency-dependent, unmodeled errors and noise (m)

with subscripts:

ρ indicating specific to the pseudorange measurement

r indicating specific to the receiver

s indicating specific to each satellite

f indicating specific to each signal frequency

c indicating specific to different code modulations

$$\phi_{s,f} = \lambda_f^{-1} r_s + f_f[\delta t_r - \delta t_s] + \lambda_f^{-1}[T_s + \delta r_s] + \epsilon_{\phi,s}$$
$$+ f_f[b_{r,f} + b_{s,f}] - \lambda_f^{-1} I_{s,f} + \tau_{\phi,s,f} + M_{\phi,s,f} + N_f + \epsilon_{\phi,s,f} \tag{1.7}$$

where

$\phi_{s,f}$ = estimated carrier phase (cycles)

λ_f = wave length of the carrier for specified frequency channel (m)

f_f = carrier frequency of specified frequency channel (Hz)

$\epsilon_{\phi,s}$ = other unmodeled errors and noise specific to the carrier phase (cycles)

$\tau_{\phi,s,f}$ = antenna delay specific to carrier phase, satellite and frequency (cycles)

$M_{\phi,s,f}$ = multipath error specific to carrier phase satellite and frequency (cycles)

N_f = integer ambiguity of an unknown constant number of wavelengths between the satellite and receiver (cycles)

$\epsilon_{\phi,s,f}$ = other frequency-dependent, unmodeled errors and noise (cycles)

with subscripts

ϕ indicating specific to the carrier phase measurement

These two equations are extremely important to this thesis, as the measurements they represent are the data primarily used in accurate estimation of the TEC. The notation described above will be used throughout. As is evident from 1.6 and 1.7, there are a large number of error sources which affect the GPS measurements. There are two broad categories of errors, dispersive and non-dispersive. The dispersive errors are those that depend on signal frequency, and are shown on the second line of 1.6 and 1.7, while the non-dispersive do not. This fact will be useful later and is discussed further in section 1.4, which will also deal with some of the errors above in more depth.

As previously mentioned, the delay, or advance, for a signal in the ionosphere is dependent on the frequency of the signal. To allow a GPS receiver to estimate the ionosphere error, the satellites broadcast on more than one frequency band. New, modernized GPS satellites broadcast three carrier frequencies: 1.57542 GHz (known as L1), 1.2276 GHz (known as L2), and 1.17645 GHz (known as L5) [18], [19]. Until recently there were no satellites broadcasting the L5 signal, meaning L1 and L2 are the two frequencies typically used to estimate the propagation delay induced by the ionosphere.

Because of the frequency dependence of the ionosphere delay, the pseudorange and carrier phase measurements from the L1 and L2 signals can be differenced to give a first order estimate of the ionosphere delay. The ionosphere pseudorange error in meters is

$$I_{s,L1} = \frac{f_{L2}^2}{(f_{L1}^2 + f_{L2}^2)}(\rho_{s,L2} - \rho_{s,L1}) \tag{1.8}$$

The TEC is derived in a similar manner and is given by

$$TEC_s = \frac{f_{L1}^2 f_{L2}^2}{40.3\,(f_{L1}^2 + f_{L2}^2)}(\rho_{s,L2} - \rho_{s,L1}) \tag{1.9}$$

While the absolute TEC cannot be derived from the carrier phase due to the integer ambiguity, it can provide a less noisy estimate of the TEC change since the receiver began tracking that particular satellites signal, sometimes called the relative TEC.

$$\Delta TEC_s = \frac{f_{L1}^2 f_{L2}^2}{40.3\,(f_{L1}^2 + f_{L2}^2)}(\lambda_{L1}\phi_{s,L1} - \lambda_{L2}\phi_{s,L2}) \tag{1.10}$$

Equations 1.9 and 1.10 illustrate the basic method by which the TEC along the satellite-receiver signal path may be estimated. However, these estimates still include all the frequency dependent errors illustrated in equations 1.6 and 1.7, and therefore only provide the first step

in obtaining TEC measurements of sufficient quality to be used in the applications discussed in section 1.1.

There is another detail which is important to consider in using GPS derived TEC to study the ionosphere. When studying the electron density of the ionosphere, measurements are generally taken in the zenith direction. However, GPS satellites are only rarely directly above the receiver. This means the GPS signal passes through more than the full thickness of the ionosphere which gives a false representation of the state of the ionosphere. Because of this, it is desirable to convert the satellite path TEC, also known as the slant TEC, to a vertical TEC. The slant TEC can be related to the vertical TEC by

$$TEC(\zeta) = \frac{1}{\cos \zeta'} \cdot TECV \tag{1.11}$$

where ζ and ζ' are the zenith angles of the satellite at the user position and the ionosphere piercing point (IPP), respectively. The IPP is defined as the point where the line of sight path between the satellite and receiver passes through the thin shell approximation of the ionosphere. The thin shell approximation considers the ionosphere to be a sphere with zero thickness at a fixed altitude. The altitude is usually somewhere between 300 and 400 km and is known as the mean ionospheric height. $(\cos \zeta')^{-1}$ is called the obliquity factor, and varies between one at the zenith, and more than three when the satellite is near the horizon. The zenith angle at the IPP is generally not known, so the obliquity factor is written in terms of the zeith angle at the receiver

$$OF_I(\zeta) = \left[1 - \left(\frac{R_E \sin \zeta}{R_E + h_I} \right)^2 \right]^{-1/2} \tag{1.12}$$

where R_E is the radius of Earth and h_I is the mean ionospheric height. Using the obliquity factor, the slant TEC can be converted to the zenith, or vertical, TEC at the IPP

$$VTEC = \frac{TEC}{OF_I(\zeta)} \tag{1.13}$$

The mapping of TEC to $VTEC$ is not a perfect approximation, however, because the ionosphere effects observed in the $VTEC$ are actually spread out across a relatively large area of the ionosphere, but are assumed to describe only the integration of a vertical profile at the IPP. However, the approximation has been shown to be effective, and is widely used in the studying the ionosphere using GPS. By using the $VTEC$ from each satellite visible to a receiver, a two dimensional map of electron density can be created. Additional receivers can be used to increase the number of piercing points, which increases resolution, or if the receivers are more widely spread, they can cover a lager area of the ionosphere. In this way, GPS can provide detailed measurements over wide areas. However, for these measurements to be useful, the ionosphere error must be separated from the other dispersive errors which affect GPS.

1.4. Error Sources

Because we are interested in the TEC, which is calculated by differencing the pseudorange and carrier phase, we will consider only the errors which remain after the difference. From equation 1.6 the differenced pseudorange, $\Delta \rho_s$, is

$$\Delta \rho_s = \rho_{s,L2} - \rho_{s,L1}$$
$$= c[\Delta b_r + \Delta b_{r,c} + \Delta b_s + \Delta b_{s,c}] + \Delta I_s + \Delta \tau_{\rho,s} + \Delta M_{\rho,s} + \Delta \epsilon_{\rho,s} \tag{1.14}$$

The equivalent equation for the carrier phase difference, $\Delta\phi_s$, is

$$\Delta\phi_s = \phi_{s,L1} - \phi_{s,L2}$$

$$= f_f[\Delta b_r + \Delta b_s] - \lambda_f^{-1}\Delta I_s + \Delta\tau_{\phi,s} + \Delta M_{\phi,s} + \Delta N + \Delta\epsilon_{\phi,s} \tag{1.15}$$

ΔI_s is the parameter of interest and must be isolated from the remaining errors. $\Delta\tau_{\rho,s}$ is the difference in antenna delay between the two signals. It can be removed by measuring the delay of the antenna for many angles of signal arrival, but generally good antenna design is relied upon to keep this error small. For this reason, the antenna delay will be neglected in future.

The Δb terms refer to the differences in propagation time of the signals within the transmitting hardware of the satellite and the hardware of the receiver. These biases are very important when attempting to accurately estimate the TEC. There are two types of these hardware biases, the first, which is sometimes called the inter frequency bias (IFB), is the bias between the two signals assuming the codes on both signals are the same. The IFB is part of the error of both pesudorange and carrier phase, however, for the carrier phase, it is generally considered part of the integer ambiguity and therefore ignored. The second, called the differential code bias (DCB), is between than different coding schemes used. Since the DCB is an effect associated with the code, it is not part the carrier phase measurement. The IFB will be further discussed in section 1.4.1 and the DCB in section 1.4.2.

The multipath error, ΔM, is due to the reflection of the GPS signal off of objects nearby the antenna, which creates delayed and attenuated copies of original signal. Multipath affects both the psudorange and carrier phase, but is typically two orders of magnitude smaller for the carrier phase. Because of this, the carrier phase is sometimes used to decrease the effect of pseudorange multipath. However the best defense against multipath is picking an antenna

location devoid of sources of reflection, and designing the antenna to reduce the effect of reflected signals[17]. A more detailed treatment of multipath can be found in section 1.4.3.

The final error term, $\Delta\epsilon$, includes all other errors we are not considering, and noise. The errors included in $\Delta\epsilon$ are small enough that they are not of major concern, and in this thesis they are simply ignored. However, the more errors that are corrected, the better the accuracy that can be achieved, so further work could certainly be done to correct some of the errors present in this term. One error in $\Delta\epsilon$ that will be partially corrected is the noise. In reality, the noise correction is only exchanging the larger noise effect in the pseudorange measurement for the smaller magnitude noise in the carrier phase. This is generally done as part of correcting the multipath, and will be discussed in the same section.

1.4.1. INTER FREQUENCY BIAS. The IFB is the difference in the propagation delay experienced by the two signals within the analog hardware of the satellite and receiver. The IFB does not include differences in the group delays of different codes, and therefore assumes both signals are using the same coding scheme. The satellite IFB, Δb_s, is calibrated before launch by the manufacturer, however, these calibration values are no longer valid once the satellite is in orbit [20–22]. Correction of the satellite IFB is extremely important to accurate estimation, as the range of IFB values across the GPS constellation is around 12 ns, which corresponds to 34 TECu. While this is a large amount of error, it is quite stable. In general IFB estimates vary by about 1 ns, with an average root mean squared (RMS) error of 0.15 ns [23]. Because of this, monthly averaged satellite IFB is sufficient for correcting essentially all of the error.

In order to determine the IFB once the satellite is in orbit the it must be isolated from the ionosphere error and the receiver IFB. This is typically done using a network of receivers

and some model of the ionosphere [22, 24–27]. These networks typically determine satellite and receiver IFB, as well as the ionosphere error. The estimates of the satellite IFB can be obtained from the International GPS Service (IGS) analysis centers. For example, the Center for Orbit Determination in Europe (CODE) University of Berne, Switzerland; Jet Propulsion Laboratory (JPL) Pasadena, CA, USA; European Space Operations Center (ESOC) of European Space Agency (ESA), Darmstadt, Germany; and gAGE/UPC of Polytechnical University of Catalonia, Barcelona, Spain. These processing centers provide the IFBs as part of their global ionosphere map (GIM) products. The data are provided in the form of IONosphere Map EXchange format (IONEX) files[28]. These centers provide global TEC maps with low spatial and time resolution. The objective of this study is to obtain regional TEC maps with high spatial and time resolution. In this thesis, the IFB correction from the CODE processing center will be used, in addition to the GIM maps from JPL, for comparison with the TEC estimated by the algorithm presented here.

The receiver IFB, Δb_r, is typically larger than it is for the satellite and is far more variable than for the satellite. Most of this variation is due to temperature variation of the environment. This includes the temperature of the outdoor components, typically the antenna and some length of cable, as well as the indoor components, the receiver and a second length of cable. The variation in Δb_r due to the temperature is approximately 1 ns. Even after removing the indoor and outdoor temperature variation there is still a variation of a few TECU left[29]. Because of this, it is not possible to reliably calibrate the receiver for IFB. There is also some long term variation in IFB due to receiver aging, but this is not particularly significant. There are receivers which are capable of calibrating a portion of the IFB by generating a signal and using a jumper cable to send it into the receiver, however, this does not capture the effect of the antenna, or the cable between it and the receiver[22].

Because calibrating the receiver IFB is so difficult, the TEC estimation algorithm presented in this thesis simultaneously estimates the receiver IFB. This method will be elaborated upon in section 2.4.

1.4.2. DIFFERENTIAL CODE BIAS. In addition to multiple carrier frequencies, GPS uses a number of modulating codes. The L1 signal has two, one for civilian use, known as the C/A code, and an encrypted one for the military, known as the P(Y) code. Until relatively recently, L2 only had a P(Y) code, and more than half of the currently active GPS satellites still do not have a civilian signal on L2. For this reason many receivers still only use the P(Y) signal on L2. However some, including the receiver used in this thesis, use the civilian code when available and the P(Y) code otherwise. Due to the differences between the civilian and encrypted codes, the group delay within the satellite and receiver hardware is different, therefore a differential bias exists between measurements and must be corrected. This bias exists for both the satellite and receiver. In this case the receiver DCB is neglected, as it is considered to be partially included in the IFB, and the DCB is about a fourth of the IFB magnitude [30]. The satellite DCB, however, is corrected in this work using the values provided by CODE. The satellite DCB range is approximately 3 ns with daily repeatability in the picoseconds[31].

1.4.3. MULTIPATH. Multipath is so called because it refers to the same signal reaching an antenna via multiple paths. The direct line of sight signal is the only desirable one in most applications, so the delayed, and, in general, weaker reflections simply contribute to measurement error. Some resistance to multipath is already designed into the GPS signal, because a reflected signal that is delayed by more than 1.5 chips of the code would be suppressed automatically in the correlation step of the receiver. This delay translates to 500

m of signal path increase for the C/A code and 50 m for the P(Y) code. Typically, however, pseudorange multipath error is between 1 m and 5 m with the carrier phase error around 1-5 cm [17].

Because the carrier phase is far less affected by multipath, and because it is less noisy than the pseudorange measurement, applications of GPS in which precision is required generally attempt to use the carrier phase to compensate for the shortcomings of the pseudorange. One way to do this is by using a hatch filter, or some modified variant as done in [32], [33]. The use of a hatch filter was initially attempted in this work, but was found to perform poorly and was abandoned. Another possible correction method is to simply use the carrier phase measurement instead of the code phase. This relies on estimating the integer ambiguity, which has been a topic of research for some time. Some of the methods for doing this are presented in detailed in [34], [35], and [36]. In this thesis, a method known as the code noise multipath (CNMP) correction is used, which, to an extent, combines the two approaches by using the carrier phase to isolate the multipath and code noise, and then removes them from the code measurement [37–40]. A more detailed description of the CNMP algorithm will be given in section 2.2.

1.5. Prior Research

As previously stated, determination of the TEC using GPS is a relatively widely used technique, and there is a significant amount literature on the subject. This partially stems from the wide variety of methods used to correct the IFB and DCB. There are also a number of techniques used to assimilate the ionosphere measurements from the multiple receivers into an ionosphere map.

The determination of satellite IFB and DCB is generally done in concert with large scale, if not global, mapping of the ionosphere, due to the need to resolve the contribution of the ionosphere from the differential biases. For the most part, the GIM providers do not provide details of their particular implementation. However, there is still a significant amount of literature on using relatively large networks of stations for simultaneous differential bias and TEC estimation. For example in [24], Mazzella uses a network of 16 GPS stations to calibrate the TEC and plasmasphere electron content (PEC) in order to resolve the receiver bias. Earlier, Wilson and Mannucci presented a plethora of work concerning large scale and global TEC determination using the IGS network of receivers [22, 25–27].

These ionosphere mapping techniques are on a far larger scale than the method described here. The focus of this work is a single-receiver TEC mapping and receiver bias estimation method. There are significantly fewer examples of single receiver techniques in the literature. Typically, single receiver TEC and bias estimation is done using some form of polynomial approximation of the ionosphere local to the receiver. Some of these methods consider the TEC over the sky visible to the receiver to be a polynomial with respect to latitude and longitude, as is done in this thesis [28, 41]. However, both of these methods assume the ionosphere is invariant over relatively long periods, at least an hour. These methods do consider higher order spatial polynomials, at least second order, which does partially explain the need for solving over long periods. Some network based TEC mapping methods also use a polynomial approximation of the two dimensional ionosphere map [42–44]. These methods also solve over relatively long periods, assuming the ionosphere does not change.

A significant part of this work is the validation of the estiamted TEC against incoherent scatter radar (ISR) electron density profiles. There are problems with comparing the two data sets because ISR profiles are generally restricted to measuring the ionosphere at altitudes

below 1000 km, while GPS includes electron content from both the ionosphere and the plasmasphere, above 1000 km. In [45], GPS is used in conjunction with ISR data to put the small point which the ISR measures in the context of the broader view of the sky. [46] derives TEC from the ISR and GPS measurements, and makes a direct comparison between the two, in a similar manner to the validation of estimated TEC presented here. In order to make this a direct comparison with the ISR profile, which stops at 1500 km, a numerical model is used to extend the profile to the GPS orbital altitude. The paper also considers the effect of density depletions on both measurements. Because the ISR measurement gives a vertical profile of the ionosphere, but only measures a single point vertically, and GPS measures horizontally but not vertically, the two can be combined to provide a more complete picture of ionosphere structures. The combination of the two measurements is used in [47] to study large scale traveling ionosphere disturbances (TID). GPS and ISR are two complementary instruments for measuring the ionosphere, making comparison between them a natural choice for validating methods of GPS TEC measurements.

1.6. Contributions of Thesis Research

The focus of this thesis is the design, implementation, and testing of a TEC estimation algorithm which simultaneously estimates the zenith TEC above the receiver, the spatial gradient of the TEC with respect to latitude and longitude, and receiver hardware bias from GPS measurements. The objectives of this thesis research are:

- To develop a TEC estimation algorithm which can provide high accuracy measurements of the zenith TEC, and the first order TEC gradients with respect to latitude and longitude from measurements provided by a standard dual frequency GPS receiver.

- To simultaneously estimate the receiver hardware bias in order to find the TEC without the influence of the bias.

- Correct the satellites IFB and DCB using measurements from a GPS monitoring network.

- Mitigate the effect of multipath and code noise on the TEC estimate.

- Apply the estimation method for GPS measurements from receivers at at high, mid, and low latitude locations.

- Evaluate the performance of the estimation method by comparison with simultaneous incoherent scatter radar ionosphere electron density profiles.

1.7. Overview

This thesis is broken into six parts. This chapter introduces the basics of the ionosphere, its effect on GPS, how the TEC may be measured using GPS, and the error contributions which affect this measurement. Chapter 2 outlines the implementation details of the error correct and TEC estimation methods. Results of the TEC estimation are compared with TEC from ISR measurements and GIMs in chapters 3, 4, and 5. These three chapters present results from high, mid, and low latitude locations respectively. The final chapter summarizes the thesis and presents possible directions for future investigation.

CHAPTER 2

Methodology

2.1. Data Collection

As mentioned in section 1.6, GPS data is collected from high, mid, and low latitude locations which are collocated with incoherent scatter radars. These locations are: Poker Flat Research Range (PFRR), outside Fairbanks, Alaska; The National Astronomy and Ionosphere Center (NAIC), outside Arecibo, Puerto Rico; The Jicamarca Radar Observatory (JRO), outside Lima Peru. The sites coordinates are listed in table 2.1. It is important to consider these three latitudes because the ionosphere behaves differently in each. The high latitude ionosphere tends to have smaller TEC values and experiences many small scale density structures and turbulence. The ionosphere in mid latitudes is more stable than in the other two regions with few significant disturbances except during intense solar activity. However, there are regular phenomenas such as the sporadic-E layers typically appear in the night time. Low latitude regions of the ionosphere typically experience the largest electron densities and large scale disturbances. Because these three regions have such different behavior, data from all three is important for proper validation of a TEC estimation algorithm.

TABLE 2.1. Coordinates of GPS receiver locations.

Receiver	Latitude	Longitude	Altitude
Poker Flats Rx	N 65.1187°	W 147.4330°	519.6810 m
Puerto Rico Rx0	N 18.3472°	W 66.7542°	317.7525 m
Puerto Rico Rx1	N 18.4293°	W 66.5802°	61.5975 m
Puerto Rico Rx2	N 18.4873°	W 66.9293°	20.8695 m
Puerto Rico Rx3	N 18.2112°	W 67.1368°	11.5375 m
Jicamarca Rx	S 11.9523°	W 76.8758°	539.3220 m

2.1.1. GPS STATIONS. The GPS stations at PFRR, NIAC, and JRO all utilize the same receiver and antenna for measurement consistency. Each station consists of a PolaRxS PRO multi-frequency, multi-constellation, ionosphere scintillation monitoring receiver (ISM), manufactured by Septentrio, paired with a GPS-703GGG triple-frequency Pinwheel™ GNSS Antenna, manufactured by NovAtel. In this paper only GPS L1 C/A, L2 C, and L2 P(Y) where used but all available constellations and frequencies were collected. The PolaRxS receiver provides pseudorange and carrier phase measurements at 1 Hz sampling frequency as well as the decoded GPS broadcast ephemeris as often as it is updated. The PolaRxS provided a number of other data products however they where not utilized in this research. The exact coordinates of the receivers employed at each site are given in table 2.1.

The data collected at PFRR only included a single receiver. Although three receivers were installed at the Poker Flats only one was operational during the limited time period electron density profiles were being collected by the ISR. In TEC estimation it can be helpful to have an array of receivers to allow the effects of multipath to be distinguished from the effects of ionosphere disturbances. Because multipath should be almost completely different for each unique receiver location, structures in the TEC that are observed on multiple receivers are likely the result of an ionosphere disturbance.

The GPS measurements taken in Puerto Rico were part of a scheduled experiment which specifically collected electron density data from the ISR for comparison with GPS TEC. Data for this experiment was collected from January 24 to 26, 2014. During this time, a temporary array of PolaRxS receivers was installed. Including the permanent receiver at NIAC there where a total of four receivers. The spacing between receivers was relatively large, compared to the Poker Flat array, but they were confined to the northwest side of Puerto Rico. A map which indicates the approximate locations of the receivers can be seen

in figure 2.1. The point label Rx0 refers to the receiver at NIAC which is the reference point for all the receivers.
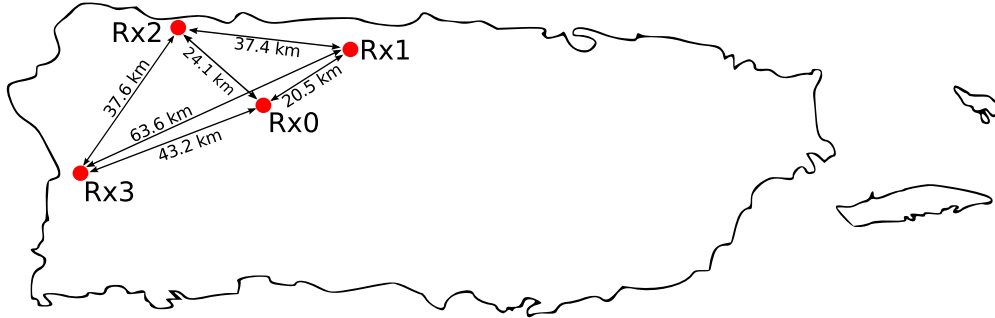

FIGURE 2.1. Approximate locations of receiver array in Puerto Rico.

The receiver at JRO has been collecting data almost continuously since August of 2013. There has only ever been one PolaRxS installed in the vicinity of Jicamrca so no array data is available. As is the case with the two other locations the data periods used were dictated by the availability of ISR data which will be elaborated on in section 2.1.4.

2.1.2. POKER FLAT ISR. ISR measurements at PFRR are provided by the Poker Flat Incoherent Scatter Radar (PFISR), which is an Advance Modular Incoherent Scatter Radar, known as AMISR. AMISR is a modular radar which uses 128 small dipole antennas to form a steerable phased array, capable of steering $\pm$ 25°off the antenna bore sight. AMISR operates between 430 and 450 MHz with a peak power output of 2 MW at 10% duty cycle. The PFISR antenna bore sight is tilted north 16°off zenith and with an azimuth of 15°geographic.

Profiles from PFISR were obtained from Madrigal database from July 2 though 5, 2014 with measurements every 5 minutes, excluding occasional gaps. The Madrigal database can be accessed at http://madrigal.haystack.edu/. The electron density profiles are obtained using long pulse mode, which uses a 330 μs pulse interleaved with 16 baud, 20 μs period alternating code. Measurements are over sampled 10 μs. Profiles from the long pulse mode begin at a range of 120 km and end at 675 km, with a range gate of 24 km. A full profile is

available every 5 minutes. Information concerning the radar mode is provided in the header of the data supplied by the Madrigal database.

For this experiment PFISR made measurements using four beams in different directions using its pulse to pulse steering capability. The beam direction are toward the zenith, along the magnetic field line (elevation 77.50°, azimuth -154.30°), and two outriggers (elevation 66.09°, azimuth -34.69°) and (elevation 65.56°, azimuth 75.03°). In this thesis only the zenith direction profiles are used.

2.1.3. ARECIBO OBSERVATOR ISR. Electron density profiles were obtained using the NAIC 430 MHz ISR between 16:16 January 24 and 15:41 January 26 local time (UTC-4). The interval between radar measurements during these experiments was approximately 17 minutes, although there are two gaps of approximately one hour in the data. The profile altitude range is 116 km to 1712 km with a range gate of 12 km. The radar profiles are taken along 83.5°elevation and zero degrees azimuth. Measurement along the zenith direction is preferred but at the time of this experiment beam steering was not possible as the feed support structure had been damaged by an earthquake shortly before the experiment period. Because this experiment was conducted specifically for comparison with GPS, a special processing method was used to extend the profile above its normal maximum height. Details of the processing method, which are taken from a previous conference paper published by this author [48], are given below.

The ISR data set was obtained using a single radar mode, the so-called topside mode, over the entire altitude range. Another mode is used to measure the plasma frequency in order to calibrate the data. Ionograms are also used for calibration during the night when the plasma line is not available. This is necessary for only a few hours, since photo electrons from the conjugate hemisphere extend the hours during which the plasma line is useful in

local winter. The top side mode has been used for many years, but the analysis from raw data is new, taking advantage of the great increase in computing speed since the previous technique was written.

The mode uses pulses 500 μs in length with center frequencies shifted above and below 430 MHz by 62.5 kHz on alternate pulses. The same 500 kHz receiver channel, centered on 430 MHz is sampled on all pulses, and so noise samples are collected at twice the altitude as would be possible if the frequency shifting were not used. The first step of the digital processing is to make two channels, each 125 kHz wide, centered on the two transmitted frequencies. The filters are very flat at the centers of their pass bands, avoiding any significant distortion of the signal.

The next step is to calculate lag profiles for each relevant delay, accumulate over a sufficient time interval, and invert the profiles using linear regularization. Lag profile calculation and inversion are discussed in [49], most relevant to this analysis, and [50]. The filtering in the process smooths the data in range so that 8 μs sampling rate can be made larger in order to reduce the computing time in the next step.

Finally, a model of the incoherent scatter spectrum is used in an iterative fitting process. The fitting is single height, as described in [49], where the signal to noise ratio (SNR) is high and the free parameters few, but the process extends across range in the topside where there are light ions and the SNR is low. The coupling between ranges is achieved using a smoothing regularization term for each parameter in the chi-square equation, and so the process is best described as non-linear regularization.

2.1.4. JICAMARCA OBSERVATORY ISR. The JRO electron density profiles used here are from March 6-7 and 11-13, 2013 with an interval of approximately 10 minutes between profiles and a number of gaps in measurement. The Jicamarca measurements from the 50

MHz radar were derived from the standard Faraday rotation double-pulse experiment, one of the primary operating modes of JRO. The Faraday rotation double-pulse experiment remains the most suitable for measuring the F region plasma density. The double pulse mode is used for altitudes below 450 km and a long pulse mode is used for altitudes above 450km. The profiles extend from 105 km to 1635 km with a range gate of 150 km.

There is a caveat concerning data from Jicamarca, as the radar is at the magnetic dip equator. These measurements are prone to contamination from coherent scatter from plasma irregularities in the equatorial electrojet and with equatorial spread F. Removal of this coherent scatter is not possible, which results in anomalously large plasma densities in those regions. Because of this, measurements below 140 km must be disregarded, 180 km at midday, as well as night measurements during spread F events, must be disregarded. Further information concerning the operation detail of the JRO experiments can be found in [51–54].

2.2. Code Noise Multipath Correction

To mitigate the effect of multipath and receiver pseudorange noise, a version of the CNMP algorithm is used. A variant of the CNMP method is used by the Wide Area Augmentation System (WAAS) reference stations [37, 38]. The algorithm uses a code minus carrier (CMC) observable to isolate and remove the pseudorange multipath, pseudorange noise, and time variation in the ionosphere delay. Removing these errors from the pseudorange, a bias is introduced which is unknown but may be estimated. In the WAAS implementation of the algorithm, the maximum bias bound is derived solely from *a priori* information on the observed GPS signal characteristics. In the version utilized here, the bias is estimated using time averaging. A bound for this estimate is derived from the multipath signature

25

extracted from the CMC observable[39]. In addition, the ionosphere variation is left in the measurement, as it is the parameter of interest[40].

2.2.1. ALGORITHM DESCRIPTION. The aim of the CNMP method is to exchange the pseudorange noise and multipath for the noise and multipath in the accumulated doppler measurement and bias, which is reducible. The CMC is the accumulated doppler range (ADR), simply the carrier phase, equation 1.7, converted to meters, subtracted from the pseudorange.

$$adr_{s,f} = \lambda_f \phi_{s,f} \tag{2.1}$$

The CMC observable is calculated from equations 1.6 and 2.1

$$
\begin{aligned}
cmc_{s,f} &= \rho_{s,f} - adr_{s,f} \\
&= 2I_{s,f} - \lambda_f N_f + M_{\rho,s,f} - \lambda_f M_{\phi,s,f} + c[b_{r,c} + b_{s,c}] \\
&\quad + \epsilon_{\rho,s} - \lambda_f \epsilon_{\phi,s} + \epsilon_{\rho,s,f} - \lambda_f \epsilon_{\phi,s,f}
\end{aligned} \tag{2.2}
$$

In 2.2, all the components which are common to the pseudorange and carrier phase measurements are removed. The common components which are removed include the geometric range (r_s), the receiver and satellite clock errors $(\delta t_r$ and $\delta r_s)$, the troposphere error (T_s), the satelltie orbit error (δr_s), and the satellite and receiver IFB $(b_{r,f}$ and $b_{s,f})$. While the ionosphere error, $I_{s,f}$, is common, because one is a delay and the other is an advance, it adds instead of cancels. The ionosphere delay is removed from the CMC using the ADR measurements. The L1 and L2 ADR difference used to find the ionosphere error is written

as

$$adr_{s,L1} - adr_{s,L2} = I_{s,L2} - I_{s,L1} + c[\Delta b_r + \Delta b_s] + \lambda_{L1}M_{\phi,s,L1} - \lambda_{L2}M_{\phi,s,L2}$$

$$+ \lambda_{L1}N_{s,L1} - \lambda_{L2}N_{s,L2} + \lambda_{L1}\epsilon_{\phi,s,L1} - \lambda_{L2}\epsilon_{\phi,s,L2} \tag{2.3}$$

From the ADR difference, the ionosphere delay for L1 is calculated as:

$$I_{s,L1} = \frac{f_{L2}^2}{f_{L1}^2 - f_{L2}^2}(I_{s,L2} - I_{s,L1}) \tag{2.4}$$

The ionosphere delay is then removed from the CMC by substituting the result from equation 2.3 into 2.4, and subtracting twice the result from the 2.2 which, for L1, results in:

$$cmc_{s,L1,corr} = \rho_{s,L1} - adr_{s,L1} - 2I_{L1} = -\lambda_{L1}N_{s,L1} - k(\lambda_{L1}N_{s,L1} - \lambda_{L2}N_{s,L2})$$

$$+ \lambda_{L1}M_{\rho,s,L1} - \lambda_{L1}M_{\phi,s,L1} - k(\lambda_{L1}M_{\phi,s,L1} - \lambda_{L2}M_{\phi,s,L2})$$

$$+ c[b_{r,c} + b_{s,c} - k(\Delta b_r + \Delta b_s)] + \epsilon_{\rho,s} \tag{2.5}$$

$$+ \epsilon_{\rho,s,L1} - \lambda_f\epsilon_{\phi,s,L1} - k(\lambda_{L1}\epsilon_{\phi,s,L1} - \lambda_{L2}\epsilon_{\phi,s,L2})$$

where

$$k = \frac{2f_{L2}^2}{f_{L1}^2 - f_{L2}^2} \tag{2.6}$$

Equation 2.5 is defined for L1 as an illustration. The entire CMC correction process is conducted on both the L1 and L2 pseudoranges.

Making this correction removes the ionosphere term at the cost of adding the difference of the L1-L2 integer ambiguity, multipath, receiver and satellite hardware bias, and the other unmodeled errors and noise. These differential errors are all multiplied by k, increasing their effect. However, the integer ambiguity and the hardware biases can be considered constant as long as the receiver maintains signal tracking lock. With this in mind the ionosphere

27

corrected CMC can be rearranged and simplified as follows:

$$cmc_{s,L1,corr} = M_{\rho,s,L1} - (1+k)\lambda_{L1}M_{\phi,s,L1} + k\lambda_{L2}M_{\phi,s,L2}$$

$$+ \epsilon_{\rho,s} + \epsilon_{\rho,s,L1} - (1+k)\lambda_{L1}\epsilon_{\phi,s,L1} + k\lambda_{L2}\epsilon_{\phi,s,L2} + B_{s,L1}$$

(2.7)

where

$$B_{s,L1} = -(1+k)\lambda_{L1}N_{L1} + k\lambda_{L2}N_{s,L2} + c[b_{r,c} + b_{s,c} - k(\Delta b_r + \Delta b_s)] \qquad (2.8)$$

B_S contains all the bias terms which affect the CMC, the estimation of which will be detailed in section 2.2.2. The estimated bias is denoted as $\hat{B}_{s,f}$, and is subtracted from the CMC. Without the contribution of the bias, the most significant components of the CMC are the pseudorange multipath and noise. Therefore, by subtracting the CMC from ρ_s, those errors can be suppressed. The corrected pseudorange is:

$$\rho_{s,L1,corr} = \rho_{s,L1} - cmc_{s,L1,corr} + \hat{B}_{s,L1}$$

$$= r_s + c[\delta t_r - \delta t_s] + T_s + \delta r_s + c[b_{r,L1} + b_{r,c} + b_{s,L1} + b_{s,c}] + I_{s,L1}$$

$$+ (1+k)\lambda_{L1}M_{\phi,s,L1} - k\lambda_{L2}M_{\phi,s,L2} + (1+k)\lambda_{L1}\epsilon_{\phi,s,L1} - k\lambda_{L2}\epsilon_{\phi,s,L2}$$

$$- B_{s,L1} + \hat{B}_{s,L1}$$

(2.9)

Upon examination, equations 1.6 and 2.9 show that the pseudorange noise and unmodeled errors, both frequency depended and independent, as well as the pseudorange multipath error are removed. However, they are replaced by amplified carrier phase multipath, noise, and unmodled errors from both L1 and L2, as well as bias estimation errors from $\hat{B}_{s,L1} - B_{s,L1}$.

Figures 2.2 and 2.3 , 2.4, 2.5, 2.6, and 2.7 show examples of the slant TEC before and after CNMP correction from receivers at Poker Flat, Arecibo and Jicamarca respectively. These plots also include the difference between the corrected and uncorrected TEC. The

difference should be almost zero mean, as only noise and multipath should be absent from the corrected measurement. However, the multipath is not always zero mean, especially over the short term. The first plot from each location shows an example of a case where the difference is close to zero mean, and the second shows an example of when the difference is relatively far from zero mean. Each plot shows the mean of the difference in the legend. Even in the worst cases, the discrepancy is relatively small, less than 5 TECu, and does not appear to be a systematic bias indicating bias estimation is operating properly. As can be seen in 2.4, 2.5, and 2.6, the TEC sometimes drops below zero, which is impossible and is due to a combination of the receiver and satellite hardware biases. This is because TEC shown in these plots is not a final product, and is presented only as an illustration of the operation of the CNMP correction. This set of satellites were chosen simply because they seemed to provide best illustration of how the correction operates, and including all 31 plots for each location seemed excessive. The satellites are indicated by their pseudorandom noise number (PRN number), which uniquely identifies the code used by a particular satellite, and is generally used to differentiate GPS satellites.
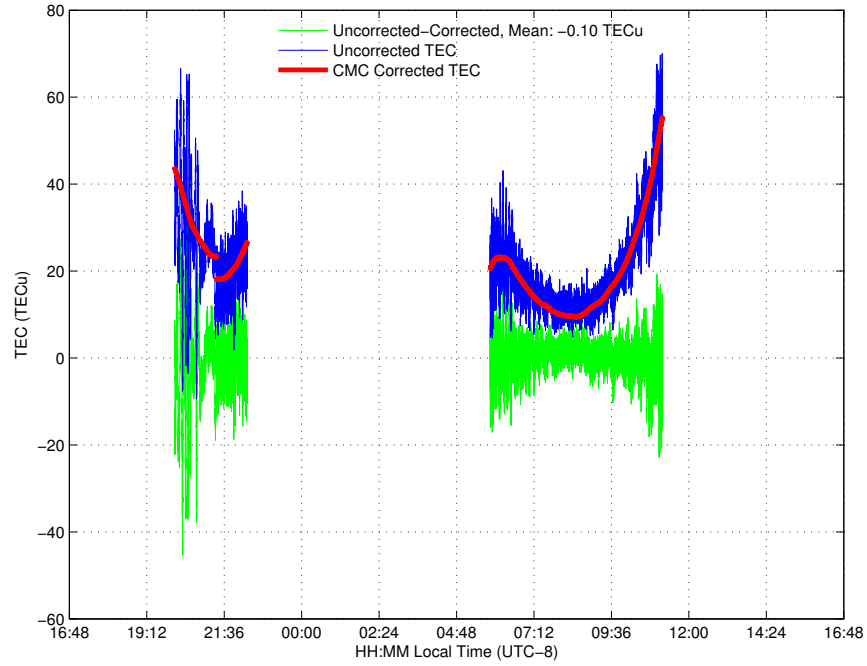
FIGURE 2.2. Slant TEC before (in blue) & after (in red) CMC correction. Difference between corrected and uncorrected (in green) should be zero mean. Data from Poker Flat, Alaska, July 5, PRN 7.
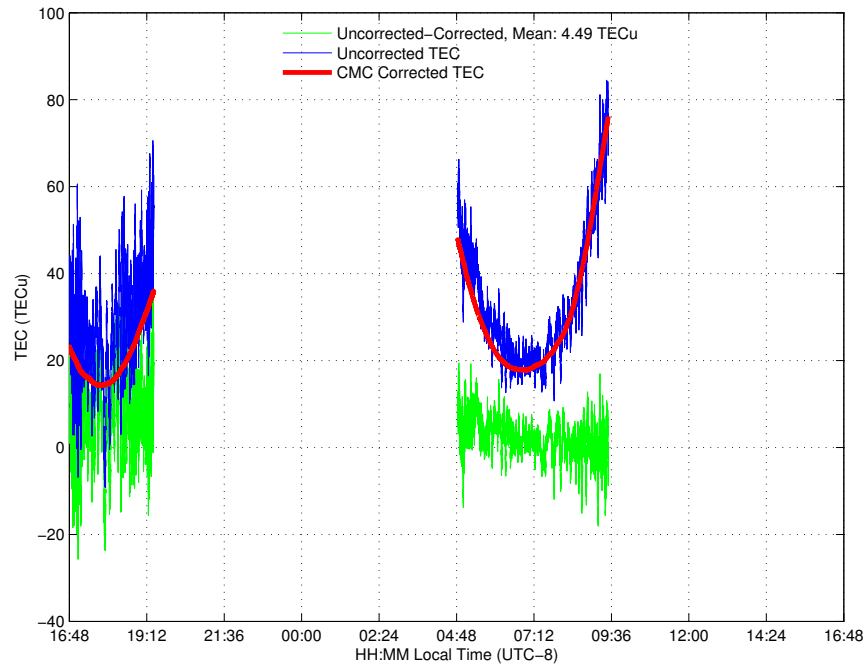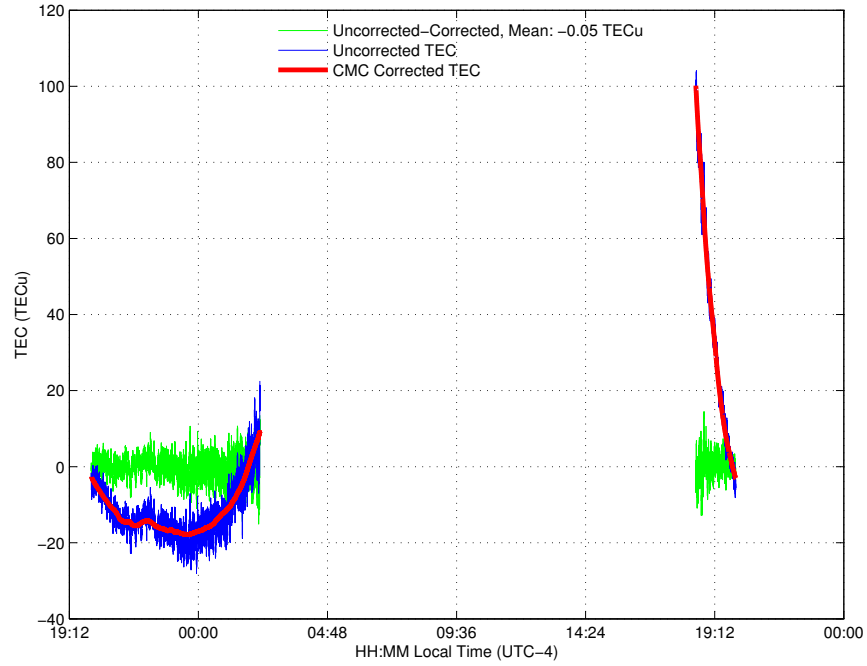

FIGURE 2.3. Slant TEC before (in blue) & after (in red) CMC correction. Difference between corrected and uncorrected (in green) should be zero mean. Data from Poker Flat, Alaska, July 5, PRN 10.

FIGURE 2.4. Slant TEC before (in blue) & after (in red) CMC correction. Difference between corrected and uncorrected (in green) should be zero mean. Data from Arecibo, Puerto Rico, January 24, PRN 16.
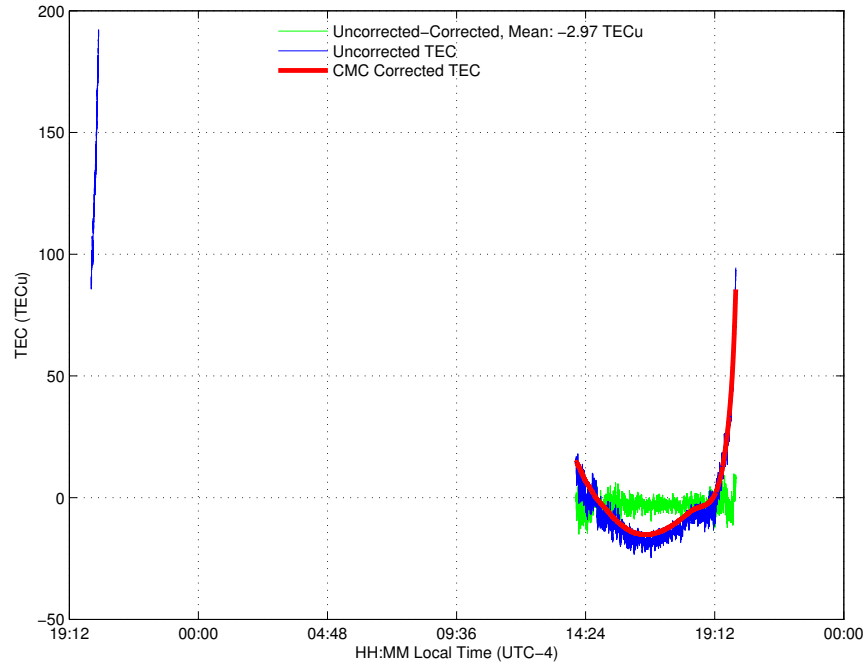

FIGURE 2.5. Slant TEC before (in blue) & after (in red) CMC correction. Difference between corrected and uncorrected (in green) should be zero mean. Data from Arecibo, Puerto Rico, January 24, PRN 22.
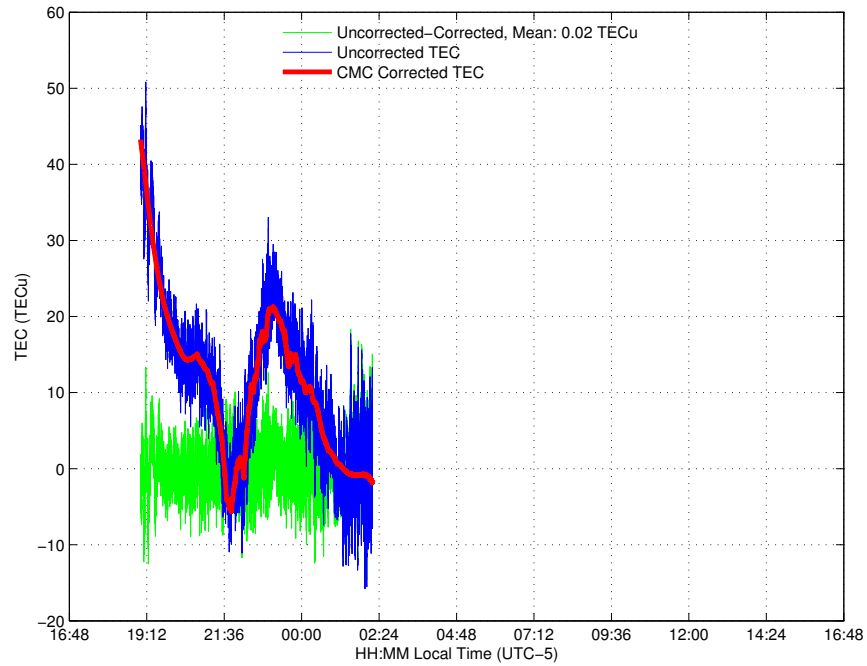
FIGURE 2.6. Slant TEC before (in blue) & after (in red) CMC correction. Difference between corrected and uncorrected (in green) should be zero mean. Data from Jicamarca, Peru, March 7, PRN 20.
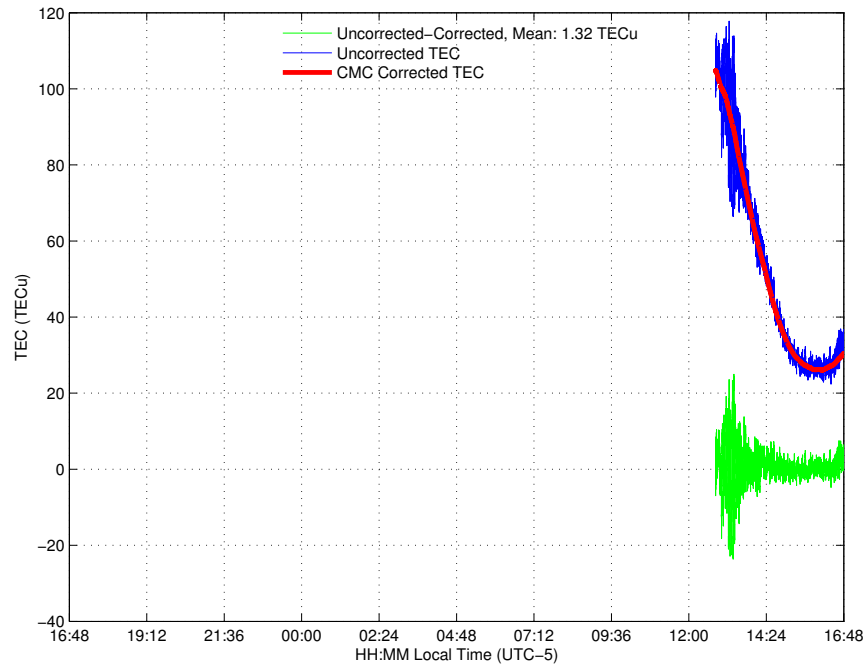

FIGURE 2.7. Slant TEC before (in blue) & after (in red) CMC correction. Difference between corrected and uncorrected (in green) should be zero mean. Data from Jicamarca, Peru, March 7, PRN 22.

2.2.2. BIAS ESTIMATION. The term $B_{s,f}$, from equation 2.8, represents the carrier phase ambiguity terms and the hardware biases from equation 2.5. Other than the bias, the terms left in the CMC observable are the multipath, frequency dependent and independent noise, and unmodeled errors. Because these terms are essentially noise, the bias can be estimated as the average over a window of n seconds. The window size, n, is determined by the multipath fading period, which will be discussed in more detail later. The bias estimation is given by the following:

$$\hat{B}_s(k) = \frac{1}{n+1} \sum_{i=k-\frac{n}{2}}^{k} CMC_{s,corr}(i); k = \left[0 + \frac{n}{2}, m - \frac{n}{2}\right] \tag{2.10}$$

Figure 2.8 illustrates how the bias estimation is made from the CMC over a continuous measurement period without cycle slips. Because of the windowed estimation, the first bias estimate, starting from the beginning of the data period, can be made at $\frac{n}{2} + 1$ seconds and the last at $k - \left(\frac{n}{2} + 1\right)$. To keep the data length consistent, the bias before the first estimate is set equal to the first estimate and the last estimate is treated similarity, as illustrated in figure 2.8.

To determine the which of the bias estimates is most representative of the true bias, in that it includes only the contributions shown in equation 2.8, an error bound on the bias estimate, $\hat{B}$, is also estimated. This is done by low-pass filtering the CMC to remove the high frequency multipath components. The bandwidth of the filter is $\frac{1}{n}$ Hz thereby leaving only the components which would appear as constant biases within the n second averaging window used for the bias estimation. The resulting filtered CMC, $CMC_{corr,filt}$, is then used to calculate MP_{bound} in a similar fashion to the bias estimation method. The n second window is used again, but instead of calculating the average of the window, the range of the values within the window is found. This range is the bound. The best $\hat{B}$ occurs where MP_{bound} is the smallest, in other words, where the error effect is the smallest.
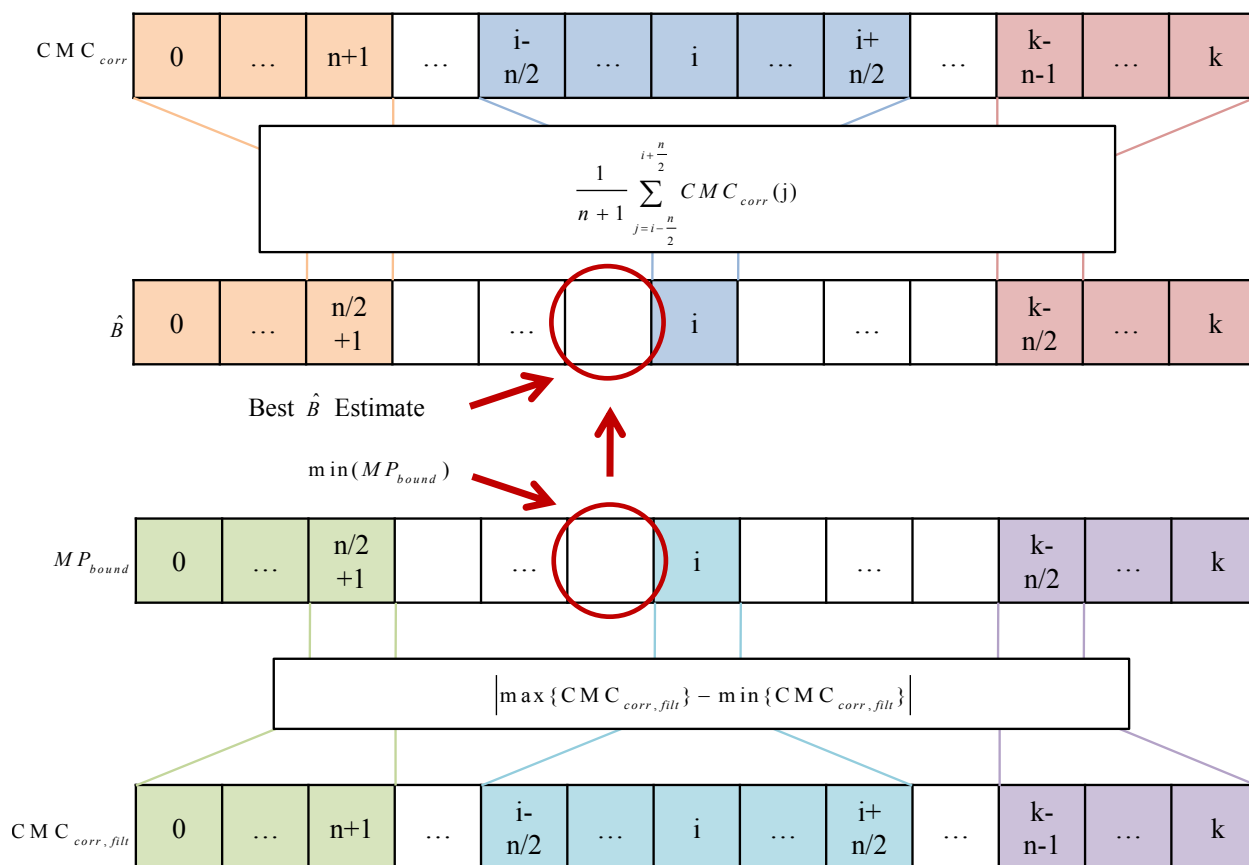
FIGURE 2.8. Basic algorithm for estimating the bias and the error bound on that bias, as well as finding the best bias estimate from the bound.

The best bias estimate can then be applied to the entire period of data where continuous phase tracking is maintained. This obviously assumes no need to operate in real time. While it is possible for all aspects of this TEC estimation method to be made compatible with real time operation, this thesis is focused on post processing only. The advantage that post processing provides is the best bias estimate can be applied to the entire data period making for a much nicer result.

The MP_{bound} is in fact a bound on the multipath error, but because it is the most variable component left in the CMC, it can be considered a bound on the bias estimate. A more rigorous formulation of the bound is given in [39], but for the purpose of this thesis research only the MP_{bound} is considered. If in future there is interest in using the bound

for measurement weighting, or to provide an error bound on the final TEC measurement, a more detailed bound formulation will be needed.

In addition to using a simplified bounding method, as compared to [39], this implementation of bias and bound estimation does not make allowances for real time operation. As is evident from figure 2.8 the assumption is made that all past and future data is available at each epoch. It would be possible to implement the windowed method in the same way in a real time situation using a buffer, however, this would significantly delay the time when the first bias estimate could be used. In the real time implementation, an initial maximum bound would be set, and a new tighter bound would not be set until n seconds of data had been collected. During this initialization period, the bias estimate would be made using all the data available up to that point. Further discussing of the real time implementation can be found in [39].

As mentioned earlier, the length of the window used to calculate $\hat{B}$ and MP_{bound} is related to the multipath fading period, derived from the fading frequency which is obtained by differentiating the path delay and converting the units to hertz.

$$f_{fading} = \frac{2h\dot{\theta}}{\lambda} \cos(\theta) \tag{2.11}$$

Based on this, a conservative window length, n, of 1000 seconds was chosen. Further investigation of the multipath fading period is necessary, as the above window length is based purely on [39]. Because the path length is based on the environment surrounding the antenna, it is difficult to determine exactly. However, analysis of the frequency components of the CMC might yield a more precise idea of the maximum fading frequency of the multipath.

2.2.3. CYCLE SLIP DETECTION. In order to estimate the bias accurately, the carrier phase must be continuously tracked with no jumps in the integer ambiguity. Every time one of these jumps, known as a cycle slip, occurs, the $\hat{B}$ and MP_{bound} must be reestimated. For this reason, use of the CNMP algorithm requires some form of cycle slip detection to be implemented. In this case, a relatively simple method was used which uses the rate of change of the L1-L2 ADR difference, $\Delta\dot{adr}$. In a similar manner to the windowed method used in estimating the bias and bound, the windowed mean and standard deviation are calculated for $\Delta\dot{adr}$. The mean, plus and minus 10σ, is used as the bound, with any value of the $\Delta\dot{adr}$ outside of the bounds being considered a cycle slip. The 10σ threshold was settled upon heuristically.

Representative examples of the operation of the cycle slip detection method are shown in figures 2.9, 2.10, and 2.11. Each figure shows the cycle slip main components which are used in the detection for three different satellites. The cycle slips are evident as sudden jumps in the L1-L2 ADR difference and in the detection limits.
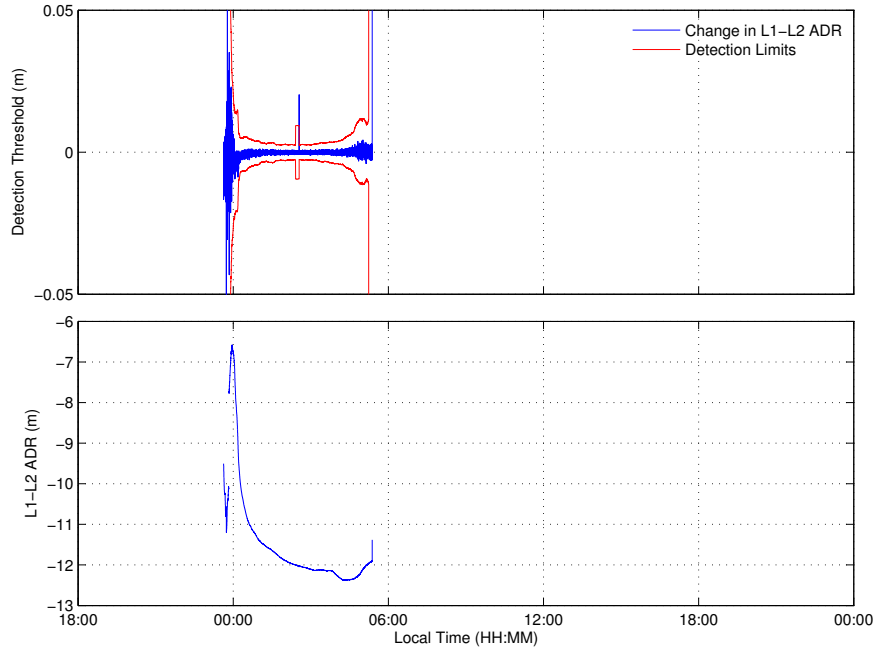
FIGURE 2.9. PRN 1, cycle slip detection operation example. The red traces indicate the 10σ detection thresholds around the L1-L2 ADR rate of change. The lower portion of the plot shows the L1-L2 ADR difference to illustrate the cycle slips. Data from Puerto Rico Rx0, Jaunary 23, 2015.
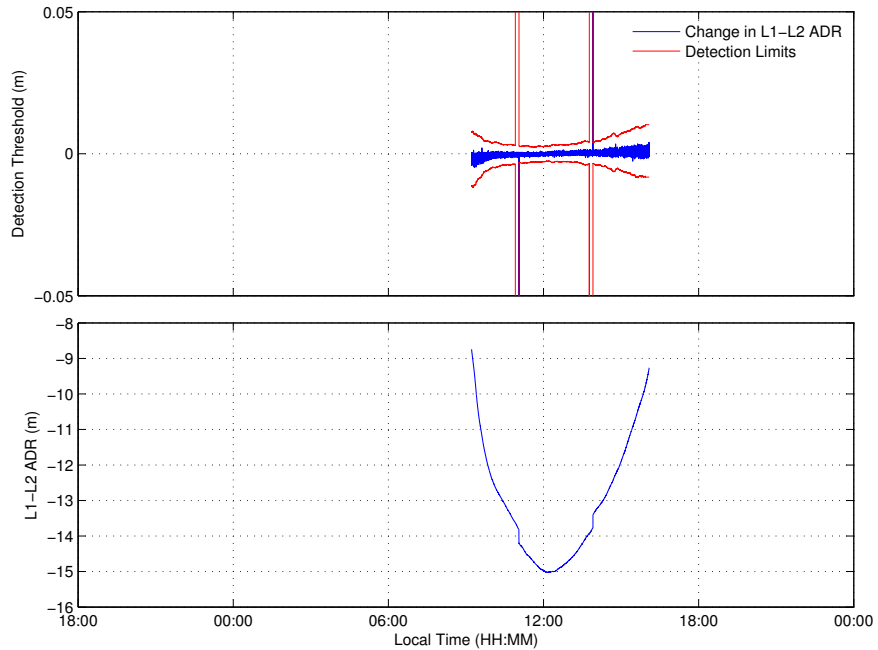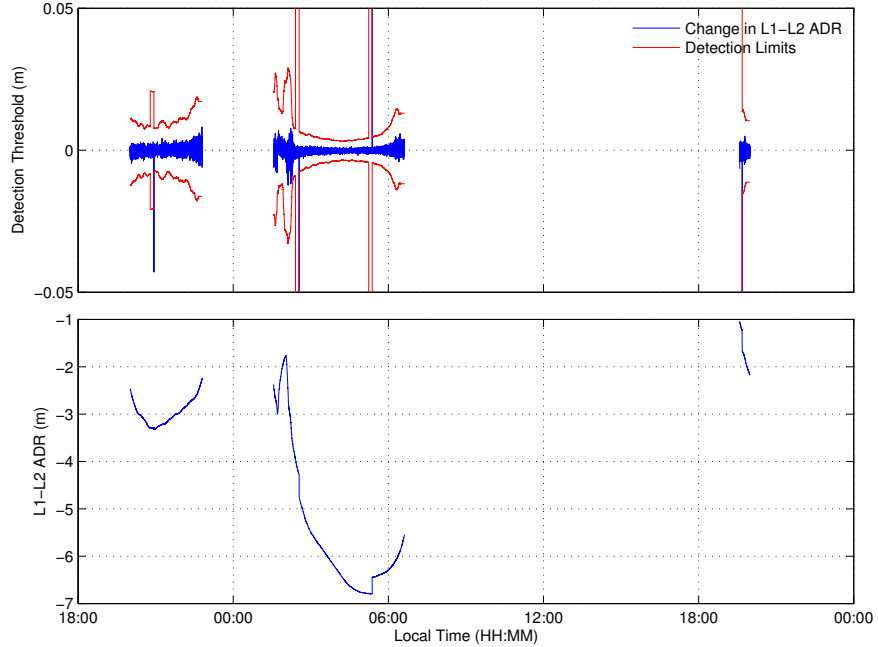

FIGURE 2.10. PRN 15, cycle slip detection operation example. The red traces indicate the 10σ detection thresholds around the L1-L2 ADR rate of change. The lower portion of the plot shows the L1-L2 ADR difference to illustrate the cycle slips. Data from Puerto Rico Rx0, Jaunary 23, 2015.

FIGURE 2.11. PRN 20, cycle slip detection operation example. The red traces indicate the 10σ detection thresholds around the L1-L2 ADR rate of change. The lower portion of the plot shows the L1-L2 ADR difference to illustrate the cycle slips. Data from Puerto Rico Rx0, Jaunary 23, 2015.

2.3. SATELLITE HARDWARE BIAS CORRECTION

The satellite IFB and DCB are corrected using measurements made by the Center for Orbit Determination in Europe (CODE). These measurements are provided on a daily bases for the IFB, but only monthly for the DCB. The daily IFB files can be found at ftp.unibe.ch/aiub/BSWUSER50/ORB/. The files are in Bernese format, which is the product of the Bernese GPS processing software suite, fully described in the Bernese GPS software manual [55]. A comprehensive description of the data organization and naming scheme within the BSWUSER50 directory of the FTP server can be found in [56].

In this thesis work however, only the monthly IFB and DCB products are used, as the variation in satellite hardware bias is small as discussed in sections 1.4.1 and 1.4.2. In addition, the DCB corrections seem to be available only monthly. The monthly bias products are found at ftp.unibe.ch/aiub/CODE/. The naming conventions and organization

are similar to those described in [56]. Correcting the satellite hardware biases is a a trivial procedure outlined by:

$$\Delta\rho_{s,corr} = \Delta\rho_s - c[\Delta\hat{b}_s + \Delta\hat{b}_{s,c}] \tag{2.12}$$

where $\Delta\hat{b}_s$ and $\Delta\hat{b}_{s,c}$ are the CODE estimates of satellite IFB and DCB respectively. The DCB term is only applied when the receiver is using the L1 C/A and L2 P(Y) signals. If the receiver is using L1 C/A and L2 C only the IFB term is needed.

Figures 2.12, 2.13, and 2.14 show the slant TEC for each satellite uncorrected, GPS broadcast bias corrected, and CODE estimation corrected for satellite hardware bias, respectively. The telling difference between the uncorrected and corrected TEC is how well the minimum TEC for each satellite agree with each other over a window of approximately two hours. As can be seen in 2.12, when uncorrected, the TECs for each satellite agree poorly. However, the difference between broadcast and CODE corrections is less apparent. The higher accuracy of the CODE correction can be seen especially around 19:00 and 7:00 universal time (UTC). Figures 2.15, 2.16, and 2.17 make a more direct comparison between the uncorrected TEC and the two corrections, using data from Alaska, Puerto Rico, and Peru respectively. From these graphs, it is evident that correction of the satellite IFB and DCB is important for accurate TEC estimation. In addition, the CODE correction provides a better product than the broadcast estimates. However, these plots also show that there is still a significant bias remaining. This is the receiver hardware bias and its mitigation will be discussed in section 2.4.
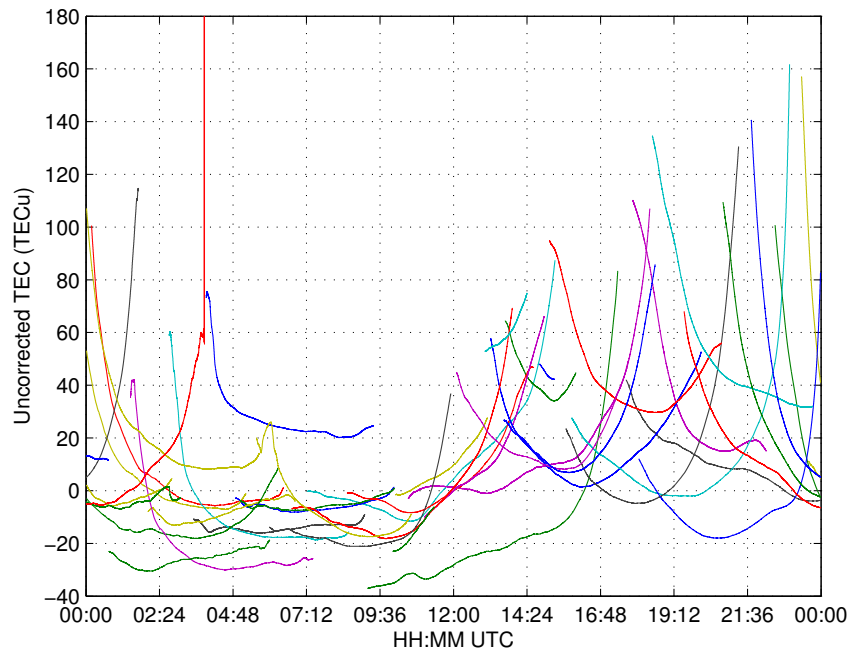
FIGURE 2.12. Slant TEC without correction for satellite IFB or DCB. Each color represents a different satellite. Data from Puerto Rico Rx0, January 24.
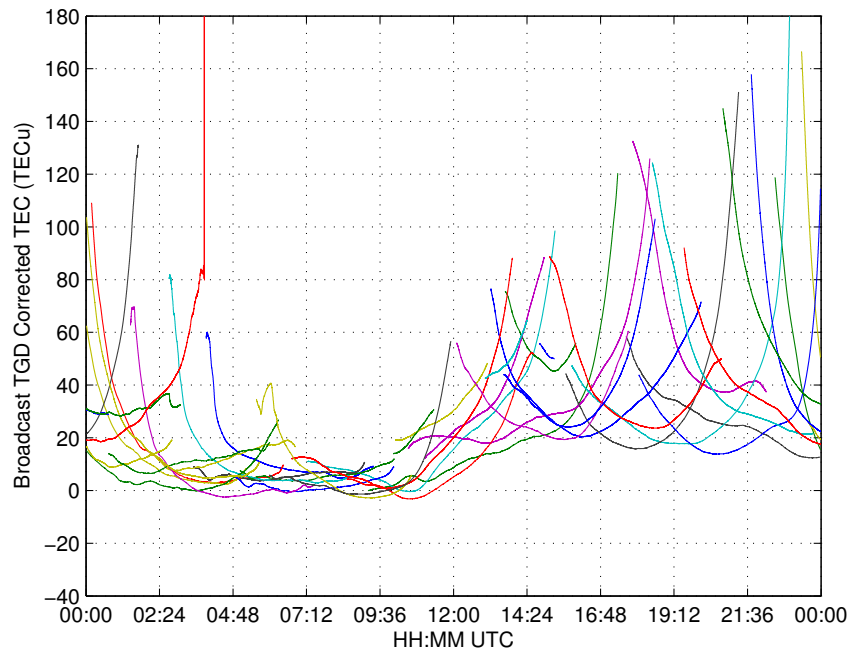

FIGURE 2.13. Slant TEC corrected with GPS broadcast satellite bias correction. Each color represents a different satellite. Data from Puerto Rico Rx0, January 24.
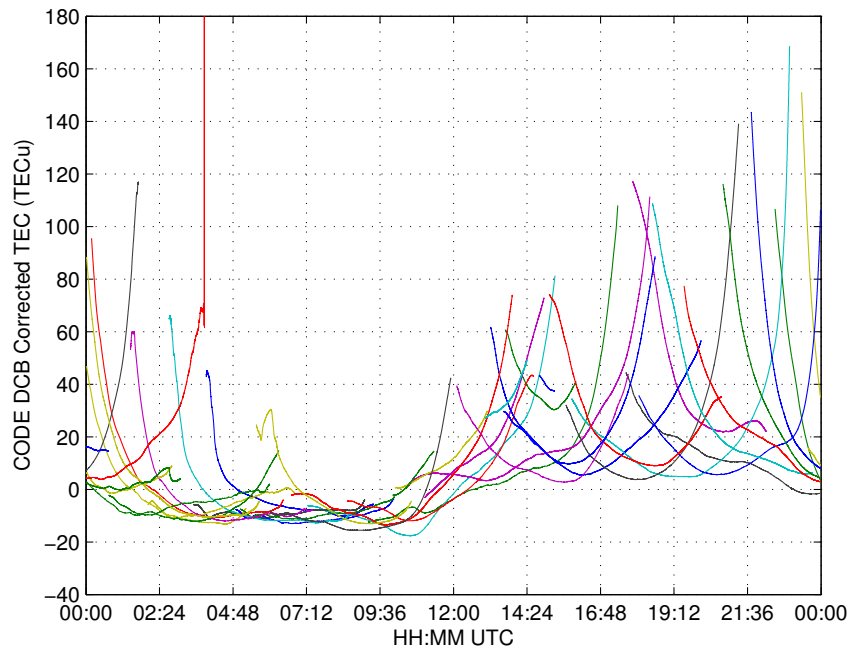
FIGURE 2.14. Slant TEC corrected with CODE estimated satellite bias correction. Each color represents a different satellite. Data from Puerto Rico Rx0, January 24.
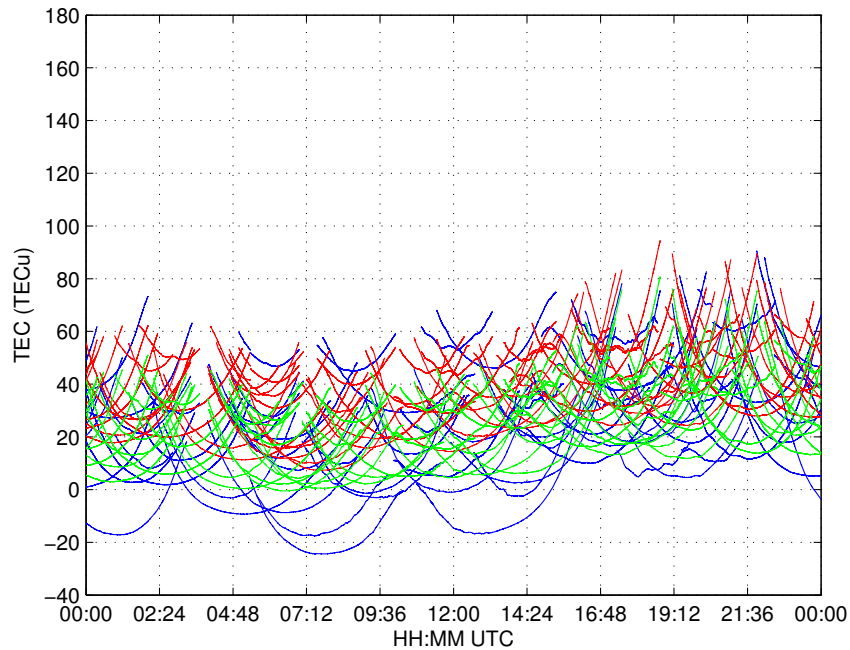

FIGURE 2.15. Comparison between TEC with uncorrected (blue), broadcast corrected (red), and CODE corrected (green) satellite hardware bias. Data from PFRR, July 5.
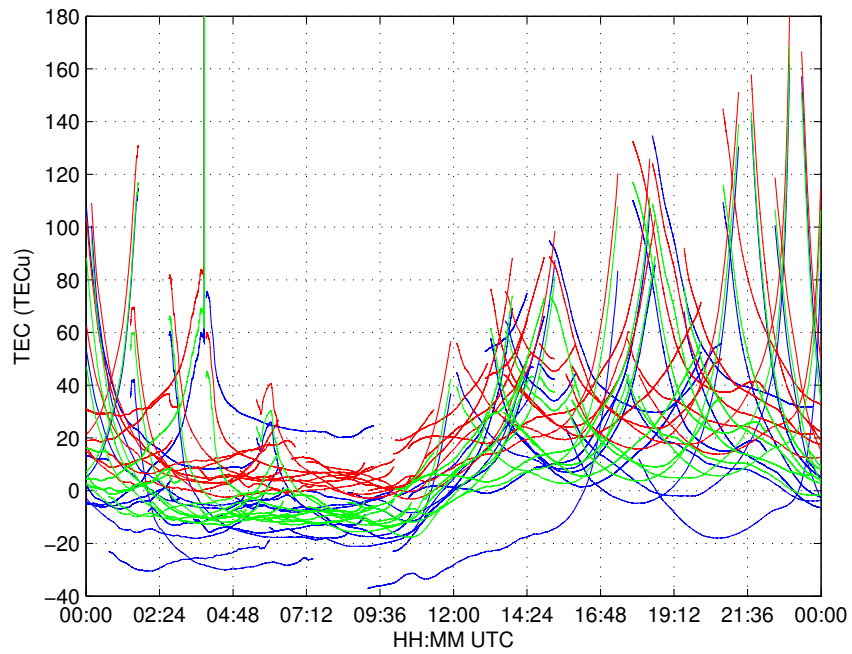
FIGURE 2.16. Comparison between TEC with uncorrected (blue), broadcast corrected (red), and CODE corrected (green) satellite hardware bias. Data from Puerto Rico Rx0, January 24.
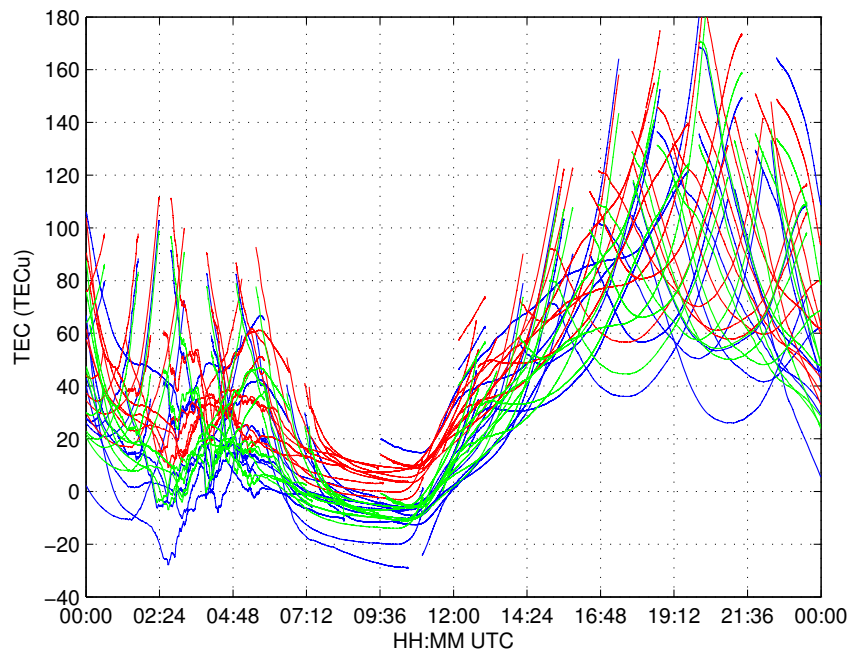

FIGURE 2.17. Comparison between TEC with uncorrected (blue), broadcast corrected (red), and CODE corrected (green) satellite hardware bias. Data from Puerto Rico Rx0, March 7.

2.4. TEC and Receiver Hardware Bias Estimation

Through the error mitigation techniques presented in previous sections, a significant portion of the errors which affect the dual frequency GPS TEC measurement have been eliminated. By returning to equation 1.14 and eliminating the corrected errors the differential pseudorange becomes:

$$\Delta\rho_{s,corr} = c\Delta b_r + \Delta I_s + \Delta\epsilon_{s,corr} \tag{2.13}$$

The only errors remaining are the differential receiver frequency bias, the differential ionosphere error and the unmodeled error and noise term. However, this ϵ term is different from the one in 1.14. It simply contains the difference between the L1 and L2 amplified carrier phase multipath, noise, and unmodeled errors and bias estimation errors introduced by the CNMP correction, as the other contributions were removed by that same correction. The receiver DCB term has also been dropped because, as discussed in section 1.4.2, it is not significant. In this section the algorithm by which the final two terms, excluding $\Delta\epsilon_{s,corr}$, in 2.13 may be estimated is outlined.

The algorithm used to estimate the TEC and hardware bias considers the ionosphere error, I_s, for each satellite-receiver path to be approximated by:

$$I_s = I_{s,v} \cdot OF_I(\zeta) \tag{2.14}$$

$$I_{s,v} = I_0 + \frac{\partial I_{s,v}}{\partial\phi}\Delta\phi_s + \frac{\partial I_{s,v}}{\partial\lambda_s}\Delta\lambda + O(I_{s,v}) \tag{2.15}$$

where $I_{s,v}$ is the vertical ionosphere value at the IPP, $OF_I(\zeta)$ is the obliquity factor discussed in section 1.2, and I_0 is the ionosphere error on the path which extends from receiver antenna toward an imaginary GPS satellite fixed at the zenith. ϕ and λ are the IPP latitude and longitude respectively, and $\Delta\phi$ and $\Delta\lambda$ are the latitude and longitude difference between

the piercing point and the receiver position. The last term in 2.15 represents higher order spatial derivatives which are not considered here. This approximation is well established as discussed in section 1.5. Further justification for considering the latitude and longitude TEC gradients constant can be found in [57].

The geometric relationship between the receiver and satellite locations and the IPP which is used in finding both the obliquity factor $OF_I(\zeta)$, $\Delta\phi_s$, and $\Delta\lambda_s$ is illustrated in figure 2.18.
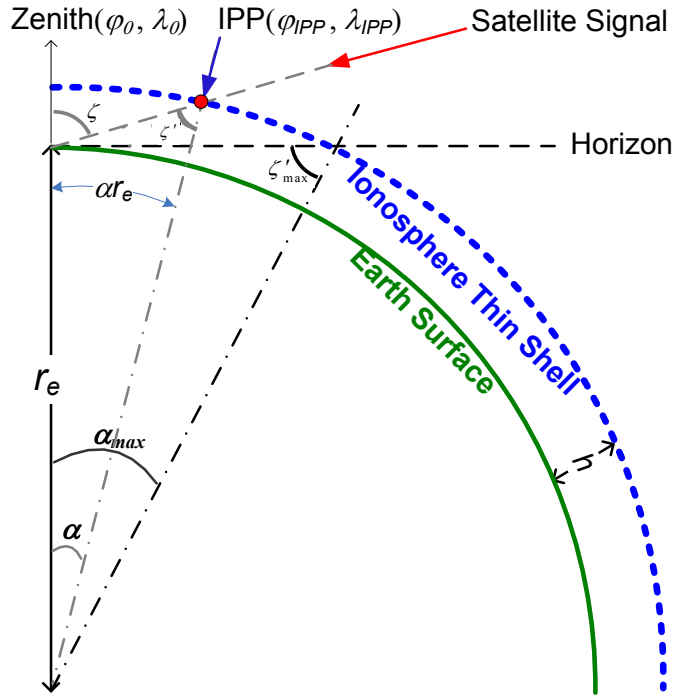

FIGURE 2.18. Geometric relationship among GPS signal propagation path, piercing point, and direct satellite viewing area.

The position of the ionosphere piercing point can be calculated from the angle α if the receiver and satellite positions are known. By using the angle α, the slant angle ζ', and the radius of the earth the distance from the receiver to the IPP can be found using:

$$r_{s,IPP} = \frac{R_e \sin(\alpha)}{\sin(\zeta')}$$
(2.16)

44

Using the distance to the IPP, the position of the IPP in earth centered earth fixed (ECEF) coordinate frame, can be found from the following:

$$\mathbf{x}_{IPP} = \mathbf{x}_r + \frac{r_{s,IPP}}{r_s}(\mathbf{x}_s - \mathbf{x}_r) \tag{2.17}$$

where XIPP, Xr, and Xs are the three dimentional corrodinate vector from the center of the Earth to the IPP, receiver, and satellite respectively. From the position of the IPP, it is trivial find both $\Delta\phi_s$ and $\Delta\lambda_s$.

Substituting the ionosphere error approximation described in equation 2.15 and 2.14 into 2.13 results in:

$$\Delta\rho_{s,corr} = OF_I(\zeta) \cdot \beta \left(I_0 + \frac{\partial I_{s,v}}{\partial \phi}\Delta\phi_s + \frac{\partial I_{s,v}}{\partial \lambda}\Delta\lambda_s \right) + c\Delta b_r + \Delta\epsilon_{s,corr} \tag{2.18}$$

where

$$\beta = \frac{f_{L1}^2 - f_{L2}^2}{f_{L1}^2 f_{L2}^2} \tag{2.19}$$

Equation 2.18 is rewritten as

$$\Delta\rho_{s,corr} = OF_I(\zeta) \cdot 40.3\beta \left(TEC_{0,v} + \frac{\partial TEC_v}{\partial \phi}\Delta\phi_s + \frac{\partial TEC_v}{\partial \lambda}\Delta\lambda_s \right) + c\Delta b_r + \Delta\epsilon_{s,corr} \tag{2.20}$$

to put the ionosphere contribution in terms of TEC, rather than the perceived increase in range. From 2.20, it can be seen that there are four unknowns which will be solved using the procedure described next. The zenith angle, ζ, needed for the obliquity factor calculation, is considered to be known since it can be calculated from the ephemeris, assuming the receiver position is known, which is the case as the receiver positions are fixed.

This is quite similar to the usual need in a GPS receiver to solve for the receiver position in three dimensions in the ECEF coordinate frame and the receiver clock error, δt_r. In that

case the range equation can be written as

$$\rho_s = \|\mathbf{x}_s - \mathbf{x}_r\| + c\delta t_r + \epsilon_s \tag{2.21}$$

where $\mathbf{x}_s$ is a vector representing the position of the satellite and $\mathbf{x}_r$ the position of the receiver and ϵ_s includes all the error sources with the exception of the receiver clock error, δt_r. The magnitude of the vectors difference replaces the true range, r_s. Again, the satellite position is considered to be known from the ephemeris broadcast as part of the GPS signal. Therefore, the unknowns to be found are the three components of the receiver position vector, $\mathbf{x}_r$, and the receiver clock error. These four unknowns can be solved by considering the range equations for all the visible satellites as a system of nonlinear equations. Given that there are usually six or more GPS satellites visible at any given time, this system of equations can be solved.

The usual way of solving this system of equations is to linearize them with respect to an initial estimate of the user position and then solve iteratively. The iterative solving method used in GPS positioning is known the as the Newton-Raphson method. Further description of the methodology can be found in any text which considers GPS positioning, such as [17]. In this method, an initial estimate of the parameters to be solved is made and this estimate is used to make an estimate of the true range. The difference between this estimated true range and the pseudorange is considered the error in the estimation and the iterative solving attempts to minimize this error. This solving method is used to estimate TEC zenith and gradients as well as the receiver IFB.

For the TEC estimation the system of equations which must be solved is given in matrix form:

$$
\begin{bmatrix}
\Delta\rho_1 \\
\Delta\rho_2 \\
\vdots \\
\Delta\rho_k
\end{bmatrix}
=
\begin{bmatrix}
40.3\beta & 40.3\beta\Delta\phi_1 & 40.3\beta\Delta\lambda_1 & c \\
40.3\beta & 40.3\beta\Delta\phi_2 & 40.3\beta\Delta\lambda_2 & c \\
& \vdots & & \vdots \\
40.3\beta & 40.3\beta\Delta\phi_k & 40.3\beta\Delta\lambda_k & c
\end{bmatrix}
\begin{bmatrix}
TEC_{0,v} \\
\frac{\partial TEC_v}{\partial \phi} \\
\frac{\partial TEC_v}{\partial \phi} \\
\Delta b_r
\end{bmatrix}
\tag{2.22}
$$

where k is the number of satellites visible at that measurement epoch. The initial estimates for all four of the unknowns are set to zero. However this form of the system of equations allows the receiver IFB to change between each measurement epoch which does not match the actual behavior of the IFB. As detailed in section 1.4.1 the variation in the IFB is relatively slow as it is due mostly to temperature changes. For this reason, the the system of equations is solved over multiple measurement epochs. This leads to equation 2.23 which is the method used in for the results shown in the following sections.

The results of the estimation can be used to find the approximate vertical and slant TEC for any satellite piercing point within the receivers view. This is accomplished by applying the distance to the desired IPP from the receiver, in latitude and longitude, to the gradients and, if the slant TEC is required, applying the obliquity factor. The direct comparison of the estimated TEC with the ISR measurements presented in the the results sections is accomplished by finding the TEC at the same point as the radar signal passes through the ionosphere.

$$
\begin{bmatrix}
\Delta\rho_1(1) \\
\Delta\rho_2(1) \\
\vdots \\
\Delta\rho_{k_1}(1) \\
\vdots \\
\Delta\rho_1(m) \\
\Delta\rho_2(m) \\
\vdots \\
\Delta\rho_{k_m}(m)
\end{bmatrix}
=
\begin{bmatrix}
40.3\beta & 40.3\beta\Delta\phi_1(1) & 40.3\beta\Delta\lambda_1(1) & 0 & & \cdots & & 0 & c \\
40.3\beta & 40.3\beta\Delta\phi_2(1) & 40.3\beta\Delta\lambda_2(1) & & & & & & \\
& \vdots & & \vdots & & \ddots & & \vdots & \\
40.3\beta & 40.3\beta\Delta\phi_{k_1}(1) & 40.3\beta\Delta\lambda_{k_1}(1) & 0 & & \cdots & & 0 & \\
0 & \cdots & 0 & \ddots & 0 & \cdots & & 0 & \vdots \\
0 & \cdots & & & 0 & 40.3\beta & 40.3\beta\Delta\phi_1(m) & 40.3\beta\Delta\lambda_1(m) & \\
& & & & & 40.3\beta & 40.3\beta\Delta\phi_2(m) & 40.3\beta\Delta\lambda_2(m) & \\
\vdots & \ddots & & & \vdots & & \vdots & & \\
0 & \cdots & & & 0 & 40.3\beta & 40.3\beta\Delta\phi_{k_m}(m) & 40.3\beta\Delta\lambda_{k_m}(m) & c
\end{bmatrix}
\begin{bmatrix}
TEC_{0,v}(1) \\
\frac{\partial TEC_v}{\partial\phi}(1) \\
\frac{\partial TEC_v}{\partial\lambda}(1) \\
\vdots \\
TEC_{0,v}(m) \\
\frac{\partial TEC_v}{\partial\phi}(m) \\
\frac{\partial TEC_v}{\partial\lambda}(m) \\
\Delta b_r
\end{bmatrix}
\tag{2.23}
$$

48

CHAPTER 3

RESULTS: ALASKA

The results presented in this chapter, as well as chapters 4 and 5, are derived from three measurement sources. These three sources all have particular strengths and weaknesses which will be highlighted in these results chapters. For clarity, each data source and how it will be presented in the results sections is discussed below.

The primary data source is GPS measurments made by the receivers collocated with each ISR. The data from GPS has been processed in two different ways to estimate the TEC affect on the GPS signal. The TEC zenith and gradient estimation method detailed in section 2.4 is primary of the two methods, as it is the method which is being evaluated and is the focus of this thesis. This method will be referred to as the GPS gradient method (GGM), and in figures which directly compare the GGM result to TEC estimated by other methods, the GGM result will be a blue trace. The GPS data used in the GGM estimation has undergone all of the processing and correction steps discussed in chapter 2. It is important to note that the GGM only produces a zenith TEC and latitude and longitude TEC gradients at each measurement epoch. The receiver IFB is also estimated for the entire solving interval, in this case approximately 24 hours. This means plots which show the TEC along some signal path, be it An ISR signal or a GPS satellite signal, are using the zenith TEC and gradients to calculate the approximate vertical TEC at the IPP and then scaling it by the slant angle of the signal path.

The second processing method uses equation 1.9 to calculate the TEC along the satellite-receiver signal path for each visible satellite. This is the standard method of TEC calculation for dual frequency, and will be referred to as standard dual-frequency method or SDM. The

49

data used in this TEC estimate has also been processed and corrected in the same way as the GGM TEC. However, the SDM TEC is not corrected for the receiver IFB. As discussed in section 2.4, a byproduct of the GGM TEC estimation is an estimate of the receiver IFB. This estimated IFB is used to correct the SDM to allow for direct comparison between the GGM TEC mapped to the satellite IPP and slant angle, and the SDM. In plot which include SDM results the SDM traces will be pink.

The second data source is also based on GPS, but not the receivers used for the GGM and SDM, but rather a global network of GPS receivers operated by the International GNSS Service (IGS). This data is processed to form a global two dimensional map of vertical TEC. These maps are known as global ionosphere maps, GIM, and will be referred two that way in future. GIM data in the results plots will be shown as green traces. The map has has relatively poor spatial and temporal resolution. Each GIM consists of a grid with pixels which are 2.5°in latitude by 5°in longitude. A new global map is available every two hours. A full day of maps is packaged into an IONEX file, a format description for which can be found in [58], and can be obtained from the IGS website, https://igscb.jpl.nasa.gov/components/prods.htmls. Because of the low spatial and temporal resolution of the GIMs, they are only considered for evaluation of the large scale value and trend of the GGM TEC. The GIMs are important, however, as they represent an estimate of the TEC from the earth surface all the way to the GPS orbital altitude, which the ISR profiles are not able to provide.

The third data source used for comparison are incoherent scatter radar profiles. To obtain the TEC from the radar profile, the measurements which makeup the profile are multiplied by the width of the range bin for that measurement. All the multiplied measurements for that profile are then summed, which gives the integrated electron density along the radar signal path, also known as the TEC. As mentioned before, this TEC will be consistently smaller

than the GGM and GIM value, as the radar profile does not reach as high an altitude. However, the ISR data provides much higher temporal resolution, and is therefore used to evaluate the GGMs large and small scale time variation. In addition to the TEC, the radar profile is also presented to provide more information on small scale variations which could be the result of an enhancement or depletion structure, which the profile will show more clearly. The TEC and profile measurements from the radars will be referred to as ISR measurements throughout the results chapters. These measurements will be displayed as red traces in the results plots.

The results considered in this chapter are from Poker Flat Research Range outside of Fairbanks, Alaska. The data used in these results was collected on July 1 and 3-5, 2014. The first three days of data are for a full 24 hours while the last day is for approximately 18 hours. The GPS satellite sky track which occurred on the first day are shown in figure 3.1. The satellite passes for the other days of this short period are almost identical and are therefore not shown.

A direct comparison of the TEC from the GGM, GIM, and ISR is presented in figure 3.2. The plots show the comparison on each of the four days of data availability listed above. Each plot shows the TEC from each of the data sources, as well as the GGM geometric dilution of precision (GDOP), which is an observable widely used in GPS positioning to indicate the effect of satellite geometry on the position solution [17]. The notable features of the plots are discussed below.

On the first three days the GGM and GIM TEC match extremely well in the long term value and variation. The agreement is extremely close, within just a couple of TECu, as indicated 3.1. This level of agreement is the best out of all three locations considered.
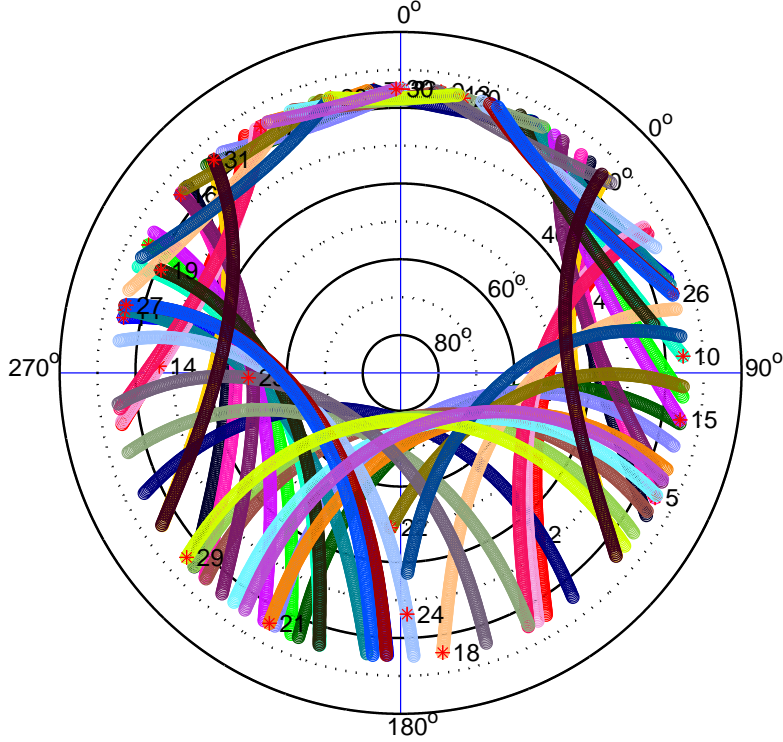
FIGURE 3.1. GPS satellite paths across the sky for 24 hours from PFRR on July 1, 2014. Each color represents a different satellite.

It is worth noting that the correspondence of the two TEC values is poorest on July 5, when less than a full day of data was used. This is possibly due to a poor estimate of the receiver IFB when less than a full day is considered. This effect can also be seen in the results from Puerto Rico and will be discussed further in chapter 4. The IFB estimates, table 3.2, however, do not clearly indicate this, as the July 5 value is not significantly different from the other three days. In fact, July 4 seems to be the outlier, but the plot shows strong correspondence on that day.

TABLE 3.1. RMS error between TEC measurement methods during July 2014 at Poker Flat, Alaska.

	ISR-GGM	GGM-GIM	ISR-GIM
July 1	6.865 TECu	0.8129 TECu	7.216 TECu
July 3	7.182 TECu	2.170 TECu	8.065 TECu
July 4	8.044 TECu	1.539 TECu	8.533 TECu
July 5	7.624 TECu	2.501 TECu	9.716 TECu

The GGM and ISR TEC also concur in their long term variation, though not value. It is not expected that the PFISR TEC would match in value, as its profiles only extend to 750 km, much lower than the other two ISRs. The PFISR data is quite noisy, which makes comparison of any fine scale structures difficult. This noisiness is also well illustrated in the time series plot of the density profiles shown in figures 3.3, 3.4, 3.5, and 3.6, as well as the GGM and ISR TEC with the GIM TEC subracted shown in figure 3.7.

TABLE 3.2. Inter-frequency bias estimate for Poker Flat GPS receiver.

July 1	July 3	July 4	July 5
-16.89 TECu	-16.09 TECu	-18.55 TECu	-17.26 TECu

Even with the noise in the ISR measurement, it is clear that fluctuations in the GGM TEC occur with no corresponding change the ISR measurement. These fluctuations occur at the same time as jumps in the GDOP, indicating they are caused by changes in satellite geometry rather than any real change in TEC.

Additional GGM fluctuations of greater magnitude can be observed on July 3 and 4 at approximately 4:00 and 18:00 respectively. A large jump can also been seen in the SDM TEC, figure 3.13. This indicates there is simply a measurement error in the pseudorange rather than a problem in the TEC estimation.

Large discontinuities can also been seen in the ISR measurements on July 3 through 5 in figure 3.2. By observing the electron density profile time series, these occurrences can be seen to occur due to profiles which contain nothing but invalid measurements.

The GGM and ISR with the GIM subtracted, figure 3.7, also show extremely close agreement between the GGM and GIM. In addition, it shows that in the absence of large

discontinuities in either the GGM or ISR measurements, the GGM TEC has a smaller standard deviation then the ISR TEC indicating the GGM provides a less noisy measurement. This is true in spite of the geometry based fluctuations discussed previously.

Figures 3.8, 3.9, 3.10, and 3.11 show a comparison of the GGM and SDM TEC. The first two plots were chosen because they show poor correspondence between the GGM and SDM, and the second two because they show excellent correspondence. The interesting feature of the poor agreement plots is that the first shows the GGM much larger than the SDM at the apex of the satellite pass while the second shows smaller GGM. However, during the lower elevation portions of the pass the correspondence is much closer, which should not occur as the TEC sheet approximation used in the GGM should be more valid when the IPP are close to the receiver, when the satellite elevation is high. The two close concurrence cases shown provide evidence that the two methods can be identical over the entire satellite pass. Further investigation is needed to determine what circumstances lead to poor agreement between the methods.

Figure 3.12 shows the GGM TEC along each satellite path. All four days have a number of large discontinuities at the beginnings and ends of some satellite passes. This is concerning, as no corresponding fluctuations can be seen in the SDM TEC, meaning the discontinuity does not occur in the data but is a function of the estimation method. This indicates a problem in the estimation algorithm which needs further investigation.

The difference of the GGM and SDM, figure 3.14, shows the two are within 20 TEC units at almost all times, even in the presence of the geometry induced fluctuation in the GGM. This is encouraging for coarse grain measurement using the GGM but shows too much fluctuation to expect fine grain observably. However, using the IFB to correct the SDM may allow for the best of both.

The mean of the SDM-GGM difference with the standard deviation show as error bars is presented in figure 5.16. These results are included to better characterize the accuracy of the GGM. From figure 5.16 the mean difference between the two methods can be seen to be with approximately pulse-minus four TECu however the standard deviation can be quite large. The large standard deviation of a single satellite on January 3 and 4 simply indicates a measurement problem for that satellite which can also be observed in figures 3.12 and 3.13.

Consideration of the TEC gradients is also important, as the GGM is primary concerned with estimating the gradients. Figure 3.16 show the zenith TEC and gradients from the GIM and GGM. The two agree well in general, but are far from perfect concurrence. However, this is not unexpected as the time and spatial resolution of the GIM means only general agreement can realistically be hoped for.
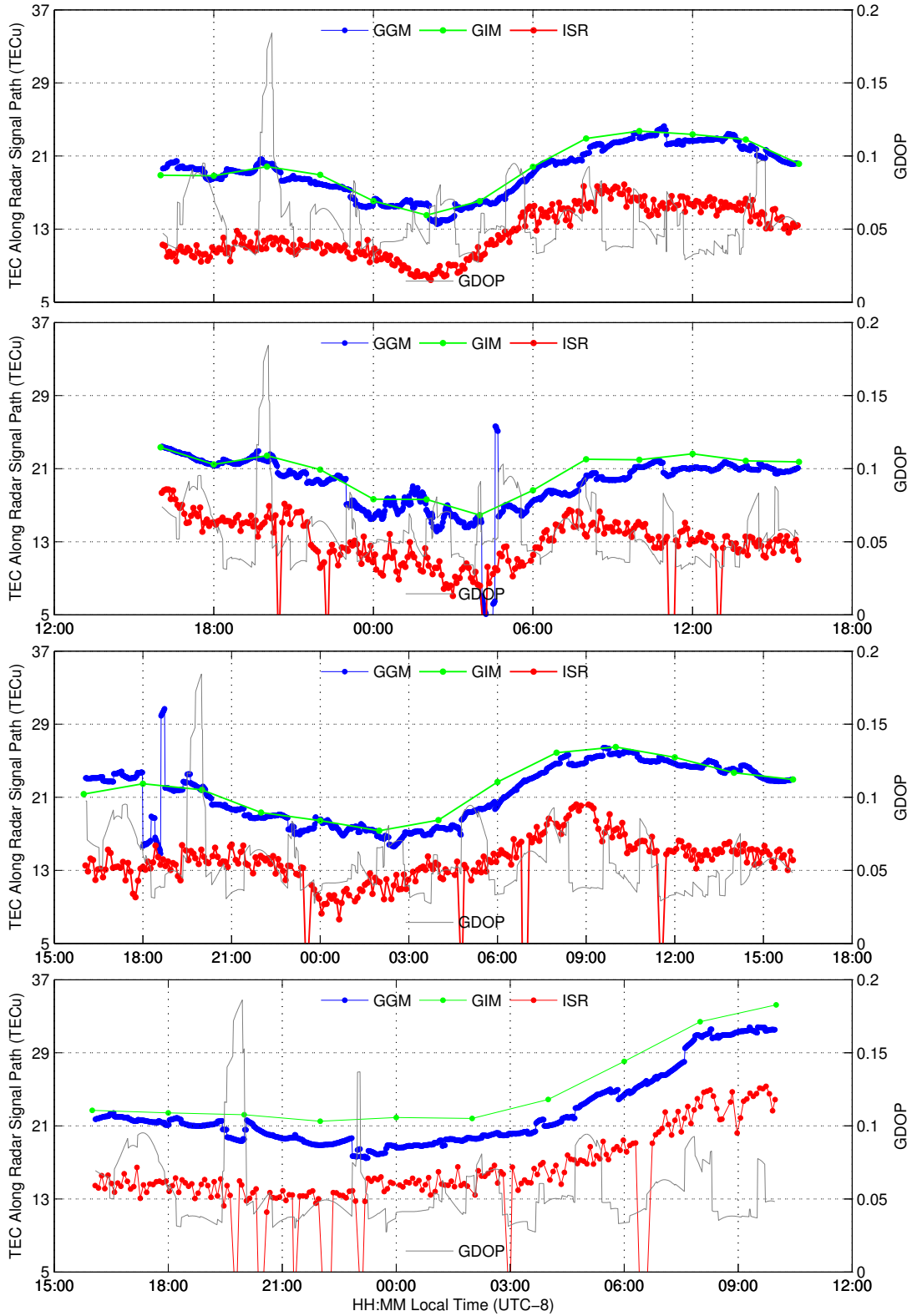
FIGURE 3.2. TEC along PFISR signal path derived from ISR (red), GGM (blue), and GIM (green), as well as the GDOP (gray) for July 1, 3-5 top to bottom.
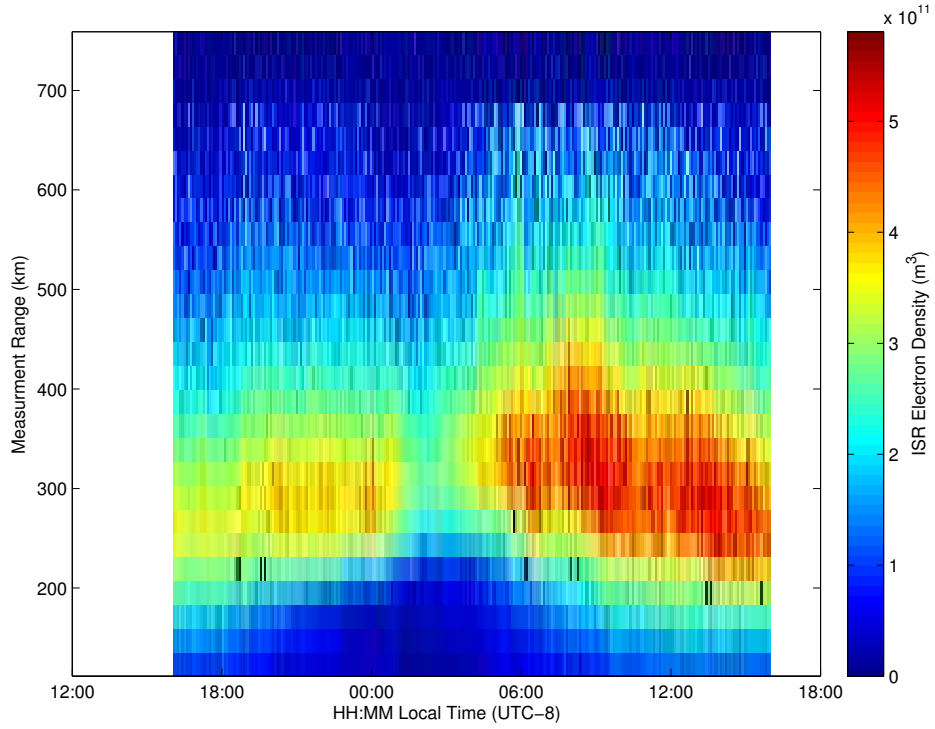
FIGURE 3.3. Time series of electron density profiles from the PFISR for July 1.
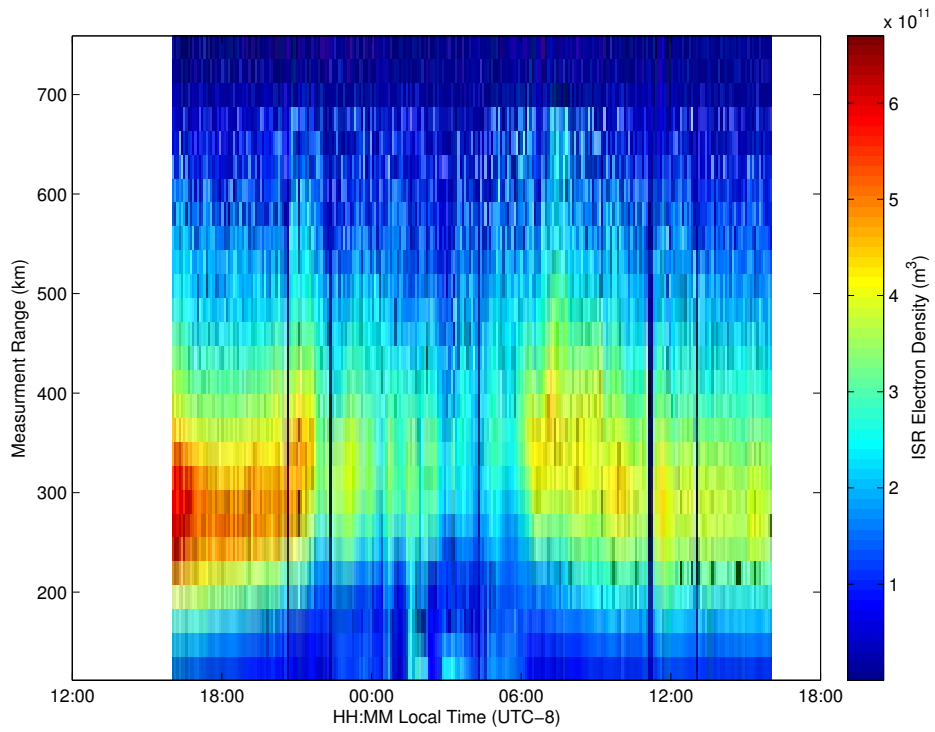
FIGURE 3.4. Time series of electron density profiles from the PFISR for July 3.
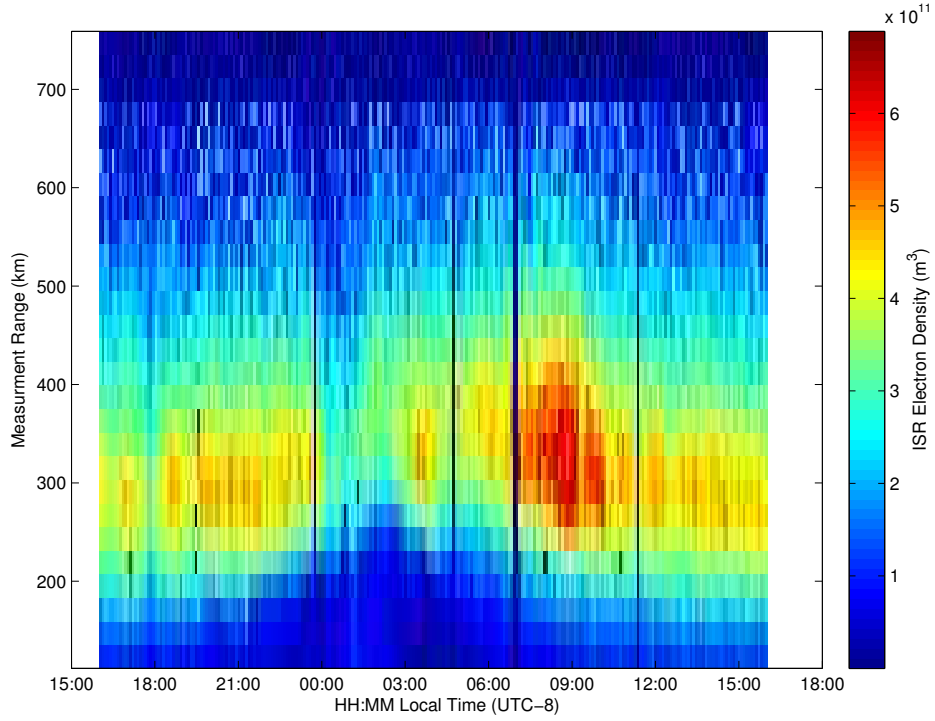
FIGURE 3.5. Time series of electron density profiles from the PFISR for July 4.
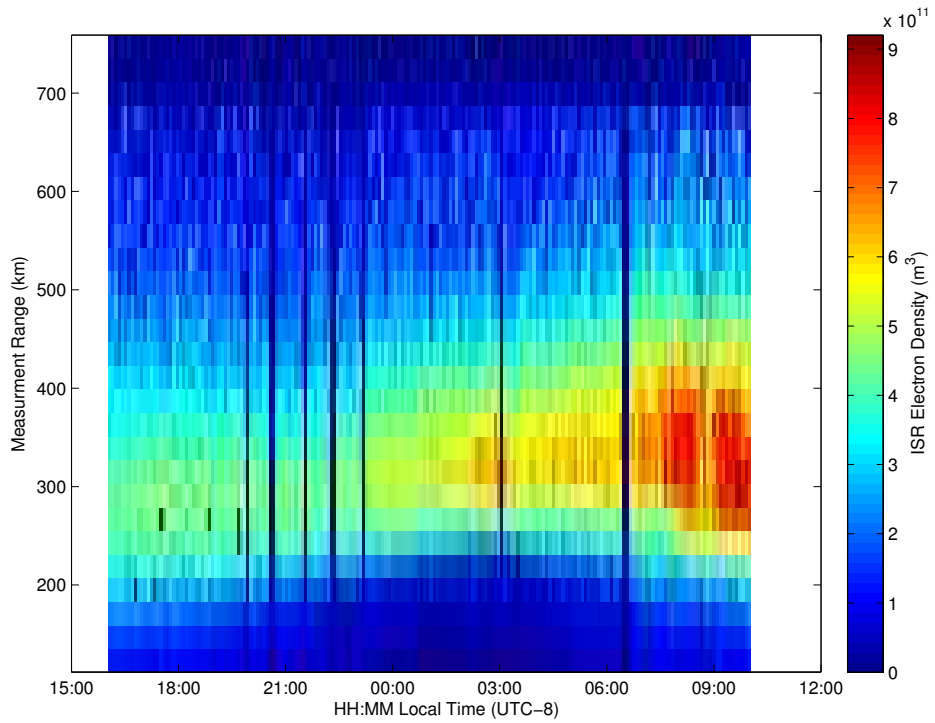
FIGURE 3.6. Time series of electron density profiles from the PFISR for July 5.
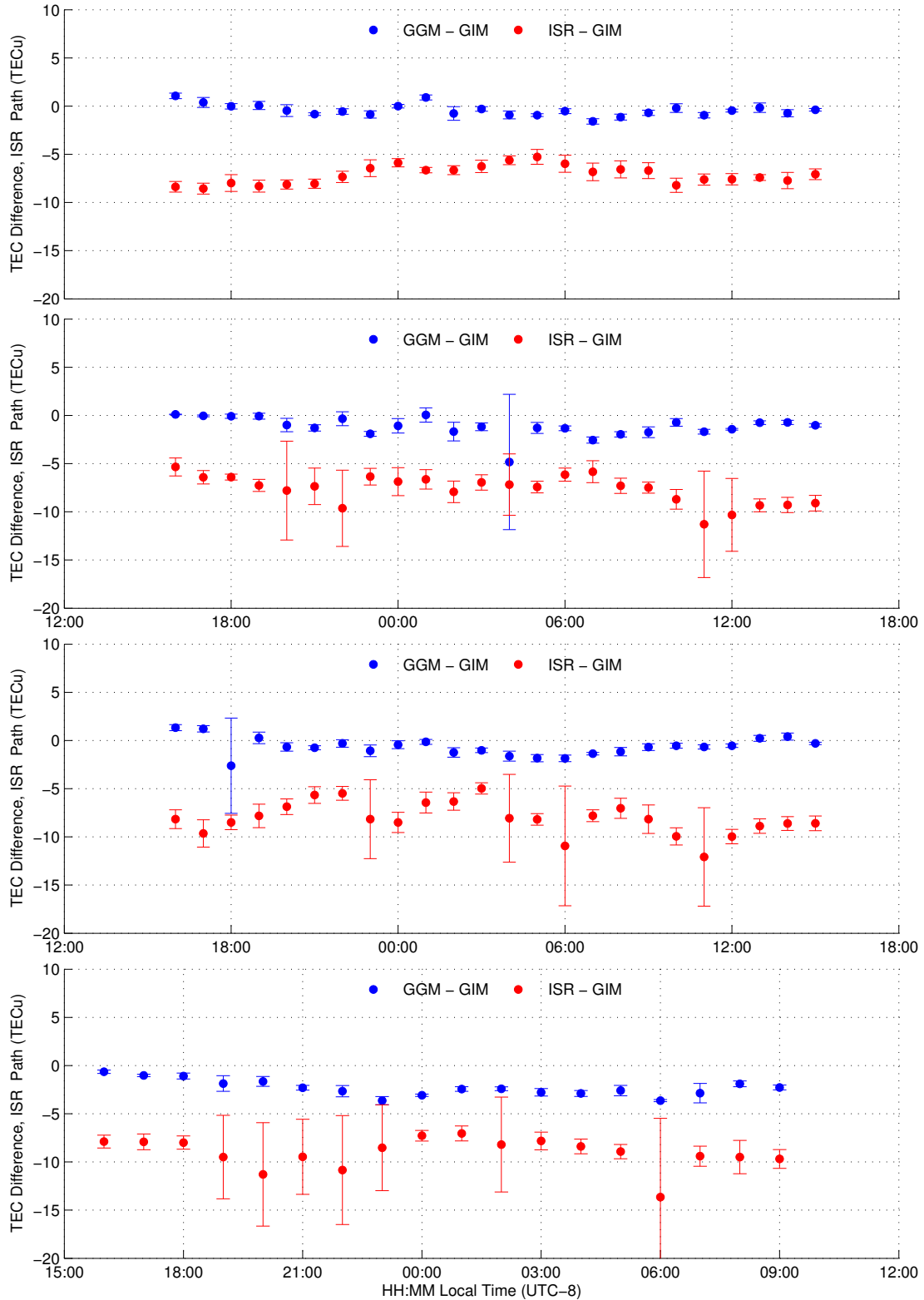
FIGURE 3.7. Difference between the GGM and IGS map (blue) as well as radar profile and IGS map TEC (red) estimate along the radar signal path. From PFRR, July 1 and 3-5, top to bottom.

59
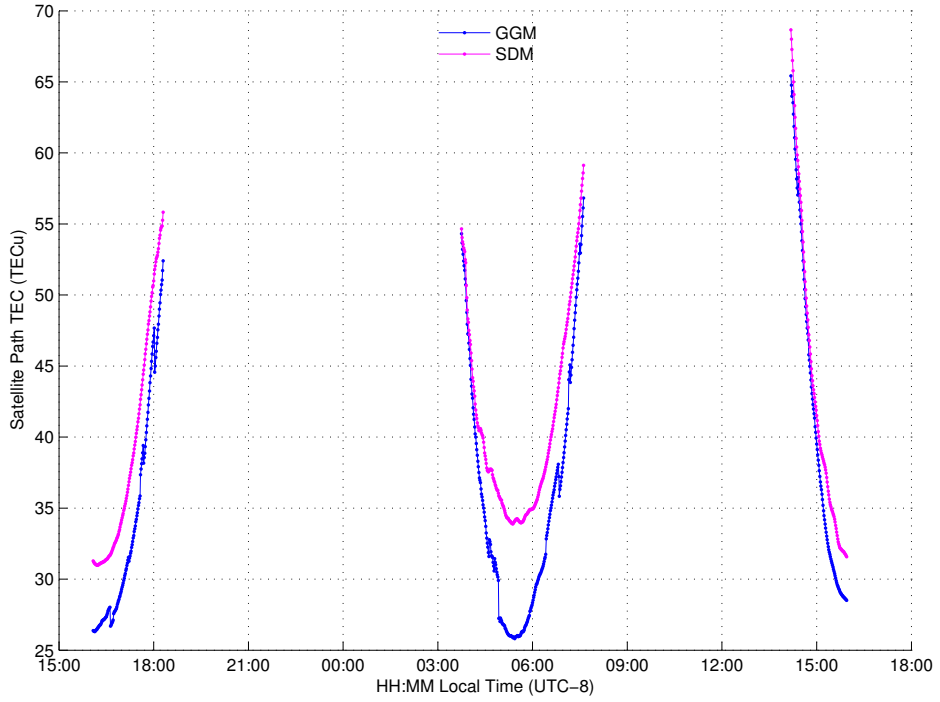
FIGURE 3.8. Comparison between TEC from the GPS gradient method (blue) and standard dual-frequency method (pink) for PRN 6 from PFRR on July 1.
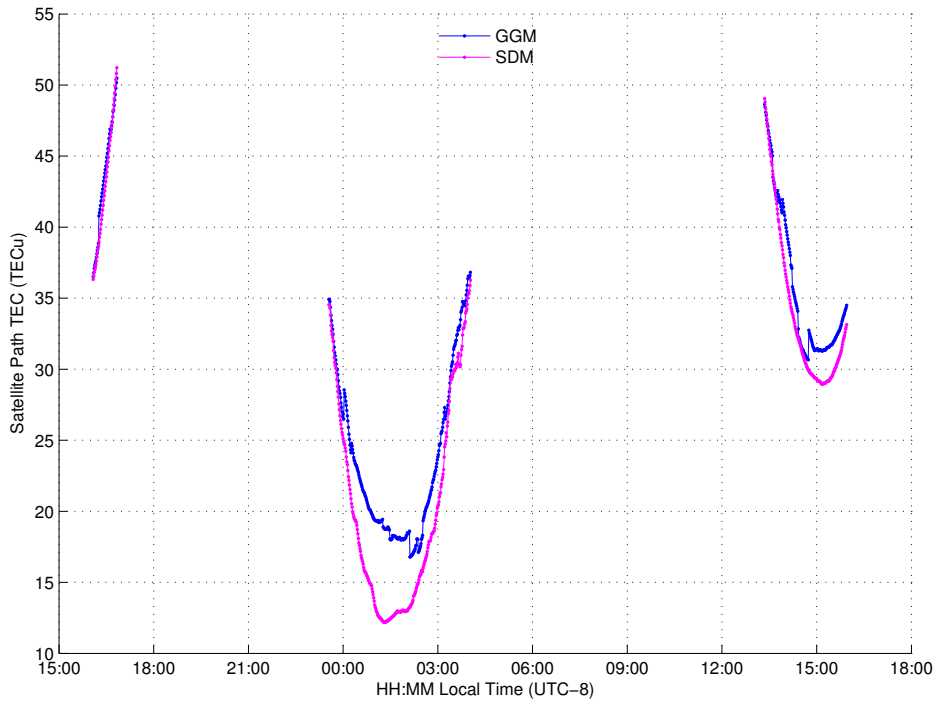
FIGURE 3.9. Comparison between TEC from the GPS gradient method (blue) and standard dual-frequency method (pink) for PRN 14 from PFRR on July 1.
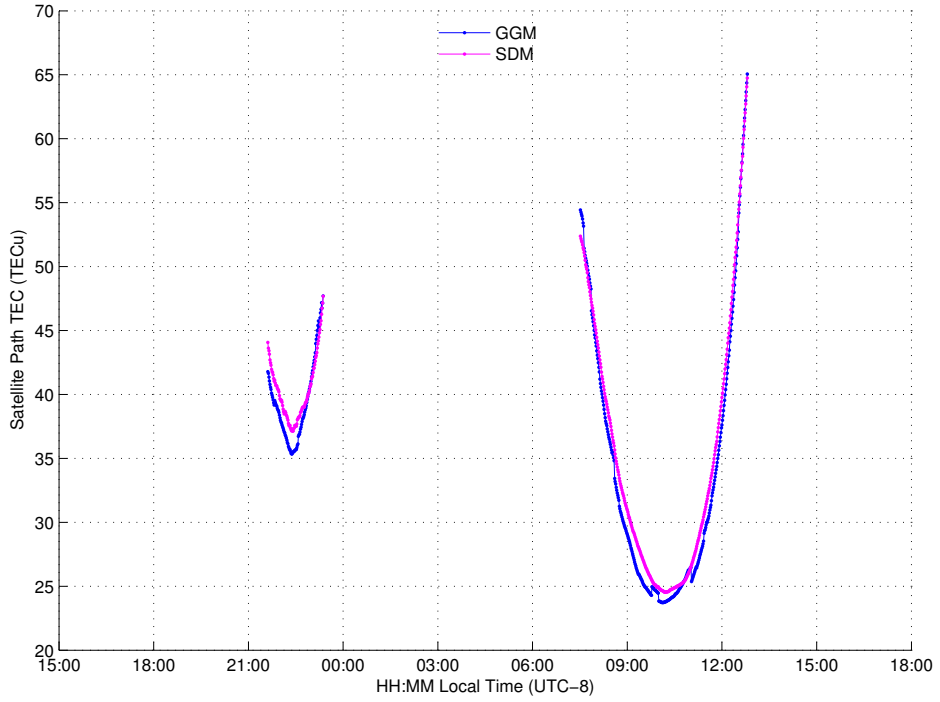
FIGURE 3.10. Comparison between TEC from the GPS gradient method (blue) and standard dual-frequency method (pink) for PRN 9 from PFRR on July 1.
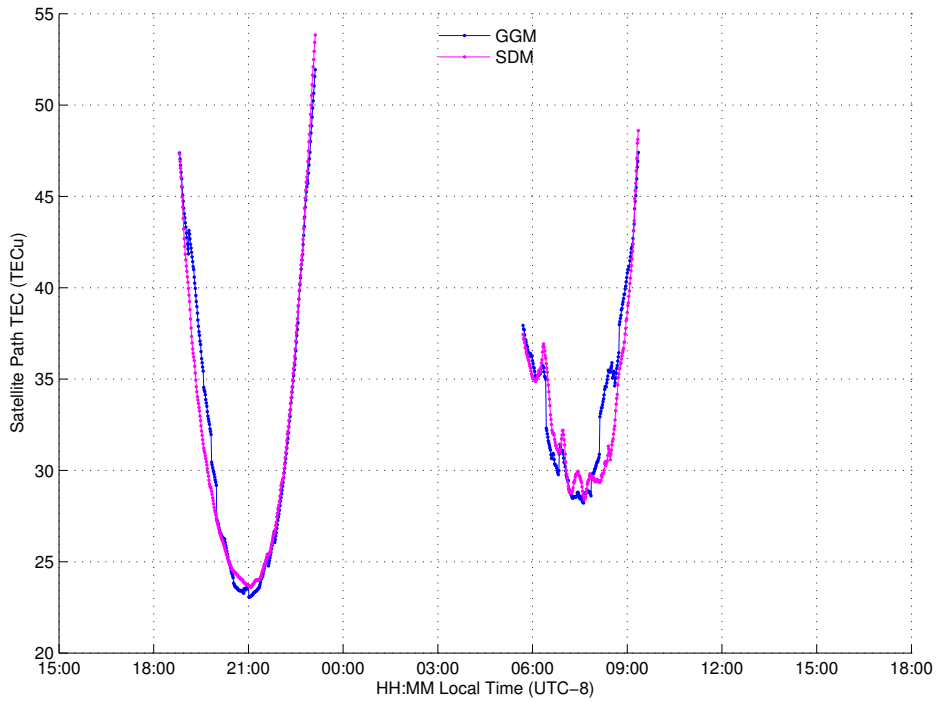
FIGURE 3.11. Comparison between TEC from the GPS gradient method (blue) and standard dual-frequency method (pink) for PRN 16 from PFRR on July 1.
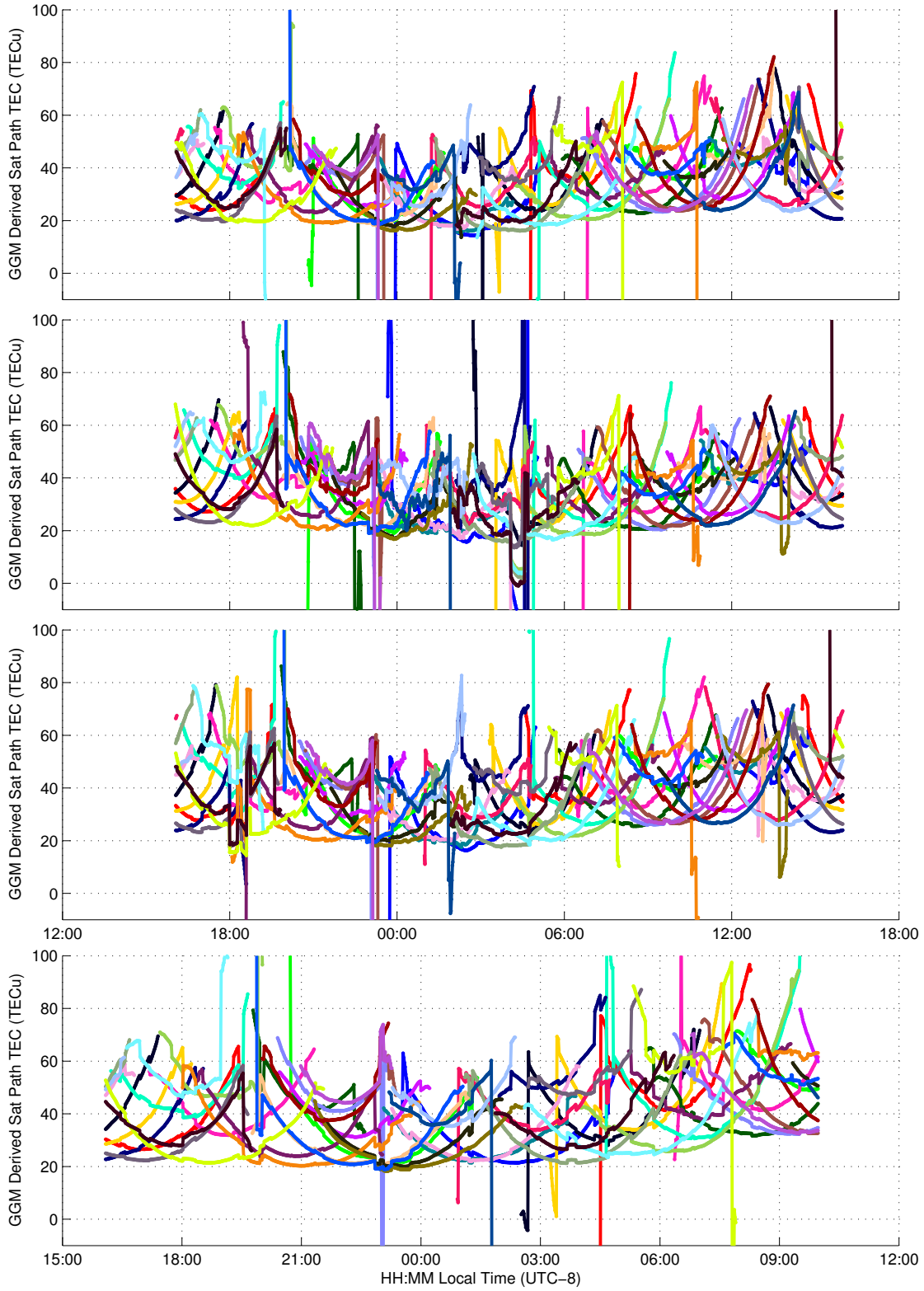
FIGURE 3.12. GGM TEC along satellite signal paths over 24 hours from PFRR, July 1 and 3-5, top to bottom. Each color represents a different satellite.
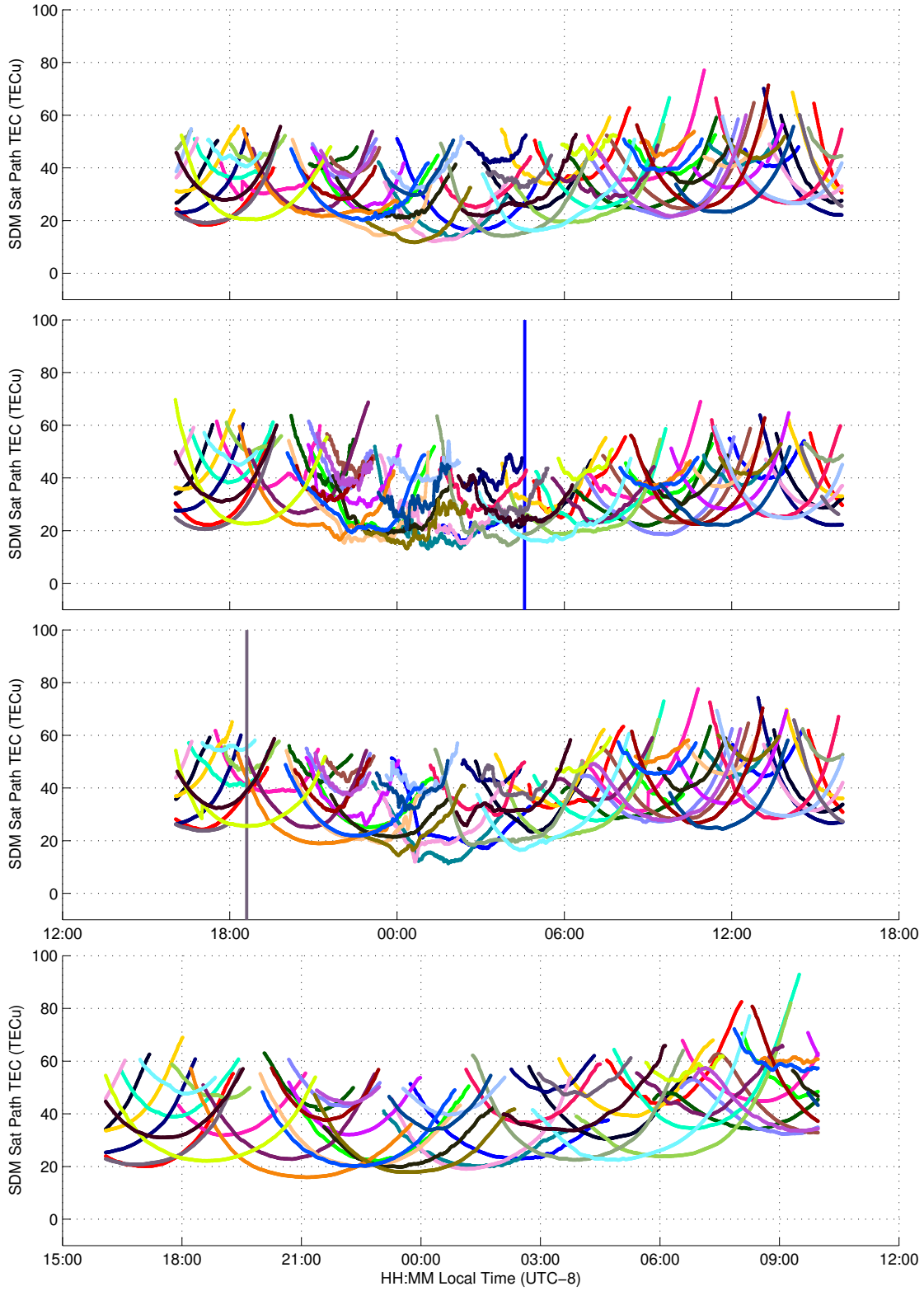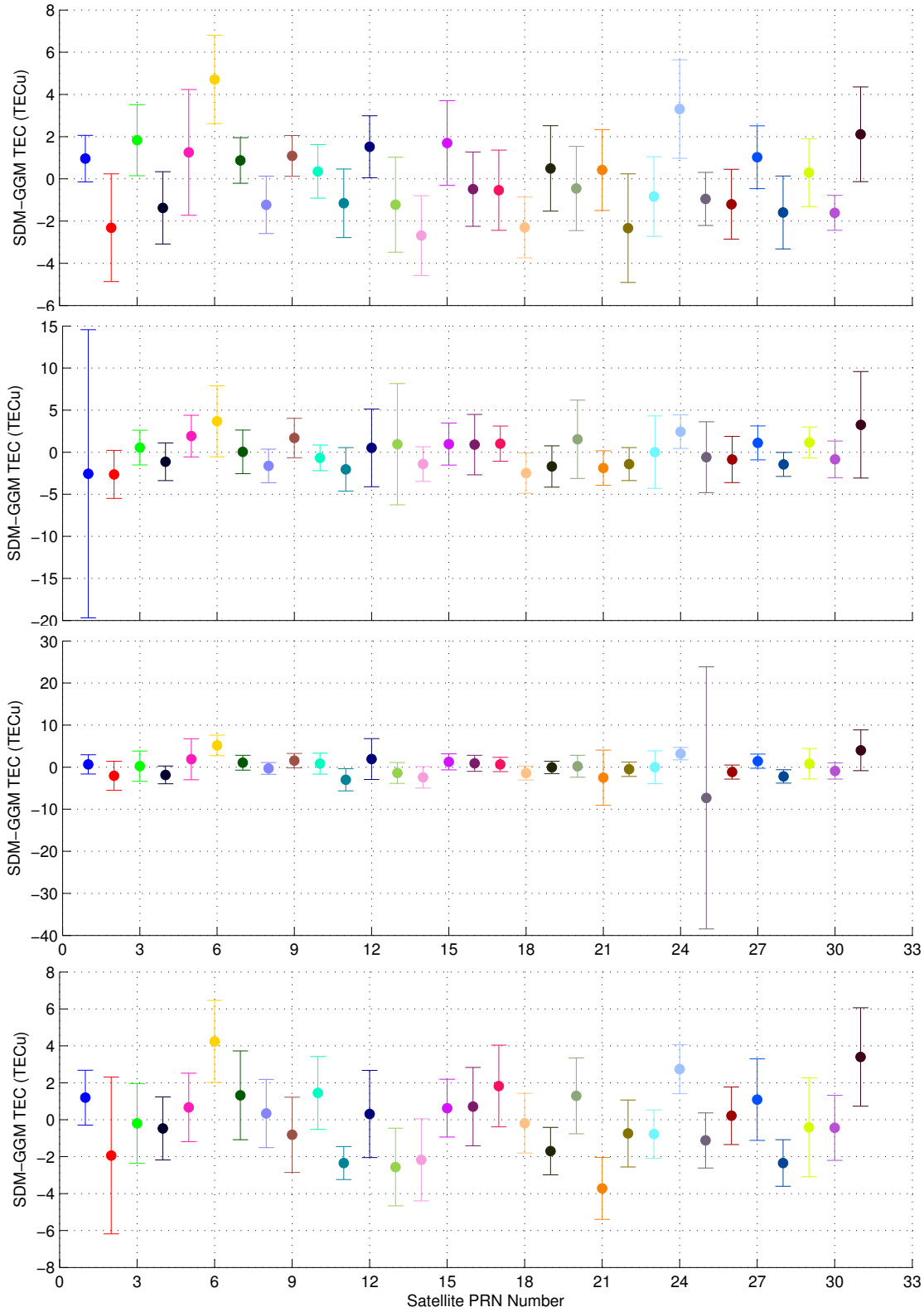
FIGURE 3.13. SDM TEC along satellite signal paths over 24 hours from PFRR, July 1 and 3-5, top to bottom. Each color represents a different satellite.
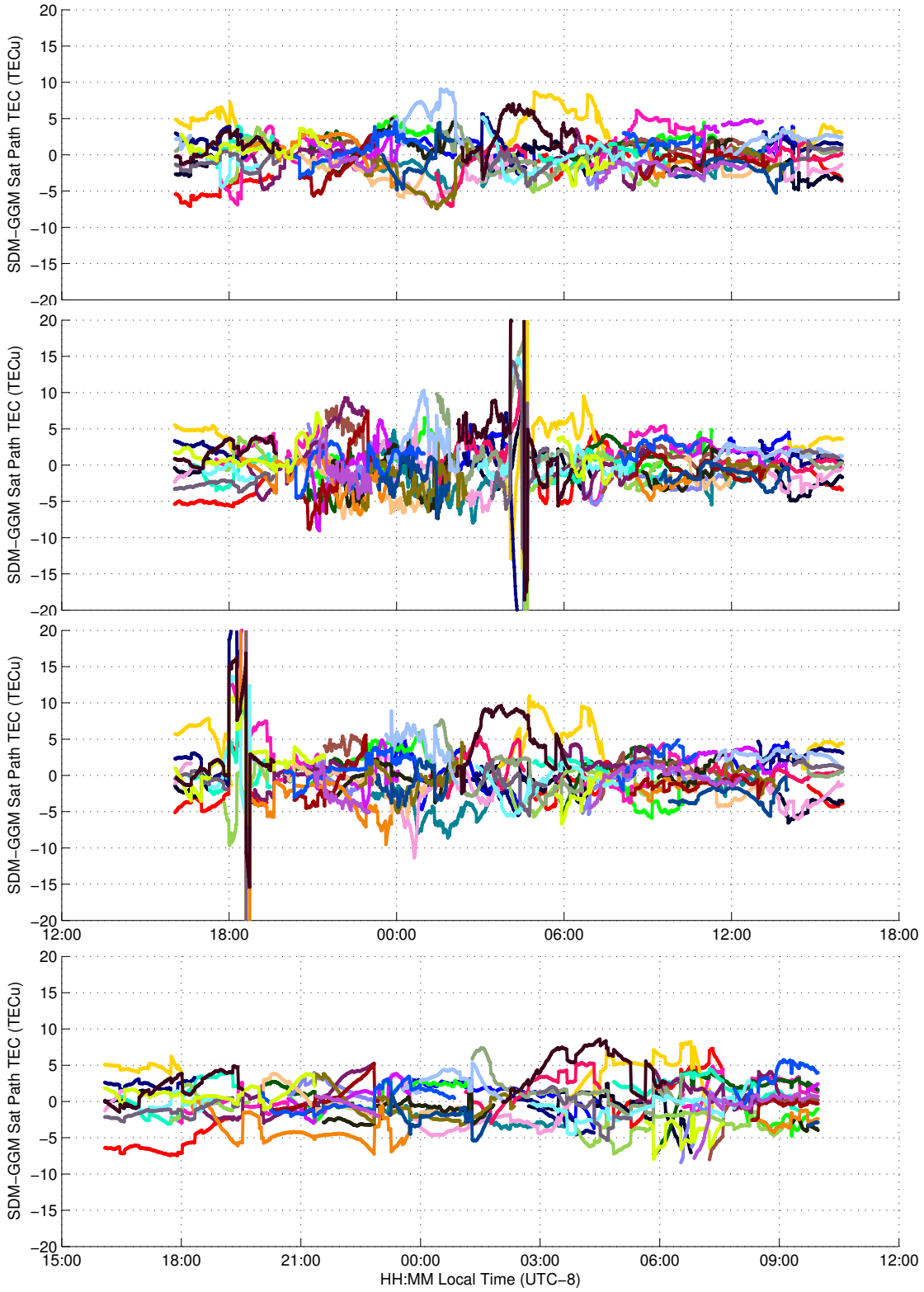
FIGURE 3.14. SDM-GGM TEC difference along satellite signal paths over 24 hours from PFRR, July 1 and 3-5, top to bottom. Each color represents a different satellite.

FIGURE 3.15. SDM-GGM TEC difference mean and standard deviation along satellite signal paths over 24 hours from PFRR, July 1 and 3-5, top to bottom. Each color represents a different satellite.
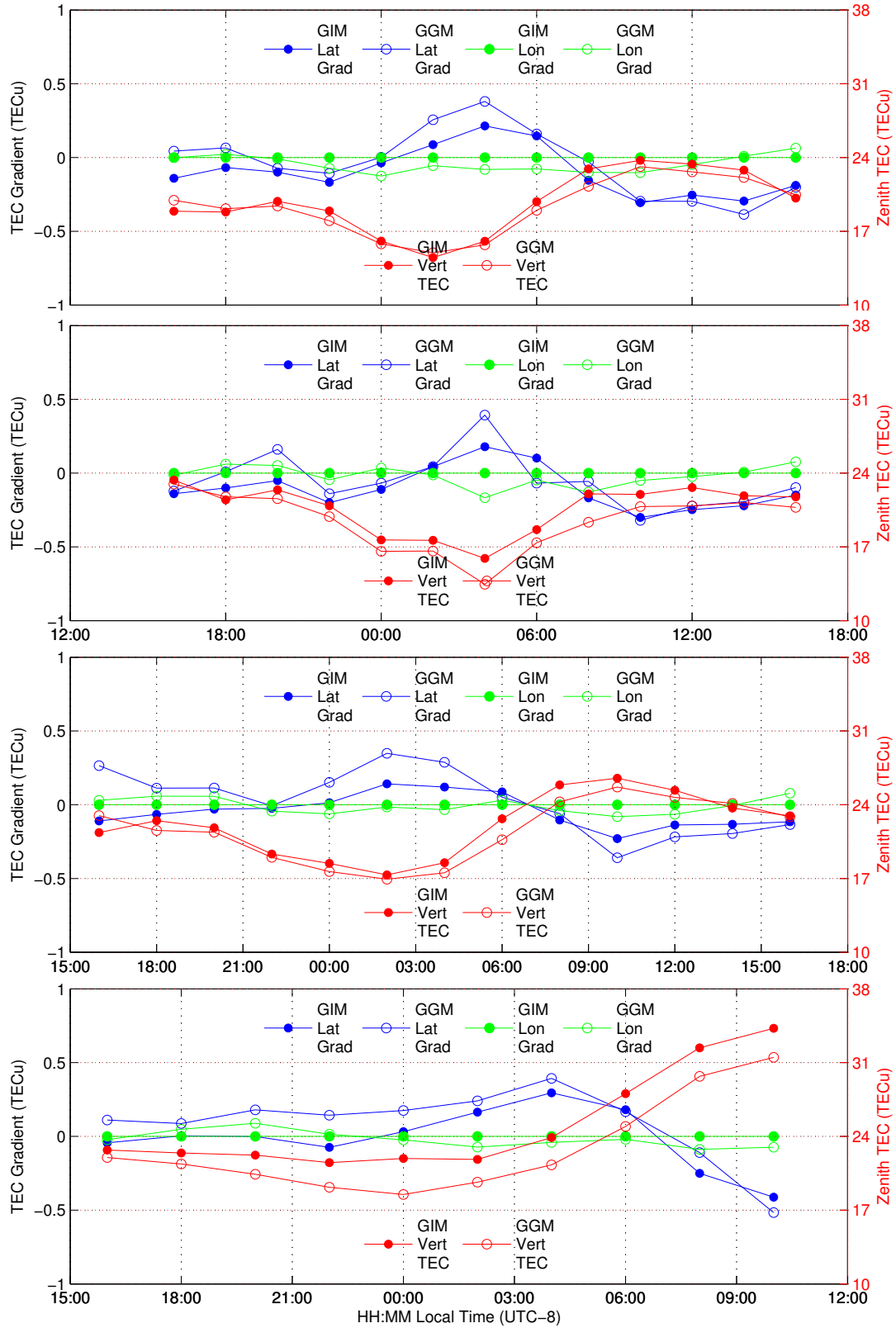
FIGURE 3.16. Comparison between GGM and IGS map zenith, latitude and longitude gradients. From PFRR, July 1 and 3-5, top to bottom.

CHAPTER 4

Results: Puerto Rico

This chapter presents the TEC estimation results from a simultaneous ISR and GPS experiment conducted in January, 2014 on the north west side of Puerto Rico. These results are somewhat different from the other locations in that data from an array of four receivers was available during the experiment. The results presented are from one complete 24 hour period on January 25 and a 20 hour period on the 26. The GPS satellite passes which occurred on the first day are shown in figure 4.1. The satellite passes on the second day are almost identical and are therefore not shown.
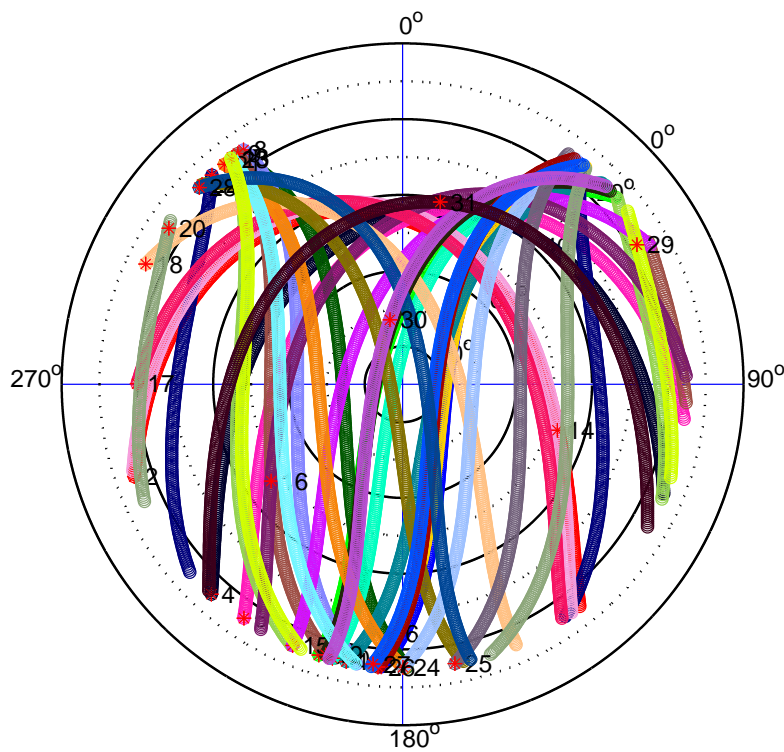
FIGURE 4.1. GPS satellite paths across the sky for 24 hours from NAIC on January 25. Each color represents a different satellite.

The direct comparison of the TEC from the GGM, GIM, and ISR is presented figures 4.6 and 4.7 for January 25 and 26 respectively. These plots show the comparison for GGM

TEC from each of the receivers in the Puerto Rico array for both of the days. In addition, each plot shows the GDOP. There are quite a few notable features evident in these two plots which are discussed below

On both days the long term variation of the GGM and GIM TEC agree quite well. This general agreement of the long term variation is all that can be expected, as the GIM does not have the temporal resolution to make a direct comparison possible. Encouragingly, the agreement between the two is constant across all four receivers, indicating the receiver IFB has been successfully mitigated. A more quantitative view of the GGM, GIM comparison can be seen in table 4.1.

TABLE 4.1. RMS error between TEC estimation methods for GPS receivers at NAIC (RX 0), near Barceloneta (RX 1) near Quebradillas (RX 2), and in Mayagez (RX 3) during 2014 experiment in Puerto Rico.

Day	Receiver	ISR-GGM	GGM-GIM	ISR-GIM
Jan 25	Rx0	6.603 TECu	2.120 TECu	7.625 TECu
	Rx1	6.675 TECu	2.163 TECu	
	Rx2	6.029 TECu	2.510 TECu	
	Rx3	6.231 TECu	2.349 TECu	
Jan 26	Rx0	4.482 TECu	3.731 TECu	7.496 TECu
	Rx1	4.551 TECu	3.742 TECu	
	Rx2	4.715 TECu	3.580 TECu	
	Rx3	4.094 TECu	4.183 TECu	

The agreement between the GGM and GIM is seen to be noticeably poorer on January 26. The likely explanation for this is the GGM estimate was only made over 20 hours and not the full day. This idea is supported by table 4.1, which shows the RMS difference is consistently greater on January 26 across all the receivers. This indicates that solving over the shorter, 20 hour, period resulted in a poor estimation of the receiver IFB resulting in its effect on the TEC not being fully corrected. This hypothesis is born out by table 4.2 which shows the estimated IFB on January 26 is consistently smaller for all four receivers than on

the previous day. It is possible, but unlikely, that the IFB was lower for all receivers due to that day being cooler.

TABLE 4.2. Inter-frequency bias estimate for all four receivers during the Puerto Rico experiment on January 25 and 26

	Jan 25	Jan 26
Rx0	-25.69 TECu	-23.31 TECu
Rx1	-19.13 TECu	-15.96 TECu
Rx2	-19.41 TECu	-17.82 TECu
Rx3	-19.73 TECu	-16.11 TECu

The GGM and ISR TEC also correspond closely in the long term variation, and both show variations in the trend which are not visible in the GIM. This is expected due to the higher temporal resolution of the GGM and ISR measurements. There are, however, quite a few instances of short duration enhancements and depletions in the GGM TEC when there is no corresponding change in the ISR TEC. This indicates one of two things: there are TEC enhancements or depletions in an area of the sky not visible to the ISR, or these fluctuations are due to changes in the satellite geometry. By comparing the occurrence of these fluctuation with the GDOP in figures 4.6 and 4.7 it can be seen that they occur at the same time as jumps in the GDOP. This indicates the fluctuations are not due to structures within the ionosphere, but rather changes in the satellite geometry. However, changes in satellite geometry do not always result in a fluctuation in the GGM TEC. Further work is needed to resolve these geometry induced fluctuations, as they present a major obstacle to fine grain measurement of the TEC. One possible avenue of investigation would be the expansion of the GGM to use the other satellite navigation constellations to increase the number of visible satellites and thereby reducing GDOP fluctuations.

There is an instance, around 3:00 on January 25, in which a fluctuation occurs in both the GGM and ISR TEC. Because it appears in both measurements, the fluctuation is likely

due to an electron density enhancement. This supposition is born out by examining the radar profile, figure 4.4, at that same time. At approximately 250 km, a slight, short term, enhancement can be seen. This indicates the GGM is capable of measuring relatively small ionosphere structures with accuracy.

By considering figures 4.6 and 4.7 in concert with the corresponding radar profiles, figures 4.4 and 4.5, cases in which there is an apparent enhancement or depletion present in the ISR TEC without a corresponding fluctuation in the GGM TEC can be observed. These fluctuations, which occur at approximately 23:00, 00:00, 12:00, and 15:00 on January 25 and 23:00 and 10:00 January 26. The three depletion events at 23:00, 00:00, January 25 and 23:00 January 26 correspond to single profiles which show a lower measurement of electron density across the entire profile. This indicates an error in the measurement or processing at that epoch. The other fluctuations are enhancements which can be seen at around 175 km range in the density profiles. These could be due coherent scatter from density structures or simply measurement error.

Figures 4.6 and 4.7 show the GGM-GIM and ISR-GIM differences. These plots indicate that the GGM measurements agree within five TEC units of the GIM, and follow the same pattern as the radar measurements but shifted upward by approximately five TECu. This is most readily visible in 4.6, while 4.7 indicates a certain amount of disagreement between the two methods. In fact, even the trend of the GGM and ISR differences do not match on January 26. They actually seem to diverge around the start and end of the data period.

Further evaluation of the TEC estimate can be accomplished through consideration of the TEC along each satellite signal path. The satellite signal path TEC is derived from the GGM and SDM methods which allows for both evaluation of the accuracy the IFB estimate and helps highlight instances of geometry induced fluctuations in the GGM TEC estimate.

Figure 4.8, 4.9, 4.10, and 4.11 show the slant TEC from the GGM and SDM methods for selected satellites from the Arecibo receiver. The first two plots were selected because they illustrate poor agreement between the GGM and SDM TEC. Figure 4.8 shows an instance in which the satellite is at low elevation and shows relatively large fluctuation in both the GGM and SDM, however, the GGM TEC does not follow the SDM. Poor agreement is expected for lower elevation satellites, as the IPP is further from the receiver and therefore the flat sheet approximation is less applicable. But, in figure 4.9, a major discrepancy occurs at the apex of the satellite pass indicating problems in the estimation do not only occur for low elevation satellites. On the other hand, figures 4.10 and 4.11 show almost complete agreement between the GGM and SDM over the entire satellite pass, even at low elevations.

The supposition that the estimation is less affective when the IPP is furthest from the receiver, for low elevation satellites, is born out by comparing 4.12 and 4.13 with 4.14 and 4.15. The first two of these plots show the TEC derived from the GGM, and the second two show TEC from the SDM. From these it is evident that the agreement between estimation methods is the poorest when the TEC is largest, which is when the satellite is lowest in the sky.

The difference of the two methods is also interesting, as it shows discrepancies between the methods are mirrored around zero. This indicates the geometry changes cause an artificial enhancement or depletion in the gradient which then causes the opposite effect in portion of the gradient on the other side of the receiver. The difference results can be seen in figures 4.16 and 4.17.

The mean and standard deviation of the SDM-GGM difference, figure 4.18 and 4.19 show that the mean difference between the two has a range of ten TECu. However the standard deviation of the difference for some satellites is more than 12 TECu while for others it is

as little as two TECu. The factors which lead to the differences in the variation between satellites requires further investigation to find if large variation occurs at certain locations in the receiver viewing area or if there is some other pattern which could indicate a method of mitigating the fluctuations.

Because the estimation method presented in this thesis is concerned with estimating the gradients of the TEC with respect to latitude and longitude, it is desirable to also evaluate the accuracy of the gradients. In figures 4.20 and 4.21, a comparison of the gradient and zenith TEC from the GGM and the GIM is presented. The GGM values are averaged over the two hours of applicability of each GIM to provide a more direct comparison. On both January 25 and 26, the agreement between the GGM and GIM for all three parameters is quite good for all four receivers. There is an interesting discrepancy present between two of the receivers and the IGS measurements. In those two instances the GIM gradient does not match the GGM derived gradient or the GIM gradient at the other two receiver locations. This is likely due to the low spatial resolution of the GIM, resulting in the farther two of the receivers, Rx2 and Rx3, falling into a different bin of the map causing the disagreement.
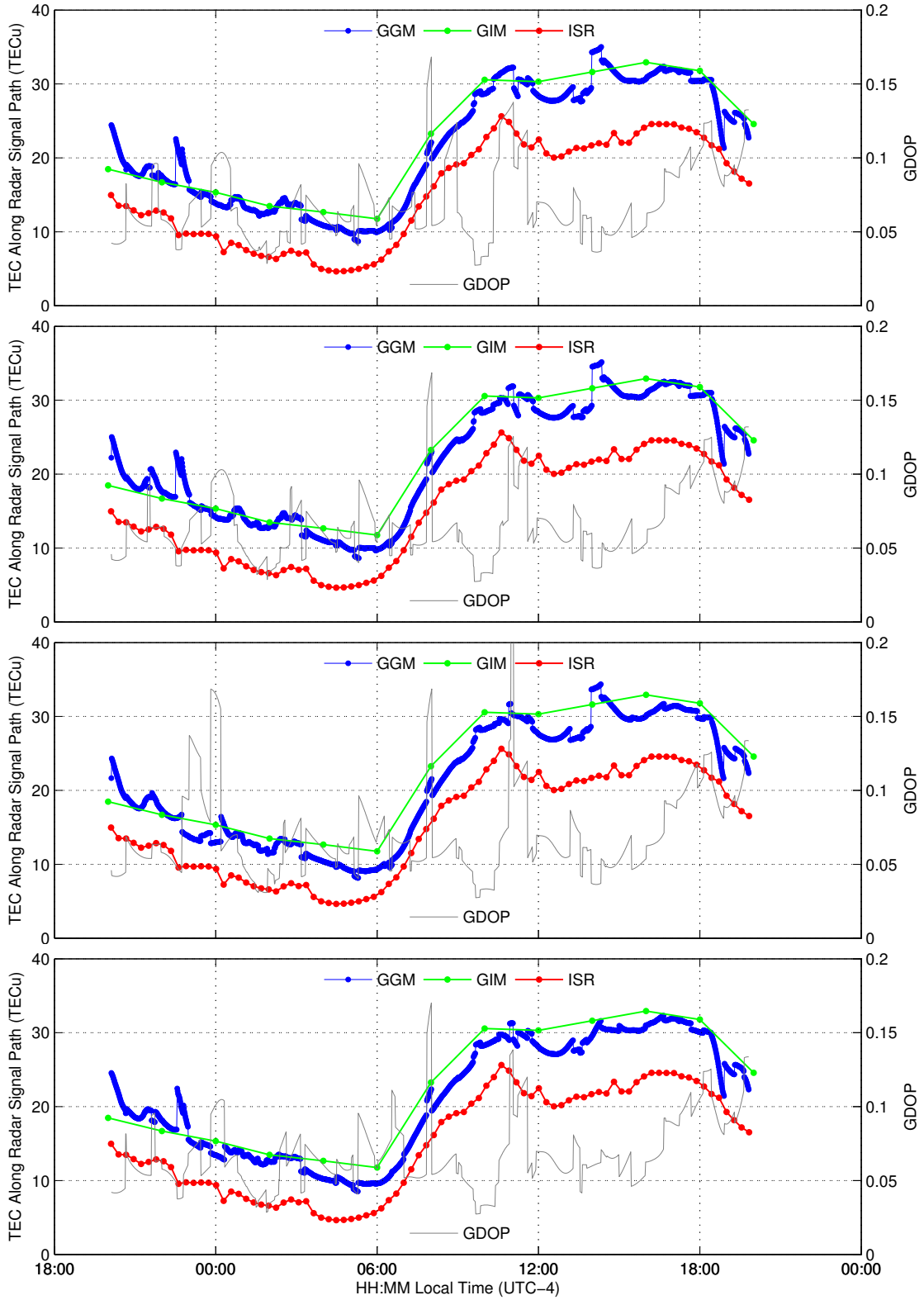
FIGURE 4.2. TEC along NAIC ISR signal path derived from ISR (red), GGM (blue), and GIM (green), as well as the GDOP (gray) for Rx 0 through Rx 3, from top to bottom, January 25.
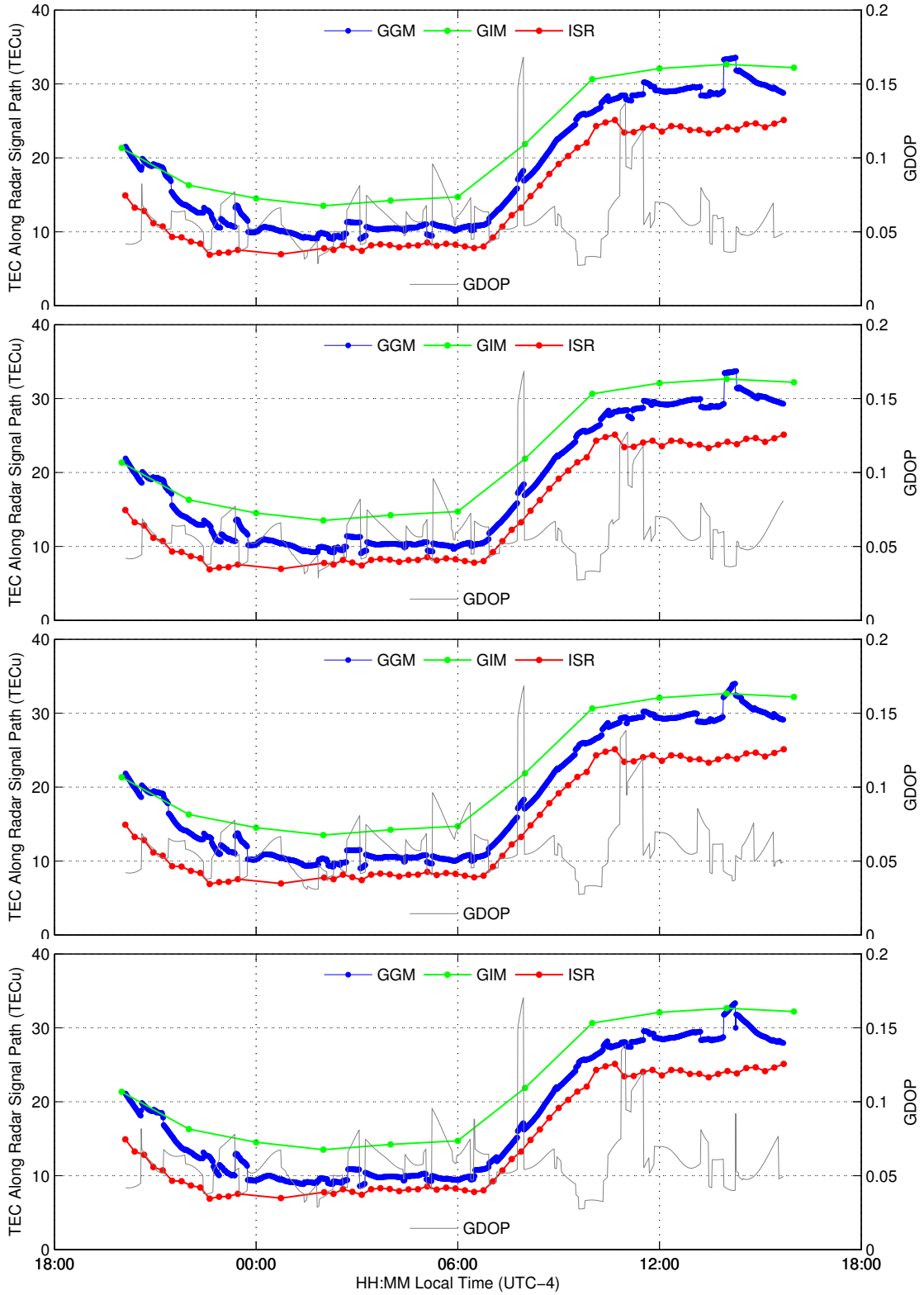
FIGURE 4.3. TEC along NAIC ISR signal path derived from ISR (red), GGM (blue), and GIM (green), as well as the GDOP (gray) for Rx 0 through Rx 3, from top to bottom, January 26.
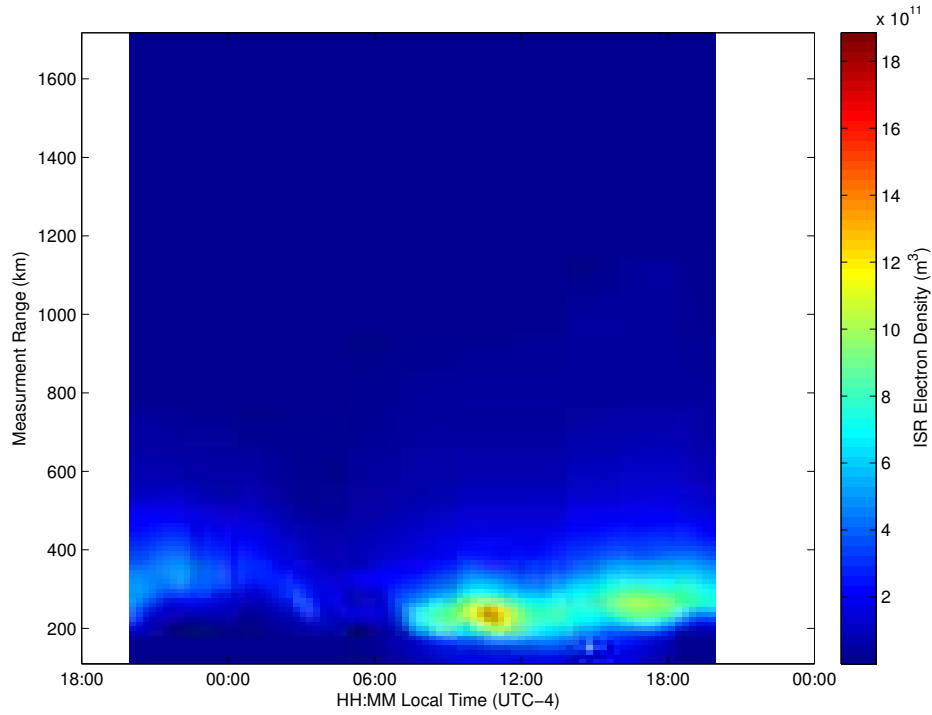
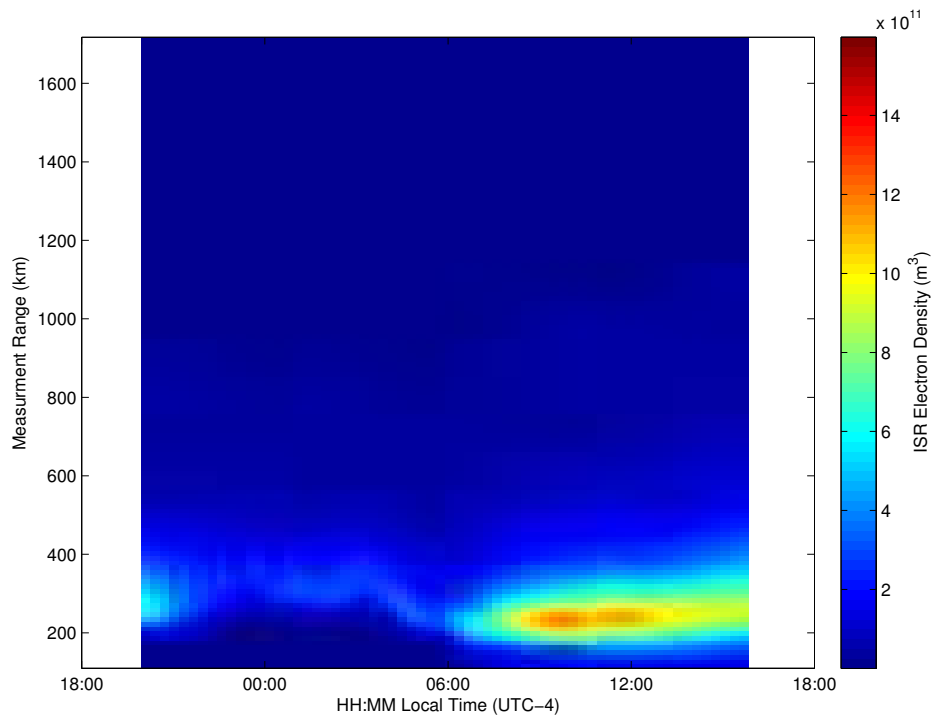FIGURE 4.4. Time series of electron density profiles from the NAIC ISR for January 25.

FIGURE 4.5. Time series of electron density profiles from the NAIC ISR for January 26.

75
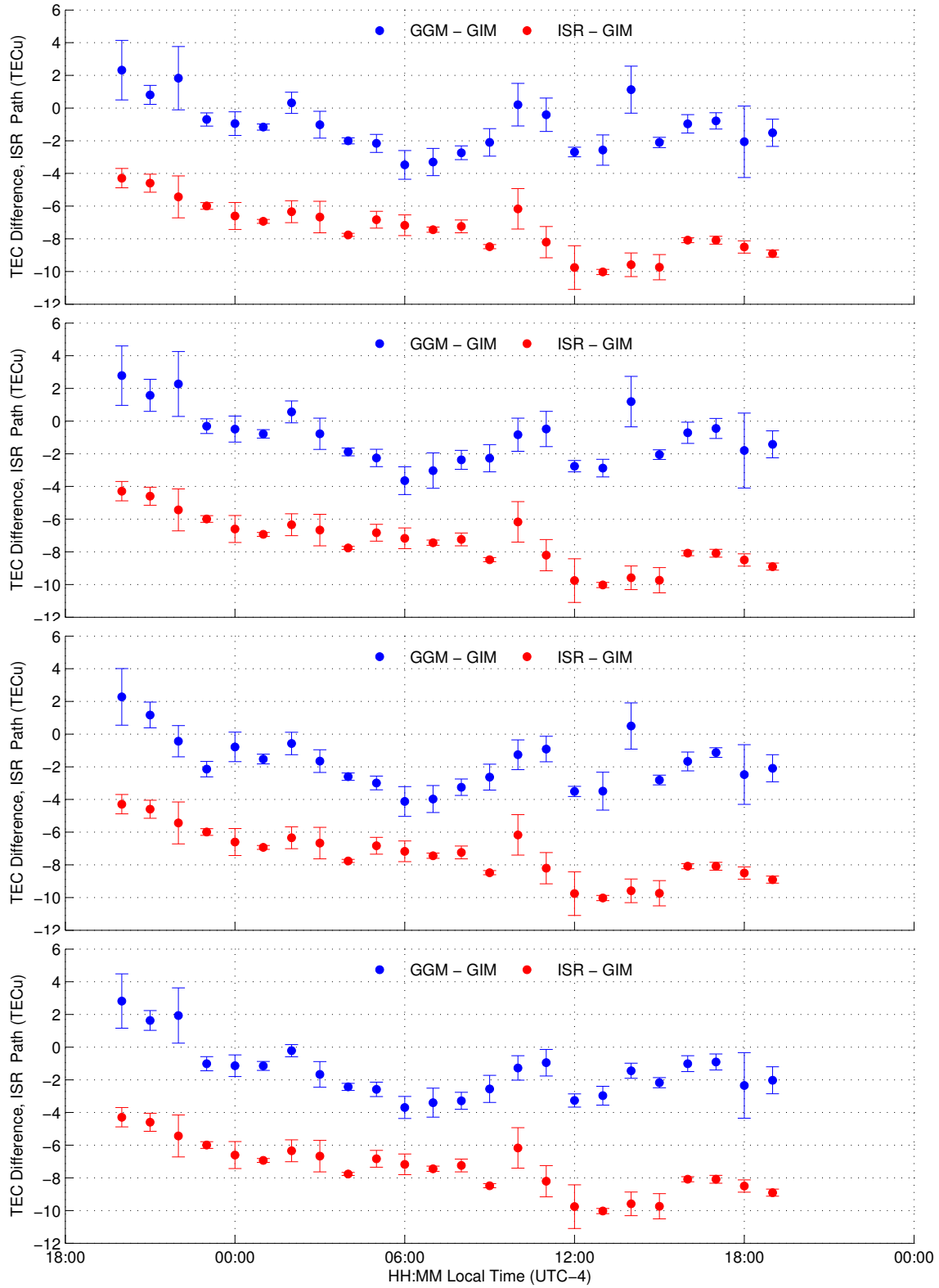
FIGURE 4.6. Difference between the gradient method and IGS map TEC (blue), as well as radar profile and IGS map TEC (red) estimate along the radar signal path. From Rx0 through Rx3, from top to bottom, January 25.

76
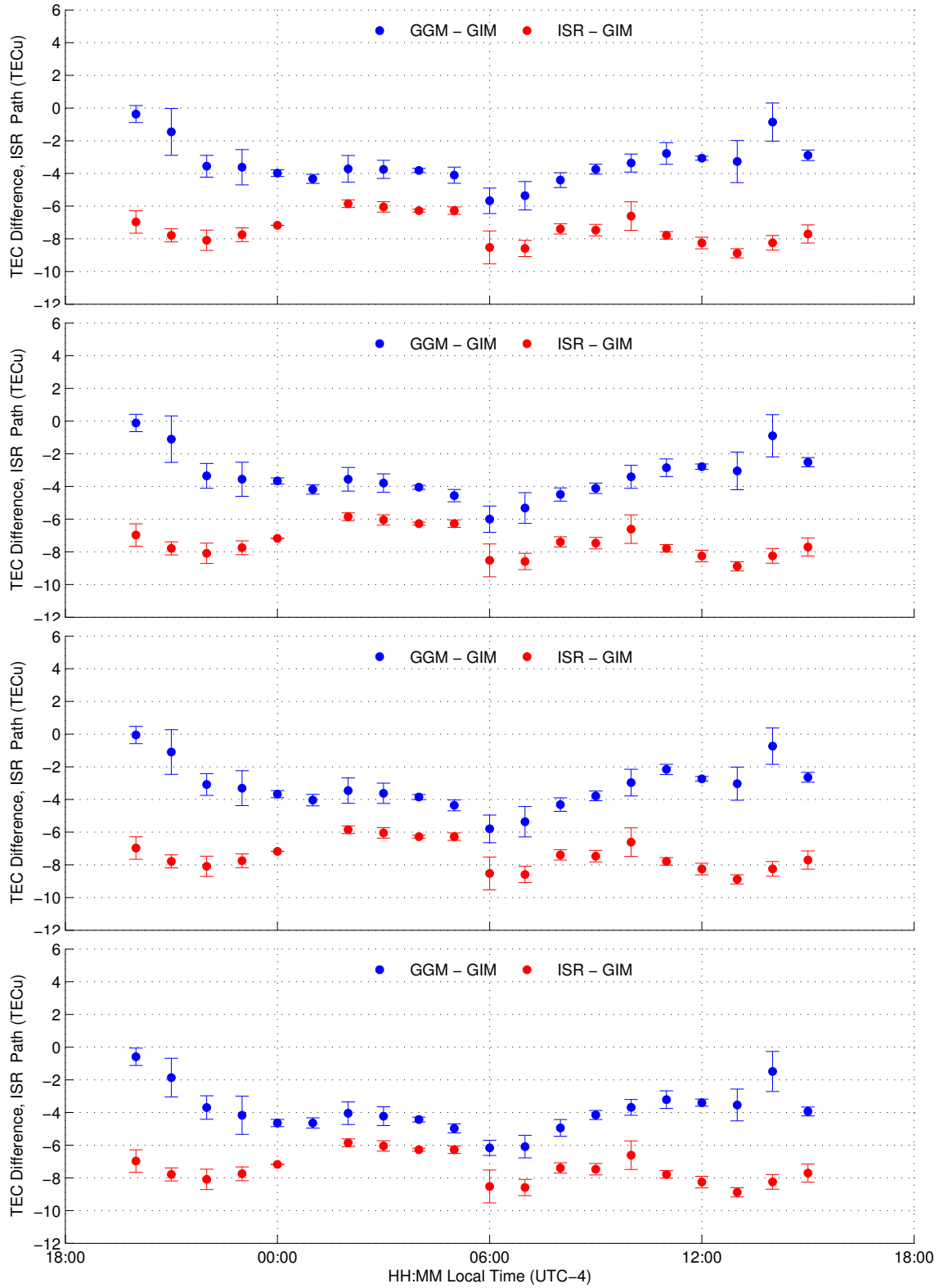
FIGURE 4.7. Difference between the gradient method and IGS map TEC (blue), as well as radar profile and IGS map TEC (red) estimate along the radar signal path. From Rx0 through Rx3, from top to bottom, January 26.
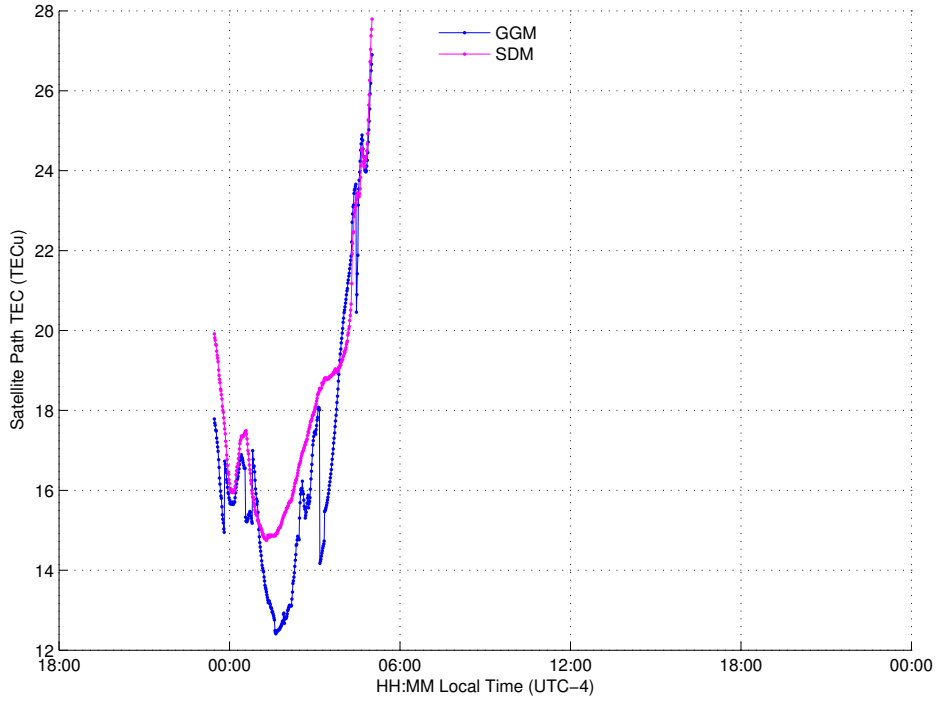
FIGURE 4.8. Comparison between TEC from the GPS gradient method (blue) and standard dual-frequency method (pink) for PRN 7 from the Arecibo receiver (Rx0), January 25.
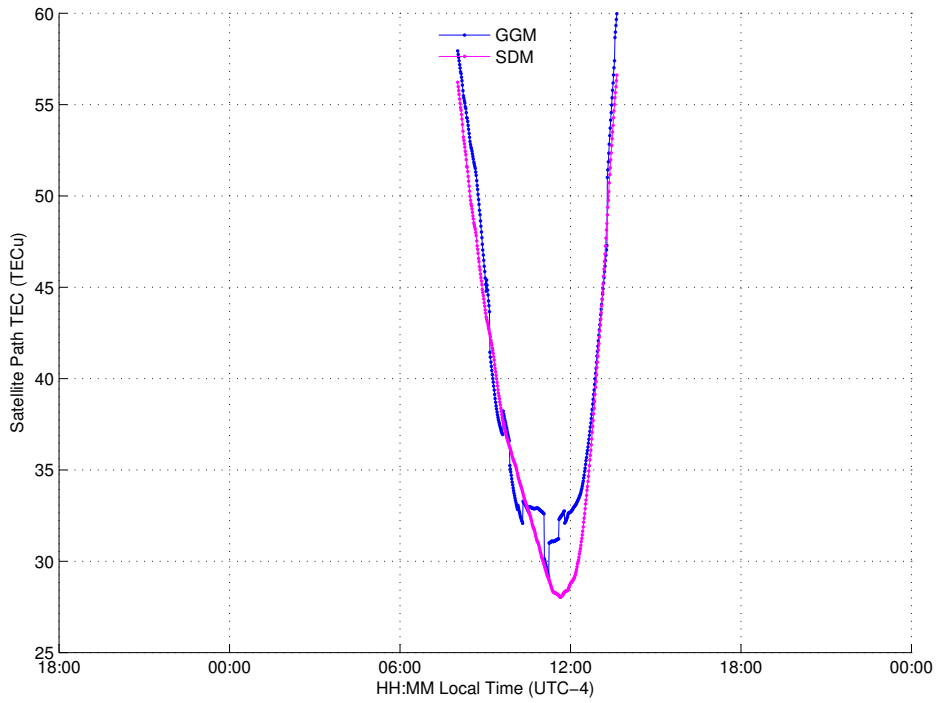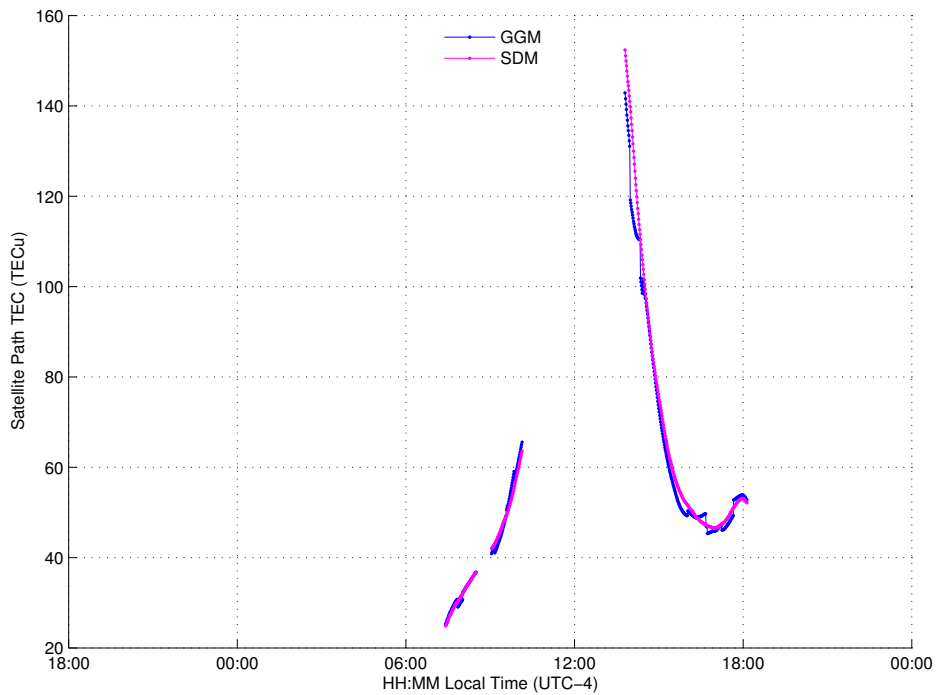

FIGURE 4.9. Comparison between TEC from the GPS gradient method (blue) and standard dual-frequency method (pink) for PRN 26 from the Arecibo receiver (Rx0), January 25.
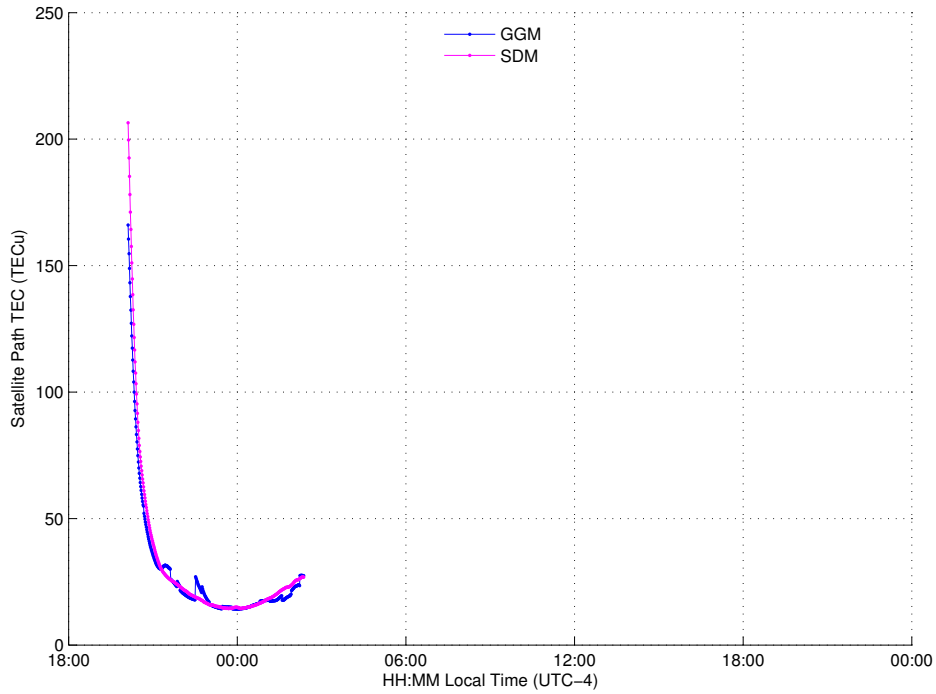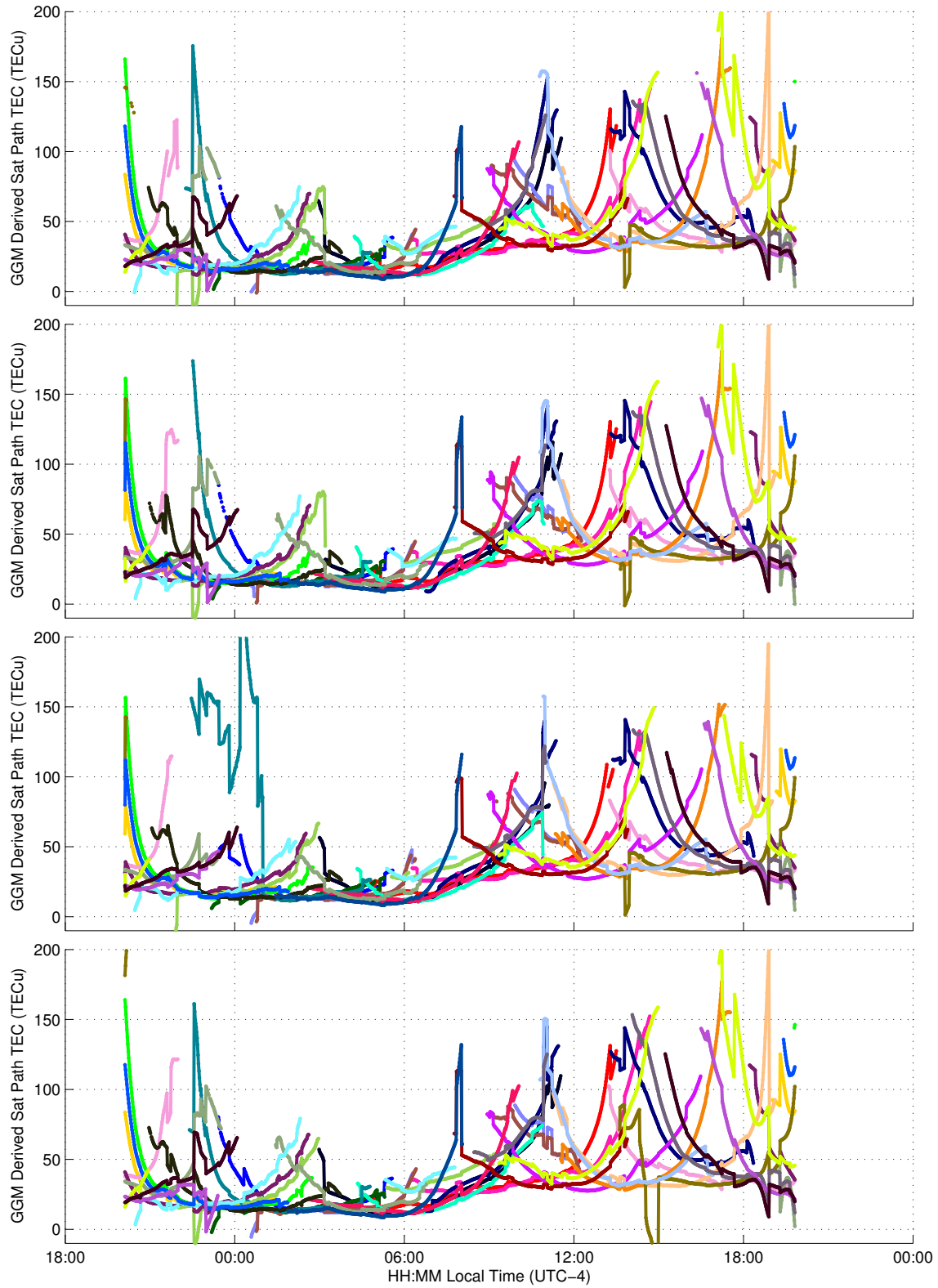
FIGURE 4.10. Comparison between TEC from the GPS gradient method (blue) and standard dual-frequency method (pink) for PRN 3 from the Arecibo receiver (Rx0), January 25.

FIGURE 4.11. Comparison between TEC from the GPS gradient method (blue) and standard dual-frequency method (pink) for PRN 12 from the Arecibo receiver (Rx0), January 25.

FIGURE 4.12. GGM TEC along satellite signal paths over 24 hours from Rx0 through Rx3, from top to bottom, January 25. Each color represents a different satellite.
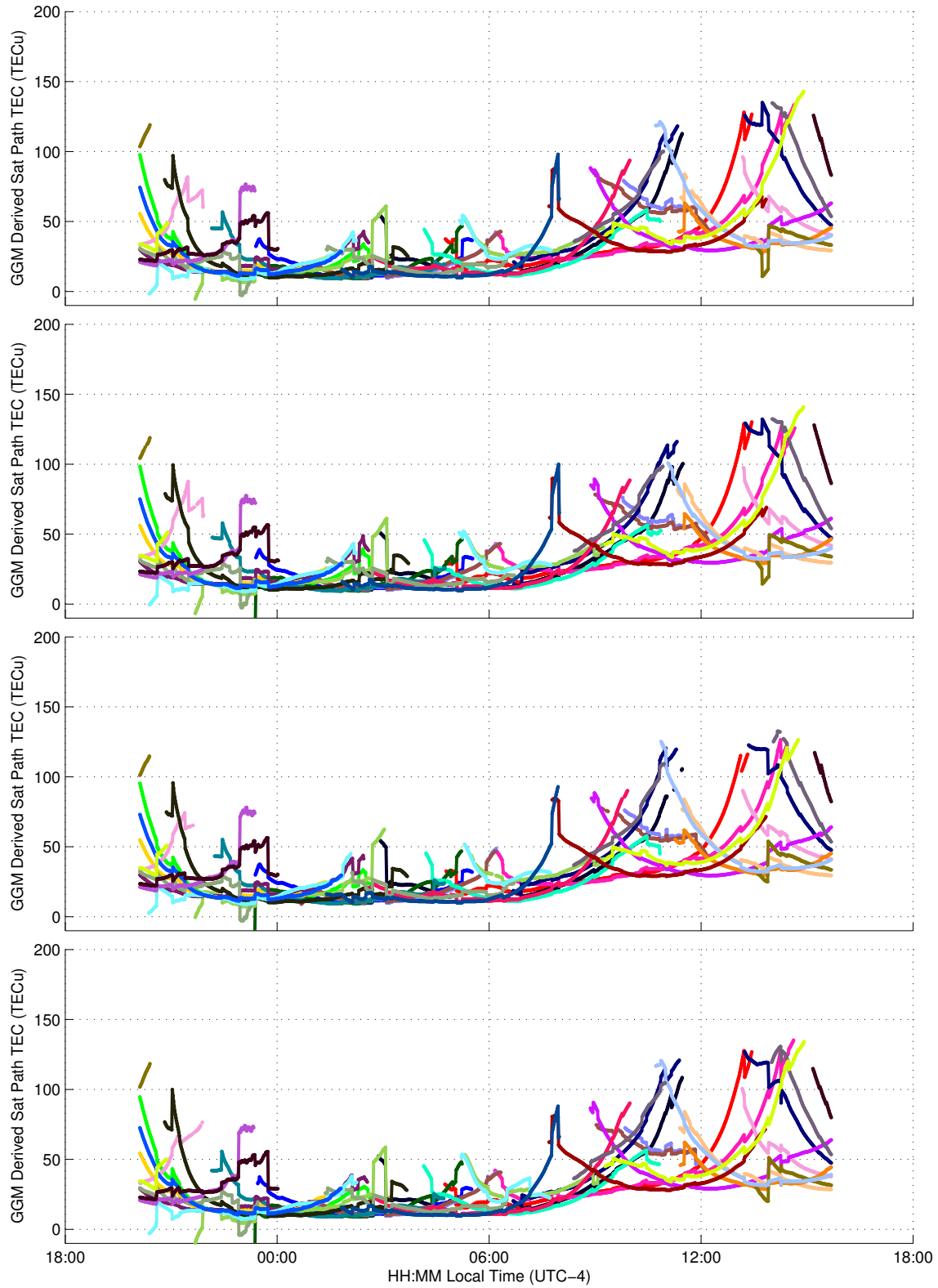
FIGURE 4.13. GGM TEC along satellite signal paths over 24 hours from Rx0 through Rx3, from top to bottom, January 26. Each color represents a different satellite.
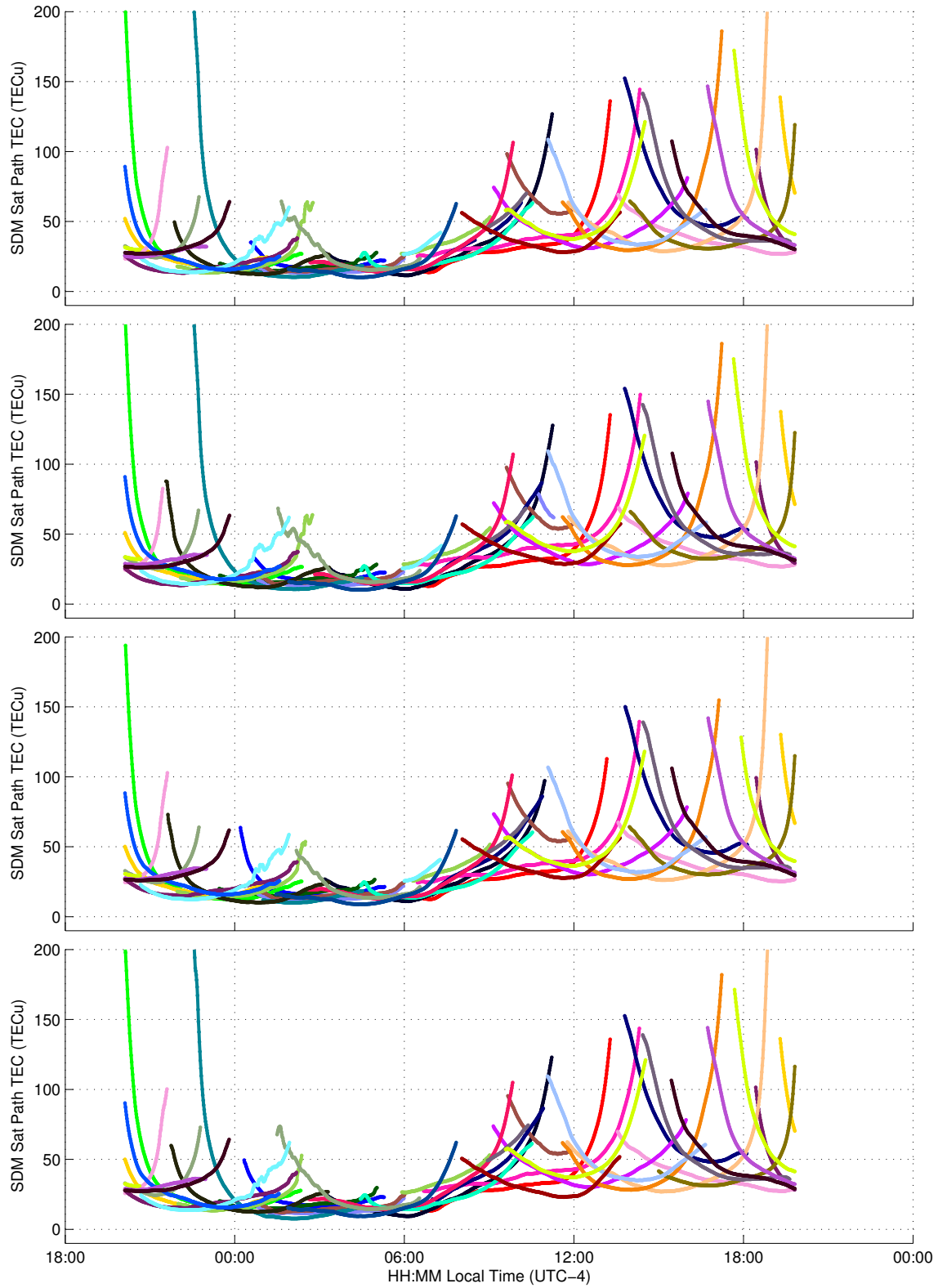
FIGURE 4.14. SDM TEC along satellite signal paths over 24 hours from Rx0 through Rx3, from top to bottom, January 26. Each color represents a different satellite.
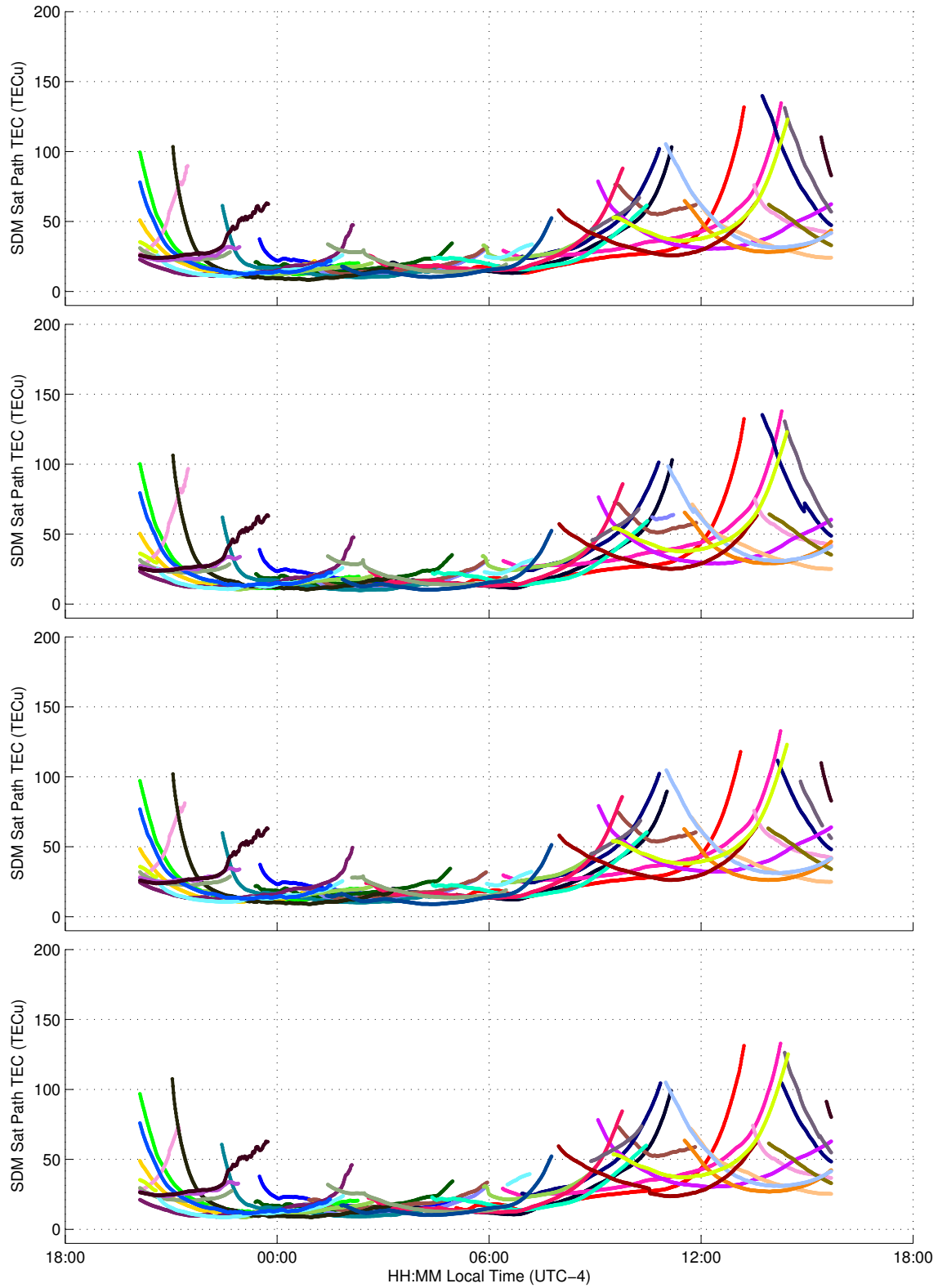
FIGURE 4.15. SDM TEC along satellite signal paths over 24 hours from Rx0 through Rx3, from top to bottom, January 26. Each color represents a different satellite.
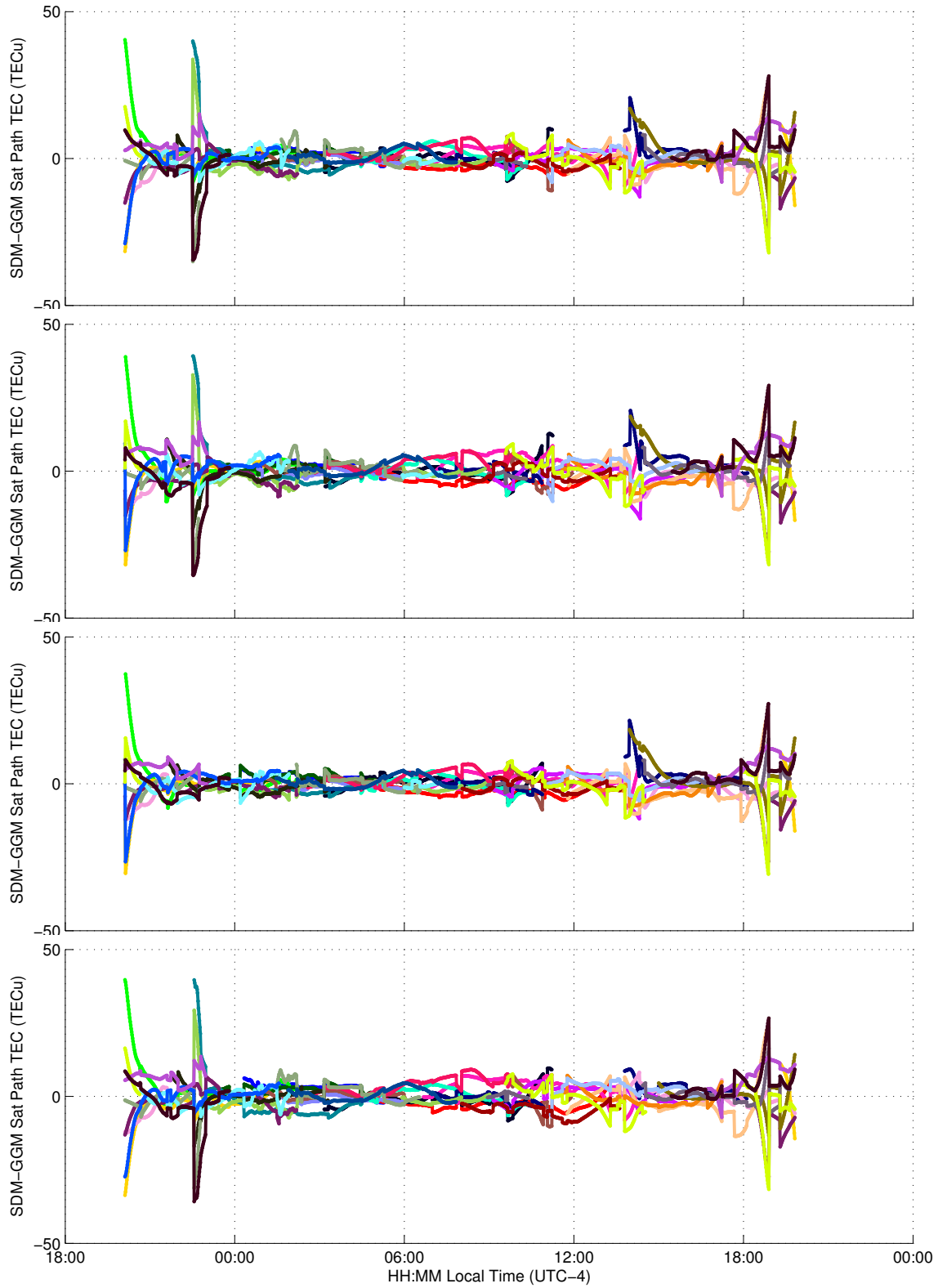
FIGURE 4.16. SDM-GGM TEC difference along satellite signal paths over 24 hours from Rx0 through Rx3, from top to bottom, January 26. Each color represents a different satellite.
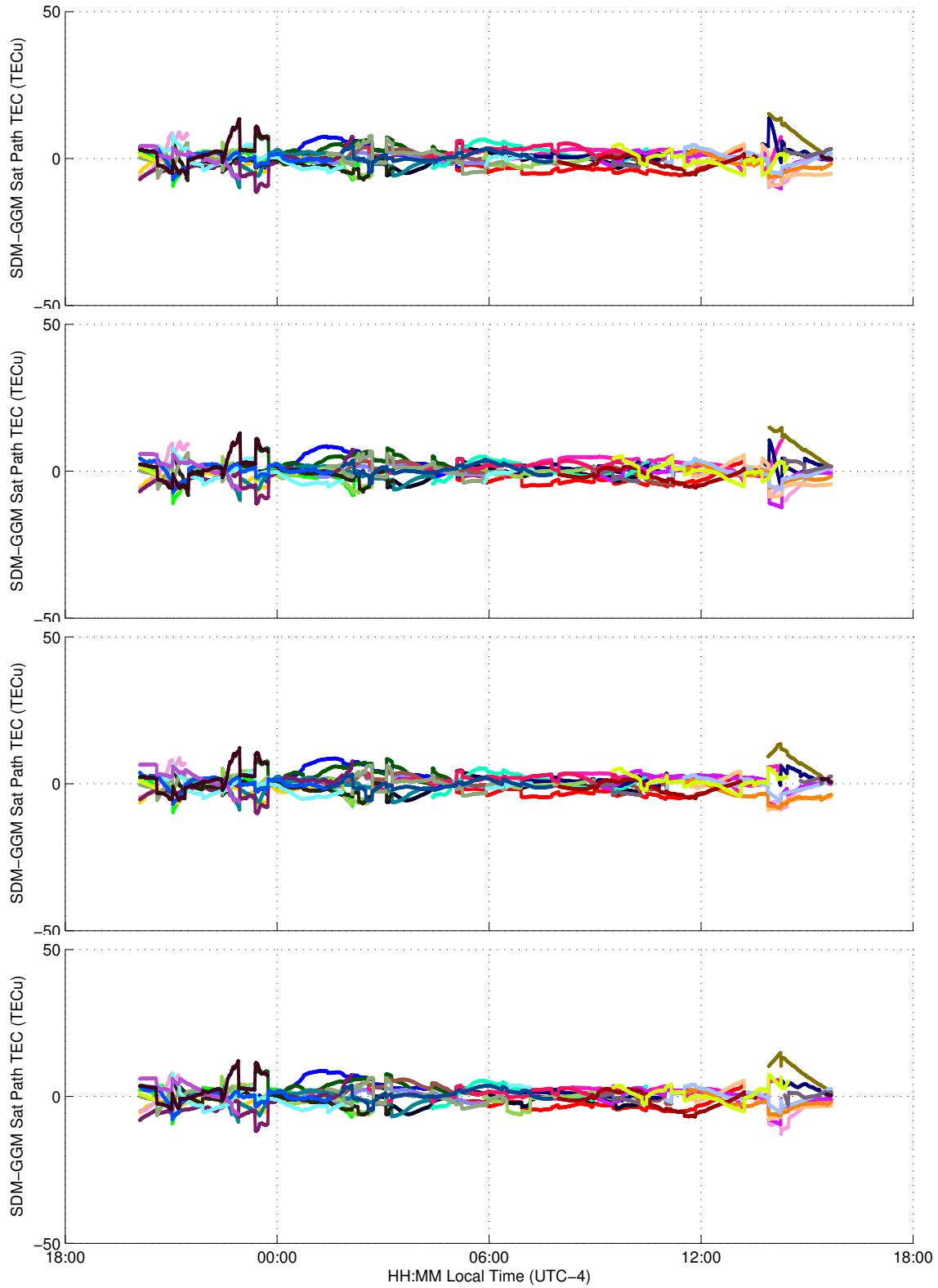
FIGURE 4.17. SDM-GGM TEC difference along satellite signal paths over 24 hours from Rx0 through Rx3, from top to bottom, January 26. Each color represents a different satellite.

FIGURE 4.18. SDM-GGM TEC difference mean and standard deviation along satellite signal paths over 24 hours from Rx0 through Rx3, from top to bottom, January 25. Each color represents a different satellite.
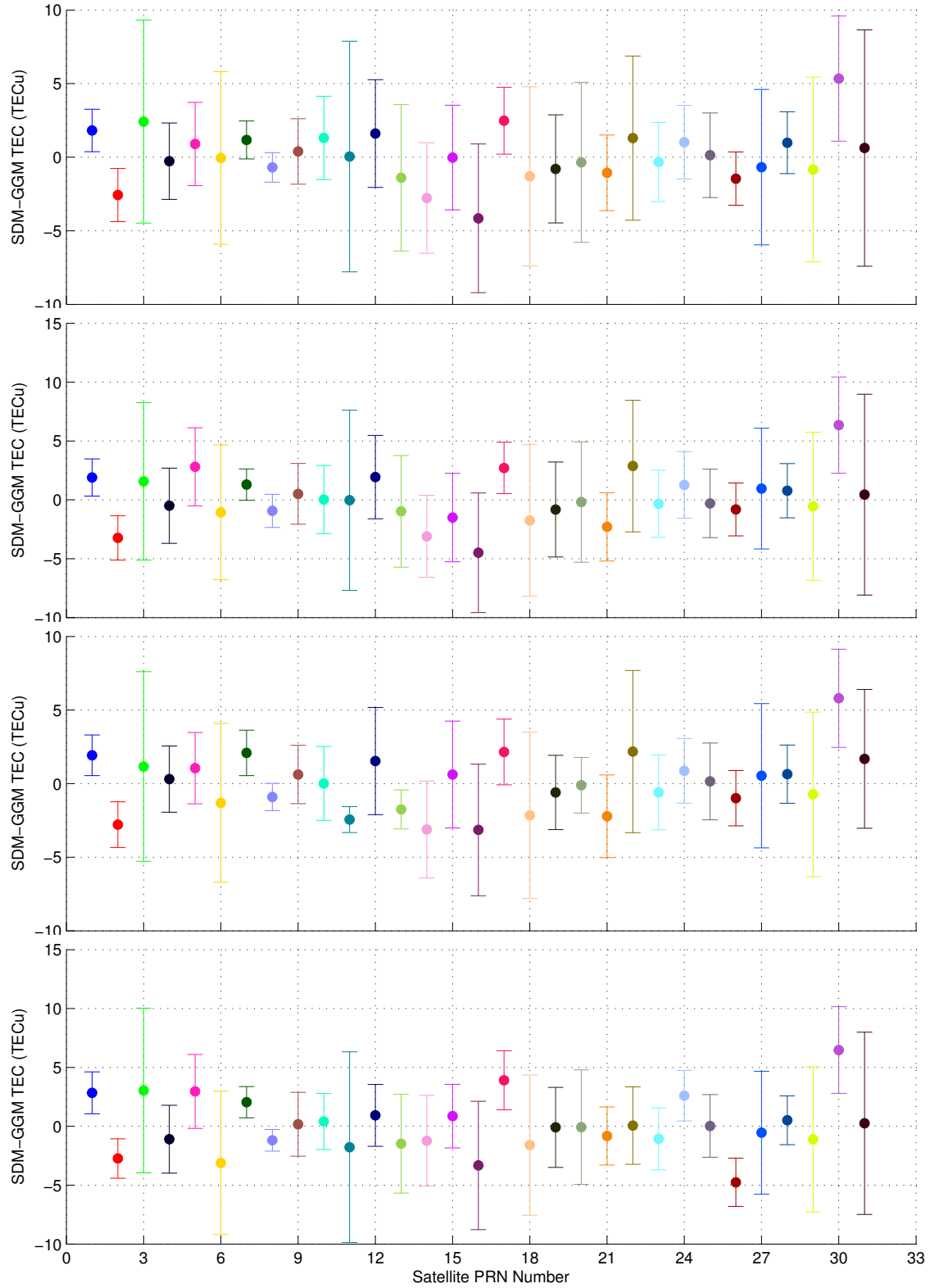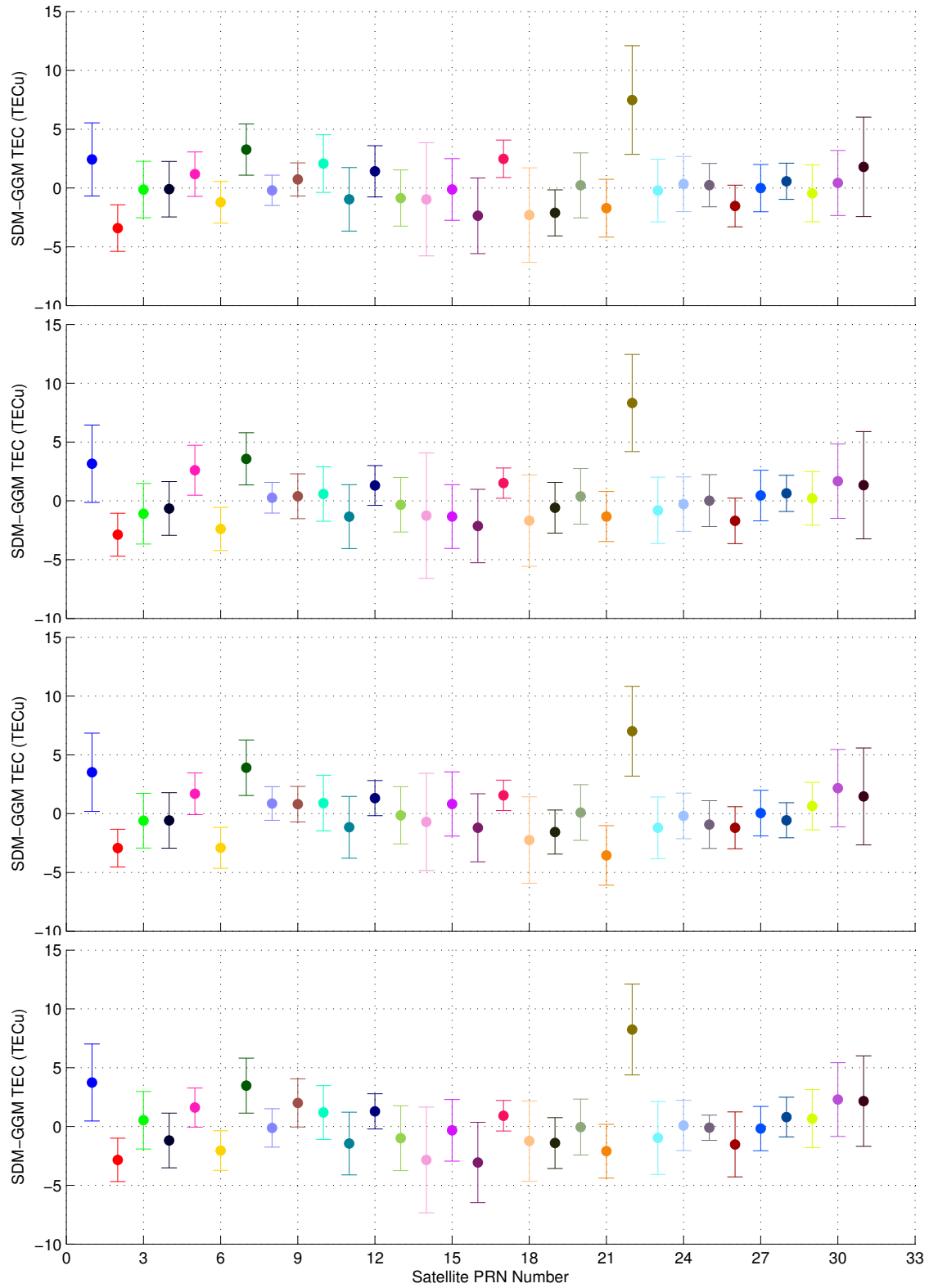
FIGURE 4.19. SDM-GGM TEC difference mean and standard deviation along satellite signal paths over 24 hours from Rx0 through Rx3, from top to bottom, January 26. Each color represents a different satellite.

FIGURE 4.20. Comparison between gradient method and IGS map zenith, latitude and longitude gradients. From Rx0 through Rx3, from top to bottom, January 25.
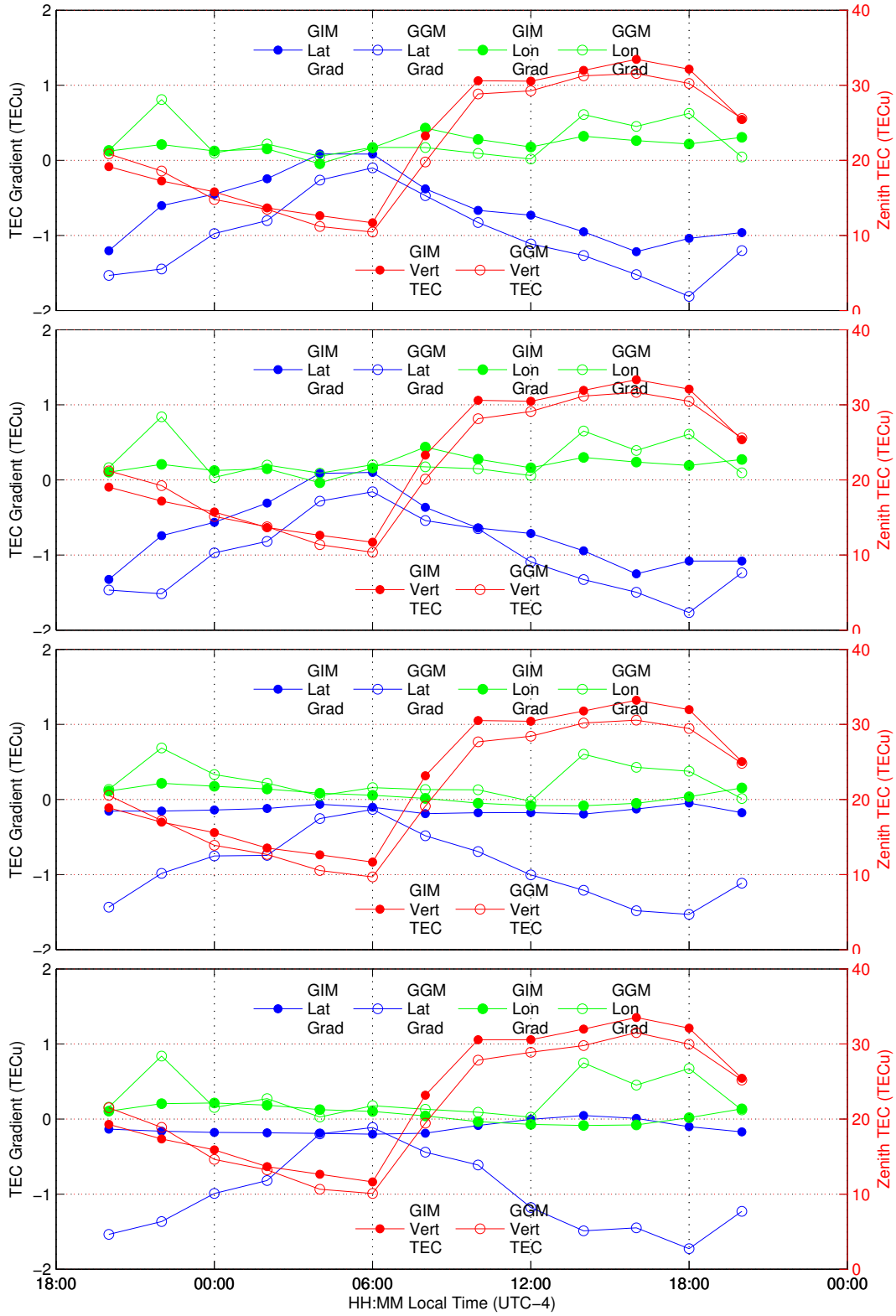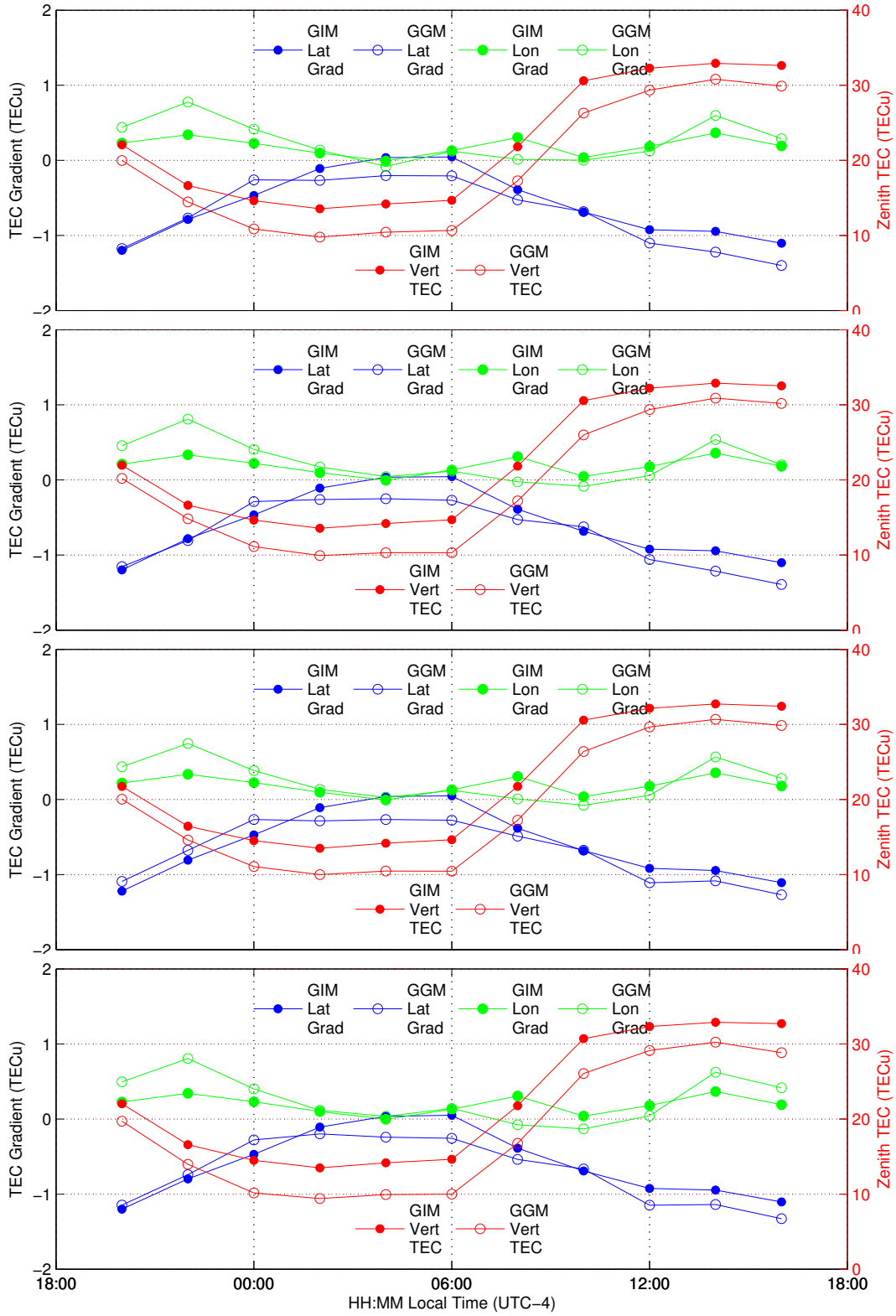
FIGURE 4.21. Comparison between gradient method and IGS map zenith, latitude and longitude gradients. From Rx0 through Rx3, from top to bottom, January 26.

CHAPTER 5

Results: Peru

Contained in this chapter are the results of comparison between GGM, SDM, GIM and
ISR TEC derived from data collected at Jicamarca Radar Observatory in March, 2013. The
results presented cover two 24 hour periods, one 19 hour period, and one 9 hour period. The
GPS satellite passes which occurred on the first day are shown in figure 5.1. The satellite
passes on the subsequent days are almost identical and are therefore not shown.
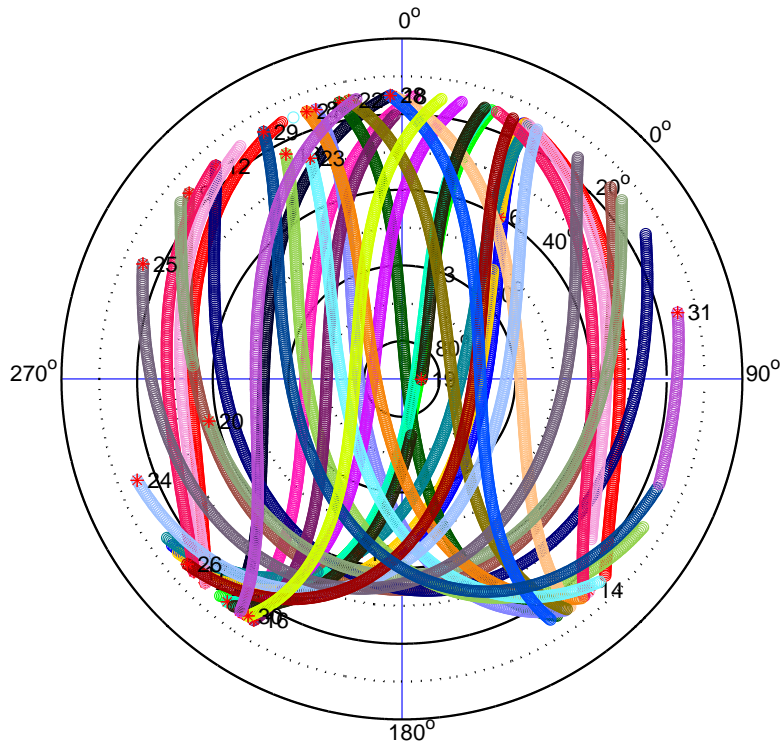
Figure 5.1. GPS satellite paths across the sky for 24 hours from JRO, March
7, 2013. Each color represents a different satellite.

One important thing to note about the ISR results in this chapter is that some processing
has been done to remove erroneous measurements. To illustrate these, a time series plot of
the uncorrected profiles from March 7 is shown in figure 5.2. These problem measurements
are most prevalent at the lowest altitude bin of the profiles at approximately 105 km altitude.

For this reason, that bin is set to zero for every profile. In addition, measurements grater than $3 \times 10^{12} \frac{n_e}{m^2}$ are set zero. The effect of the corrections can be seen through comparison with 5.4.
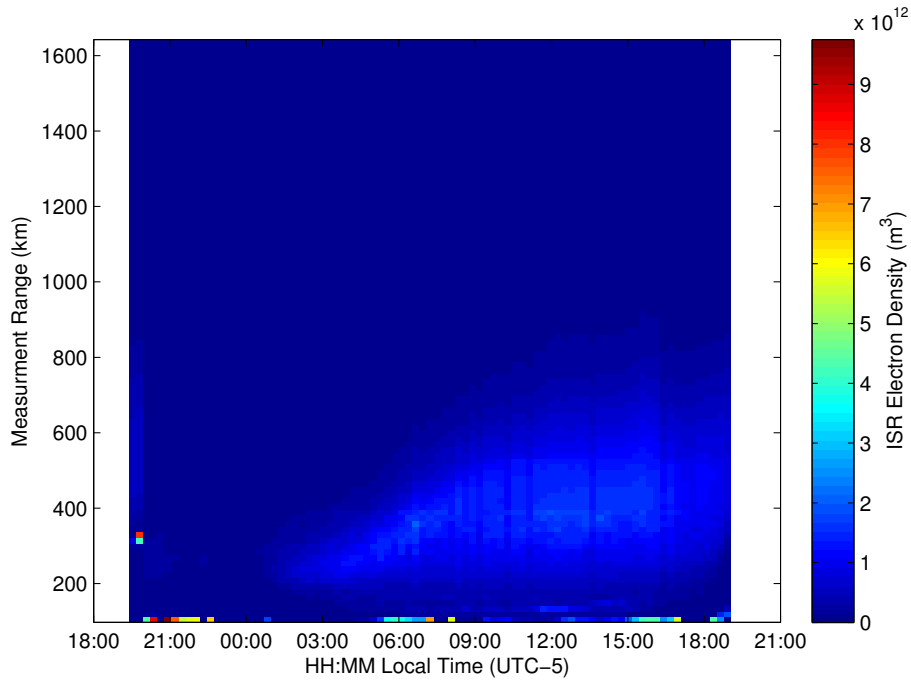

FIGURE 5.2. Time series of uncorrected electron density profiles from the JRO ISR, March 7.

Figure 5.3 gives a direct comparison of the GGM, GIM, and ISR TEC. The plots compare the three TEC measurement types over four days and the GDOP. The notable features of these plots are discussed below.

In the first two plots, and the last plot, the visual correspondence is relatively close between all three methods. The GIM and GGM have the same general trend as in the other receiver locations. However the the GIM is unable to keep pace with the large fluctuations which occur in the hours before midnight. Unfortunately ISR data is unavailable during this period, so the validity of these fluctuations cannot be ascertained. The GIM does somewhat mimic the trend to some extent.

The GIM and GGM do encounter a consistent discrepancy on March 11 which may be explained by inaccurate IFB estimation due to not solving over a full 24 hours. This supposition is born out by the IFB values on table 5.1, which shows the march 11 IFB more than two and a half TECu under the next lowest estimate.

Table 5.1. Inter-frequency bias estimate for Jicamarca GPS receiver.

March 7	March 11	March 12	March 13
-15.51 TECu	-11.73 TECu	-17.15 TECu	-18.00 TECu

Unfortunately the ISR data from JRO is extremely noisy, likely due to the coherent scatter which occurs at the magnetic equator as discussed in section 2.1.4. This makes it difficult make any judgement about the accuracy of GGM estimation of fine structures present in the ionosphere. However, no real small scale structures occur at JRO, not even the geometry induced fluctuations prevalent in both the Alaska and Puerto Rico data. This is possibly because the larger diurnal variation of the TEC masks the geometry variation. It could also be due to the better receiver environment at Jicamarca containing fewer obstructions. However, since the multipath has been mostly removed, the environment should have a negligible effect. Another possibility is the denser satellite coverage of the equatorial region help to decrease the GDOP, although the difference is not apparent from figure 5.2.

The relatively unreliable nature of the ISR measurements at JRO can be seen in the density profile time series for each day seen in figures 5.4, 5.5, 5.6, and 5.7. All four days show clear discontinuities between profiles at multiple times throughout the day. These effects are most likely due to phenomena such as the electrojet and coherent scatter from spread-F events which occur on the magnetic equator where JRO is located.

It is interesting to note that some small scale fluctuations in the GGM TEC occur around local midnight. A similar, but less intense, occurrence can also be observed at NAIC around local midnight as seen in figures 4.2 and 4.3.

The general trend of the ISR and GGM TEC also appear to match well, and even the values are over the long term quite similar. This is somewhat strange, as the JRO ISR is not able to measure as high as NAICs, which is consistently below the GGM and GIM measurements. This can also be observed in figure 5.8 where the GGM and ISR with GIM subtracted are often within five TECu of each other, and, many times, less.

A more qualitative view of the comparison between the three measurement methods is in table 5.2. The table shows that the ISR and GGM TEC are, in general, closer than the GGM and GIM, which is unique among the three locations studied. The agreement between the GGM and GIM is broadly similar to what was seen on Purto Rico and not nearly as good as at Poker. The ISR, GIM agreement is relatively consistent in being the worst across all three sites.

TABLE 5.2. RMS error between TEC measurement methods during March 2013 at Jicamarca, Peru.

	ISR-GGM	GGM-GIM	ISR-GIM
March 7	4.443 TECu	7.331 TECu	7.727 TECu
March 11	4.145 TECu	7.477 TECu	7.347 TECu
March 12	5.766 TECu	4.457 TECu	8.218 TECu
March 13	6.610 TECu	3.666 TECu	9.167 TECu

Figures 5.9, 5.10, 5.11, and 5.12 present a comparison between the GGM and SDM TEC estimates for four selected satellites. The first two plots were chosen because they represent poor concurrence, and the second two, good concurrence. Finding satellites with agreement problems was more difficult for the JRO data as most instances concurred well. Figure 5.9 was the only instance of poor agreement at the apex of the satellite path. Figure 5.10 shows

problems where they are to be expected, a satellite close to the horizon which has wildly fluctuating TEC. The plots also show far less of the geometry induced fluctuation seen in even the best of the NAIC and PFRR measurements.

The remarkable lack of the geometry fluctuations is even better illustrated by comparing figure 5.13 and 5.14. The results obtained by the GGM and SDM are quite similar, and the GGM result is remarkably smooth in comparison the other receiver locations. The picture is less pretty when looking at the difference of the two, figure 5.15, with significant variation between the two, especially around local midnight. The local midnight occurrence is expected as ionosphere seems to be more variable at that time, as variations are visible in the SDM as well as GGM. Outside of this period, fluctuation is much more limited, with around 10 TECu of range. The less significant geometry induced fluctuations at JRO may be due to a more uniform distribution of satellites. Further investigation is needed to determine if this is in fact the case.

The less significant variation in the GGM result is also evident in figure 3.15. The mean of the SDM-GGM difference is slightly smaller for the JRO data with the mean range being about eight TECu. However the standard deviation is significantly smaller at JRO with the largest being about ten TECu. Again more work is needed to determine why the JRO result is better than either of the other locations.

The comparison of the GIM and GGM gradient and zenith TEC values at JRO also shows promising results. The general trends and values of all three parameters are broadly similar, even with the significant range of variation experienced. The longitude gradient is especially variable as it covers the entire range of gradient values throughout the day.
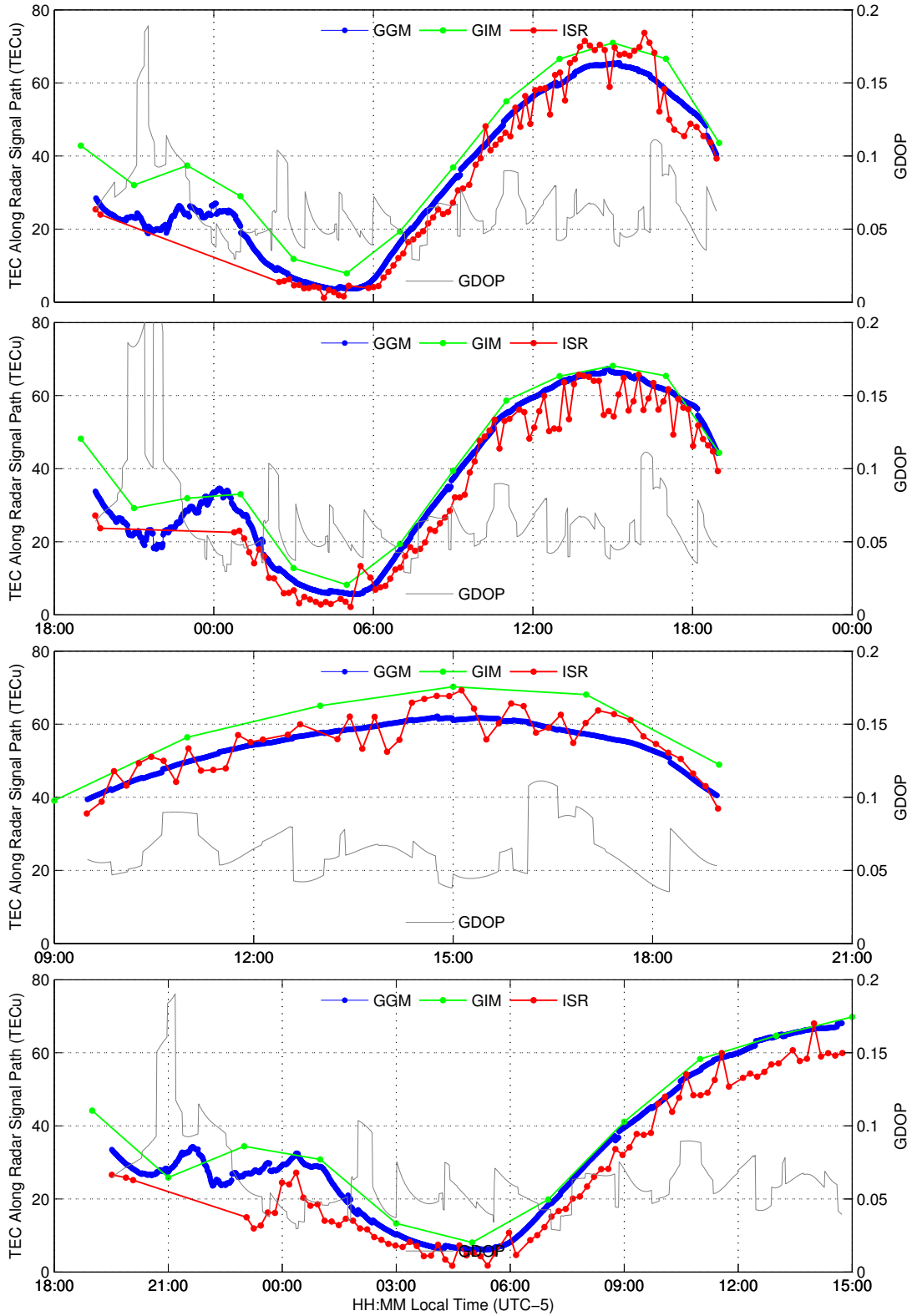
FIGURE 5.3. TEC along JRO ISR signal path derived from ISR (red), GGM (blue), and GIM (green), as well as the GDOP (gray) for March 7, 12, 11, and 13, top to bottom.
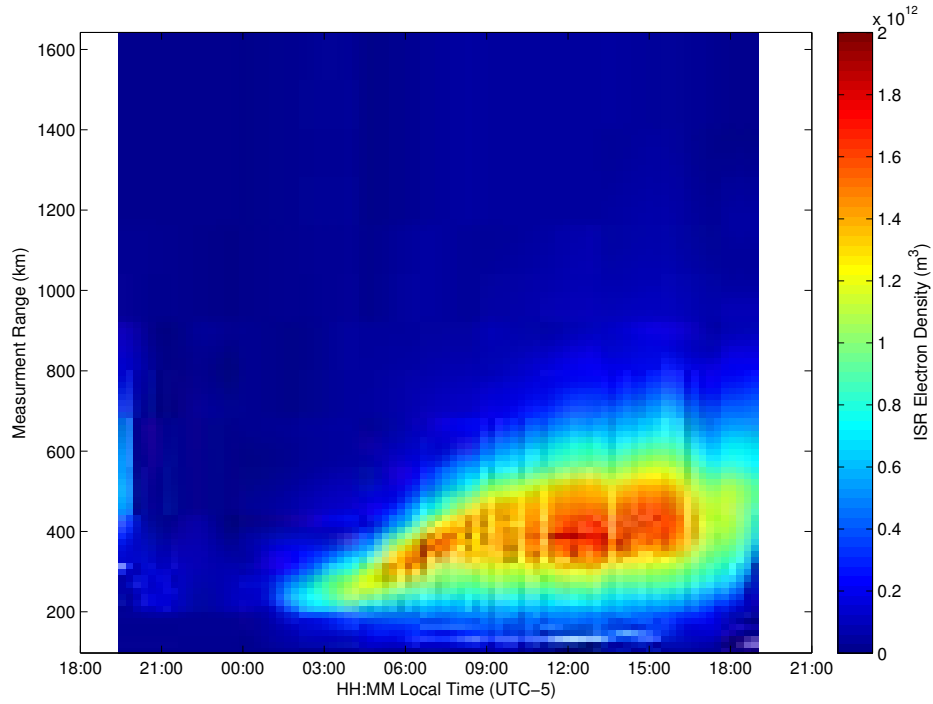
FIGURE 5.4. Time series of electron density profiles from the JRO ISR for March 7.
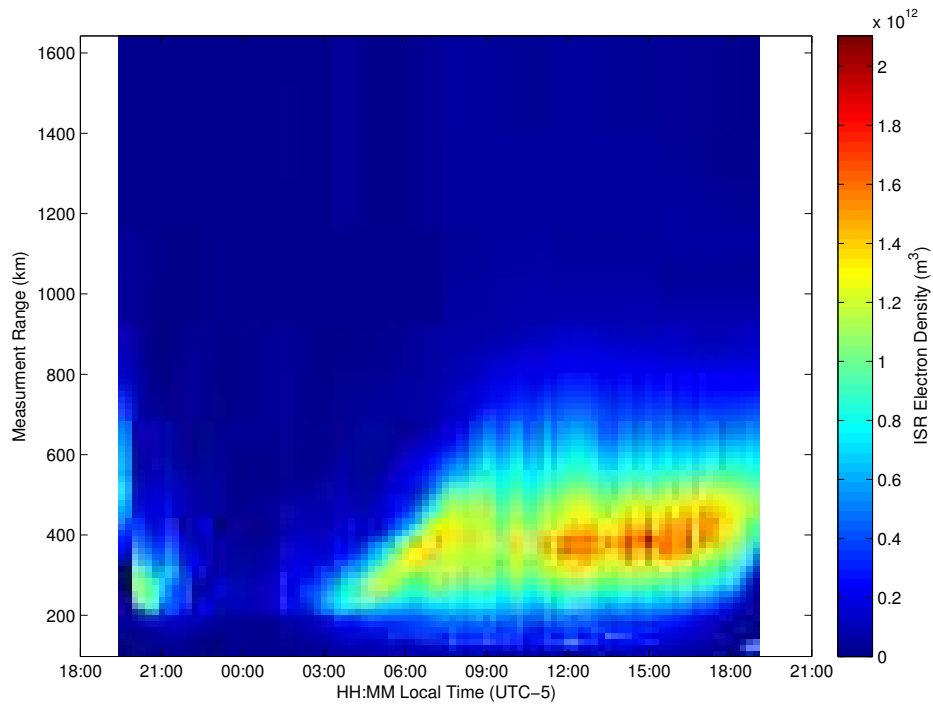

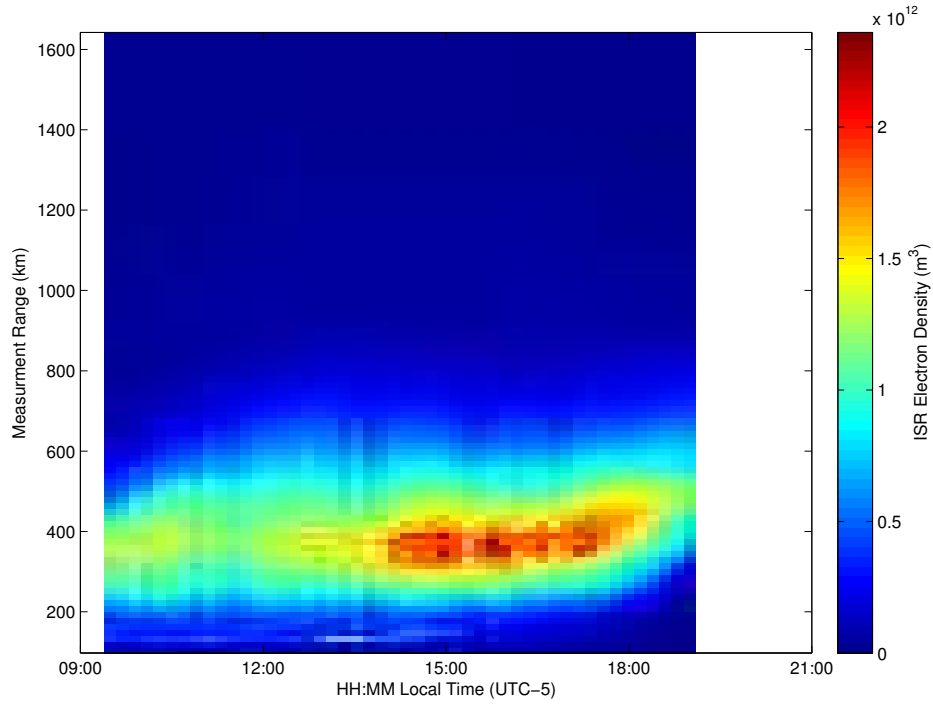FIGURE 5.5. Time series of electron density profiles from the JRO ISR for March 12.

FIGURE 5.6. Time series of electron density profiles from the JRO ISR for March 11.
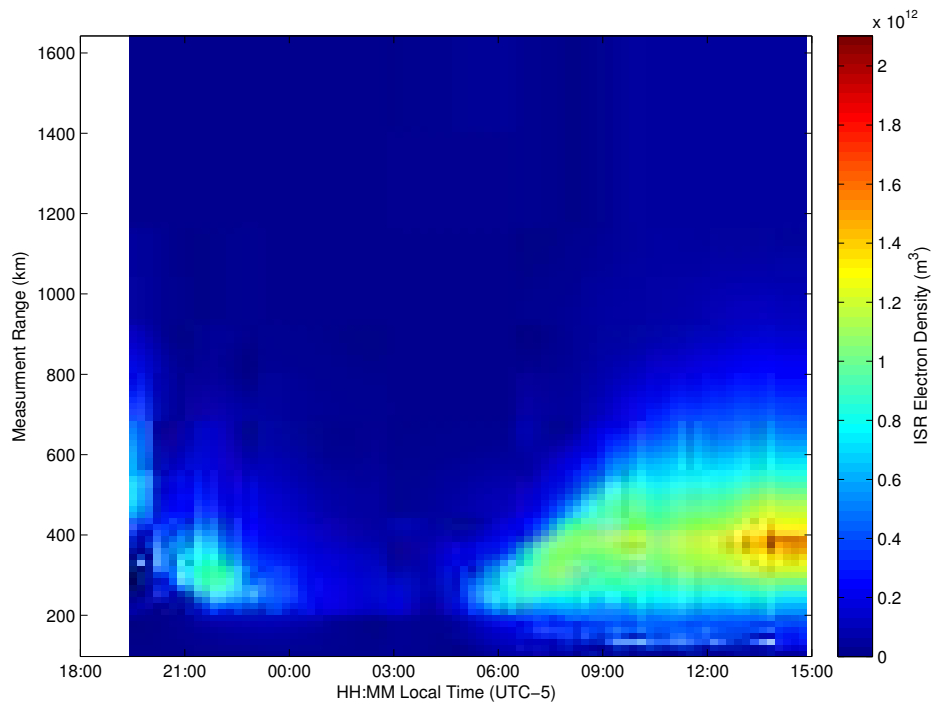

FIGURE 5.7. Time series of electron density profiles from the JRO ISR for March 13.
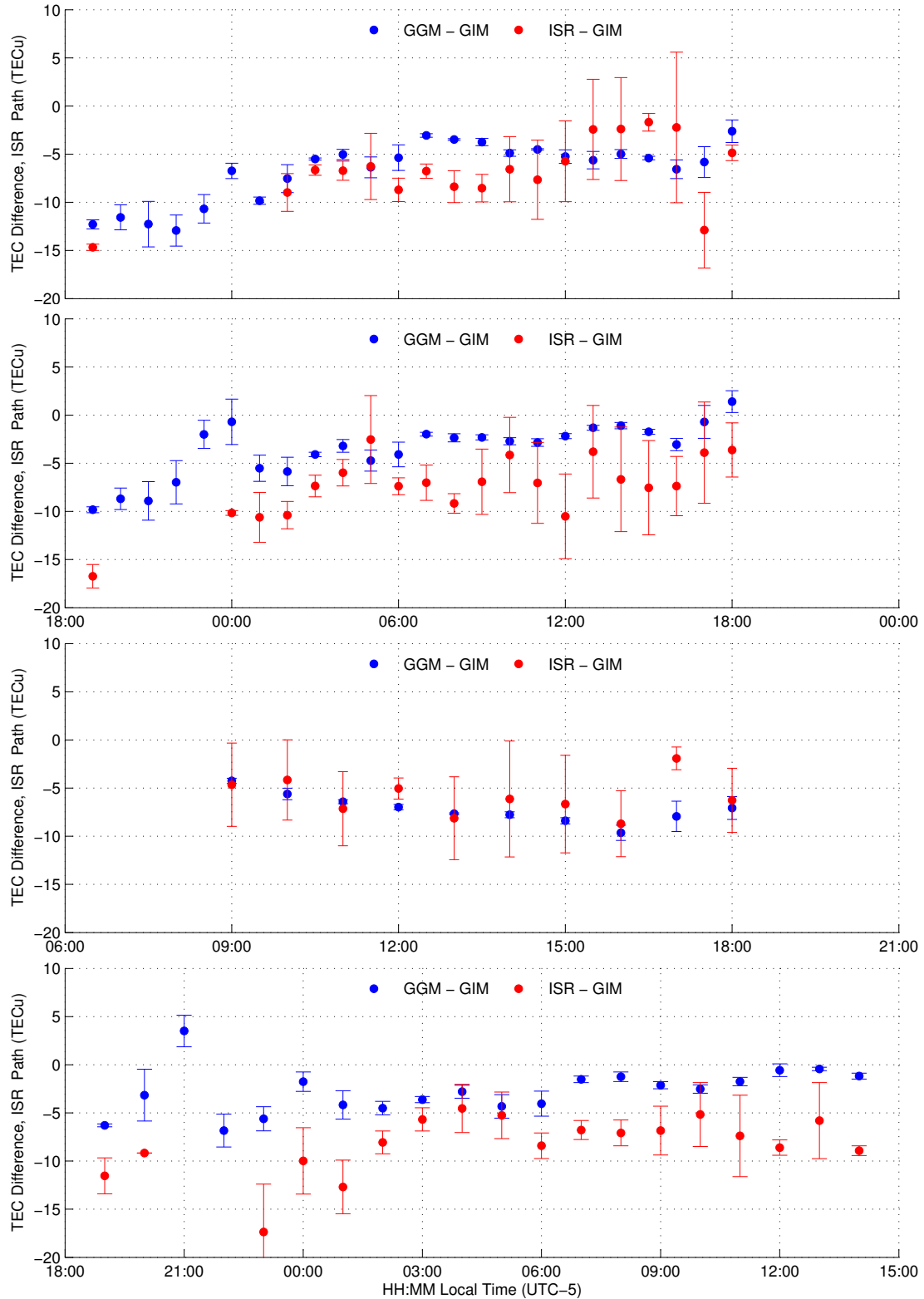
FIGURE 5.8. Difference between GGM and IGS map TEC (blue), as well as radar profile and IGS map TEC estimate (red) along the radar signal path. From JRO, March 7, 12, 11, and 13, top to bottom.

FIGURE 5.9. Comparison between TEC from the GPS gradient method (blue) and standard dual-frequency method (pink) for PRN 5 from JRO, March 7.

FIGURE 5.10. Comparison between TEC from the GPS gradient method (blue) and standard dual-frequency method (pink) for PRN 13 from JRO, March 7.
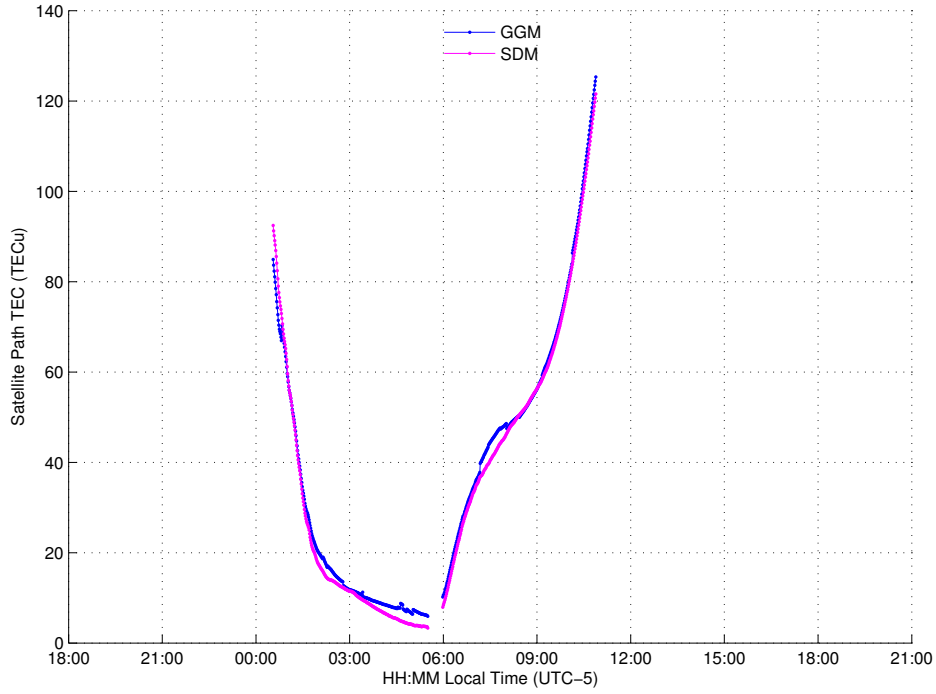
FIGURE 5.11. Comparison between TEC from the GPS gradient method (blue) and standard dual-frequency method (pink) for PRN 2 from JRO, March 7.
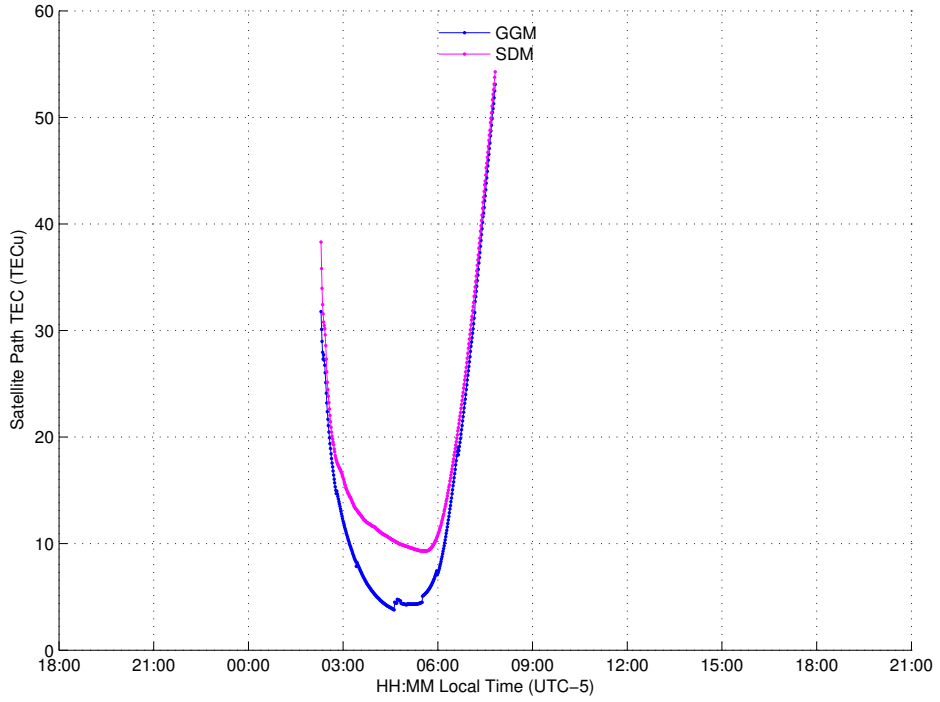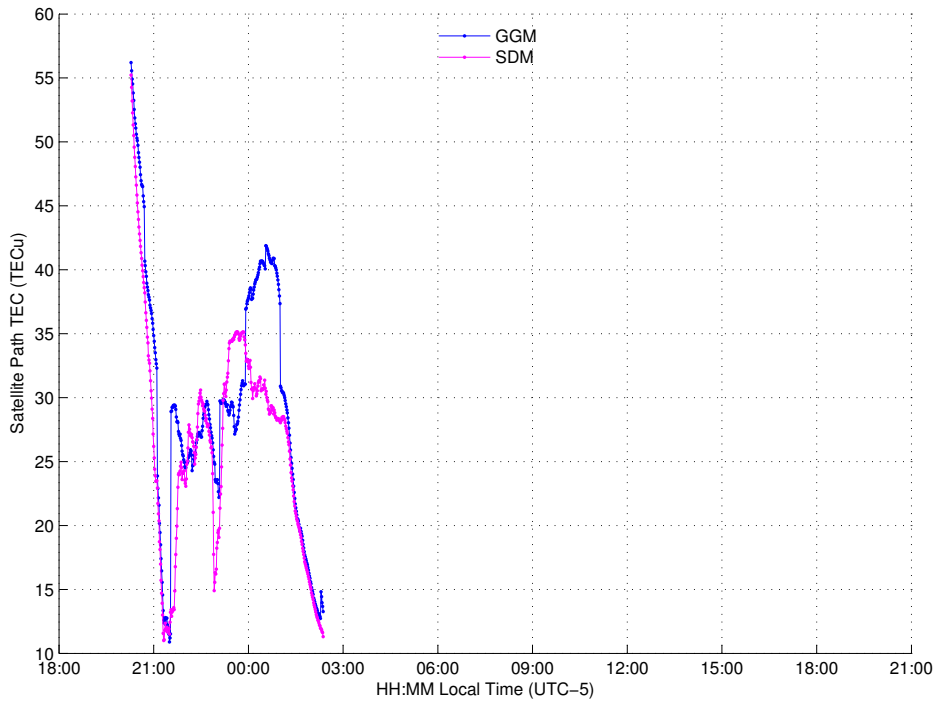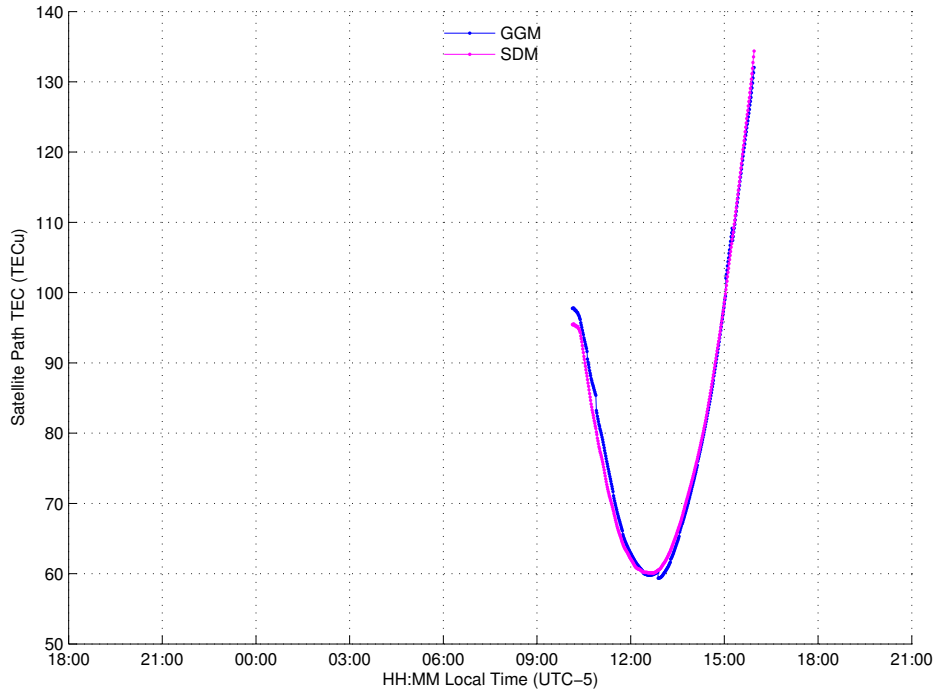

FIGURE 5.12. Comparison between TEC from the GPS gradient method (blue) and standard dual-frequency method (pink) for PRN 21 from JRO, March 7.
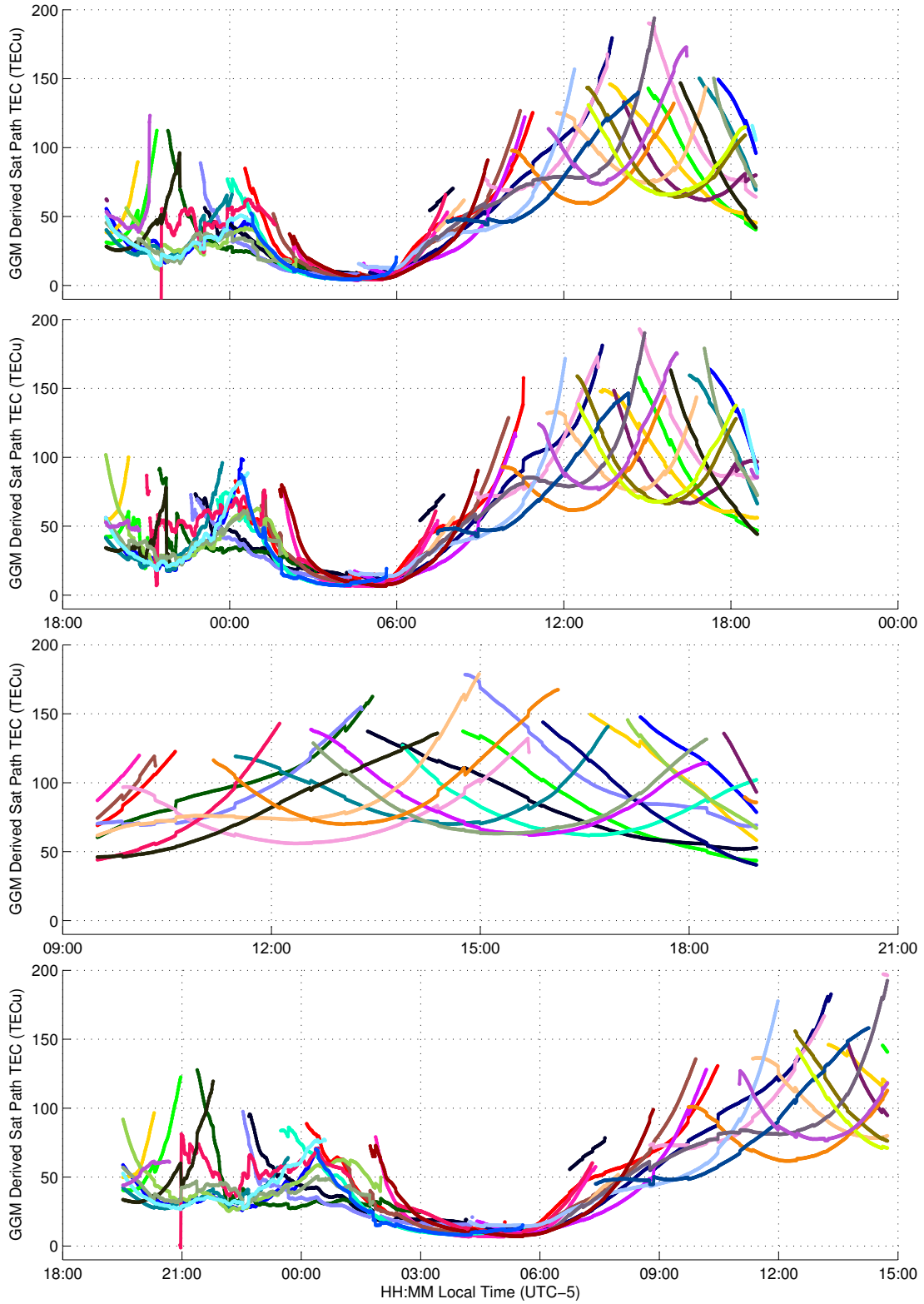
FIGURE 5.13. GGM TEC along satellite signal paths over 24 hours from JRO, March 7, 12, 11, and 13, top to bottom. Each color represents a different satellite.
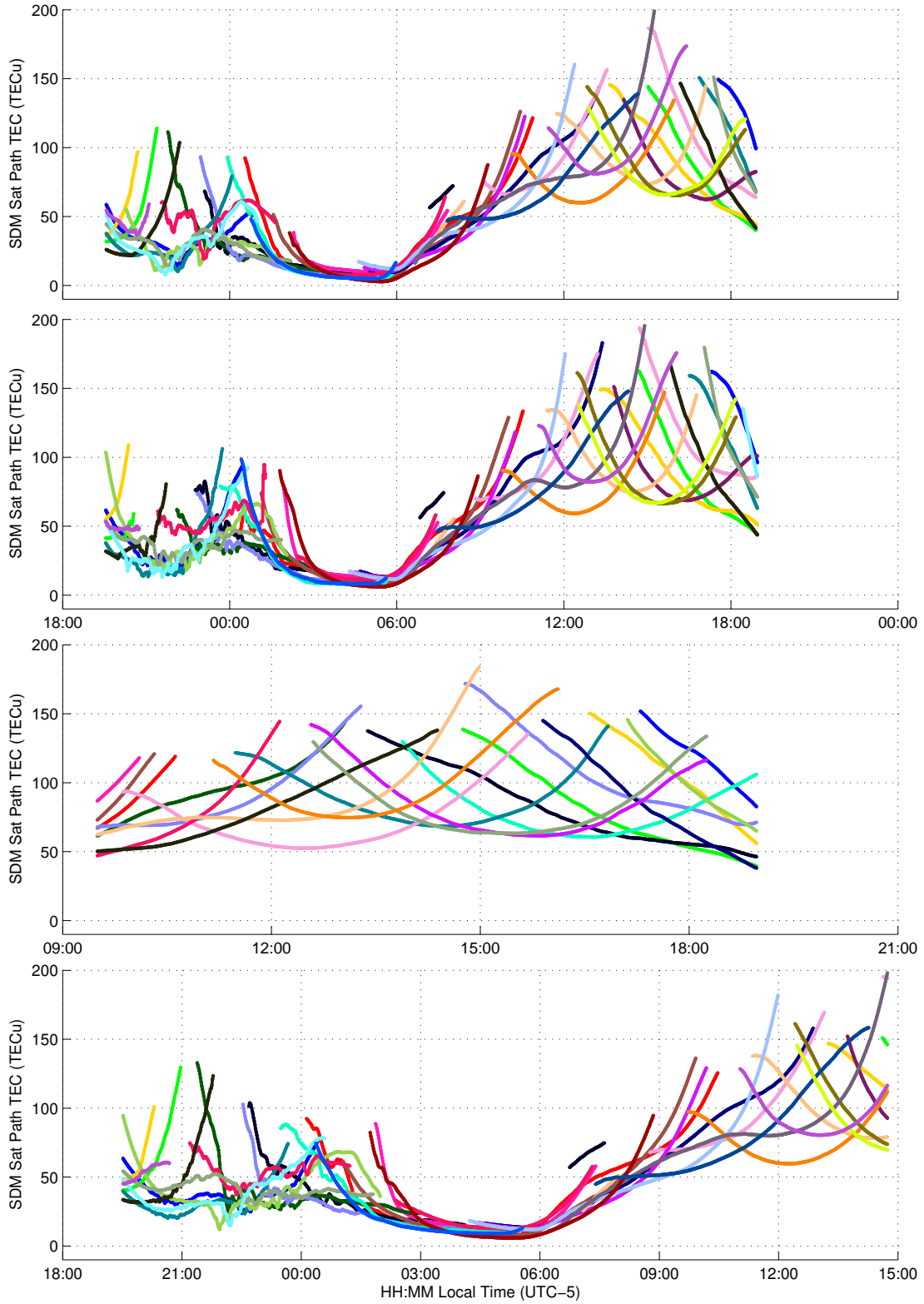
FIGURE 5.14. SDM TEC along satellite signal paths over 24 hours from JRO, March 7, 12, 11, and 13, top to bottom. Each color represents a different satellite.

FIGURE 5.15. SDM-GGM TEC difference along satellite signal paths over 24 hours from JRO, March 7, 12, 11, and 13, top to bottom. Each color represents a different satellite.

FIGURE 5.16. SDM-GGM TEC difference mean & standard deviation along satellite signal paths over 24 hours from JRO, March 7, 12, 11, and 13, top to bottom. Each color represents a different satellite.

FIGURE 5.17. Comparison between GGM and IGS map zenith TEC and latitude and longitude gradients. From JRO, March 7, 12, 11, and 13, top to bottom

CHAPTER 6

Conclusion and Future Work
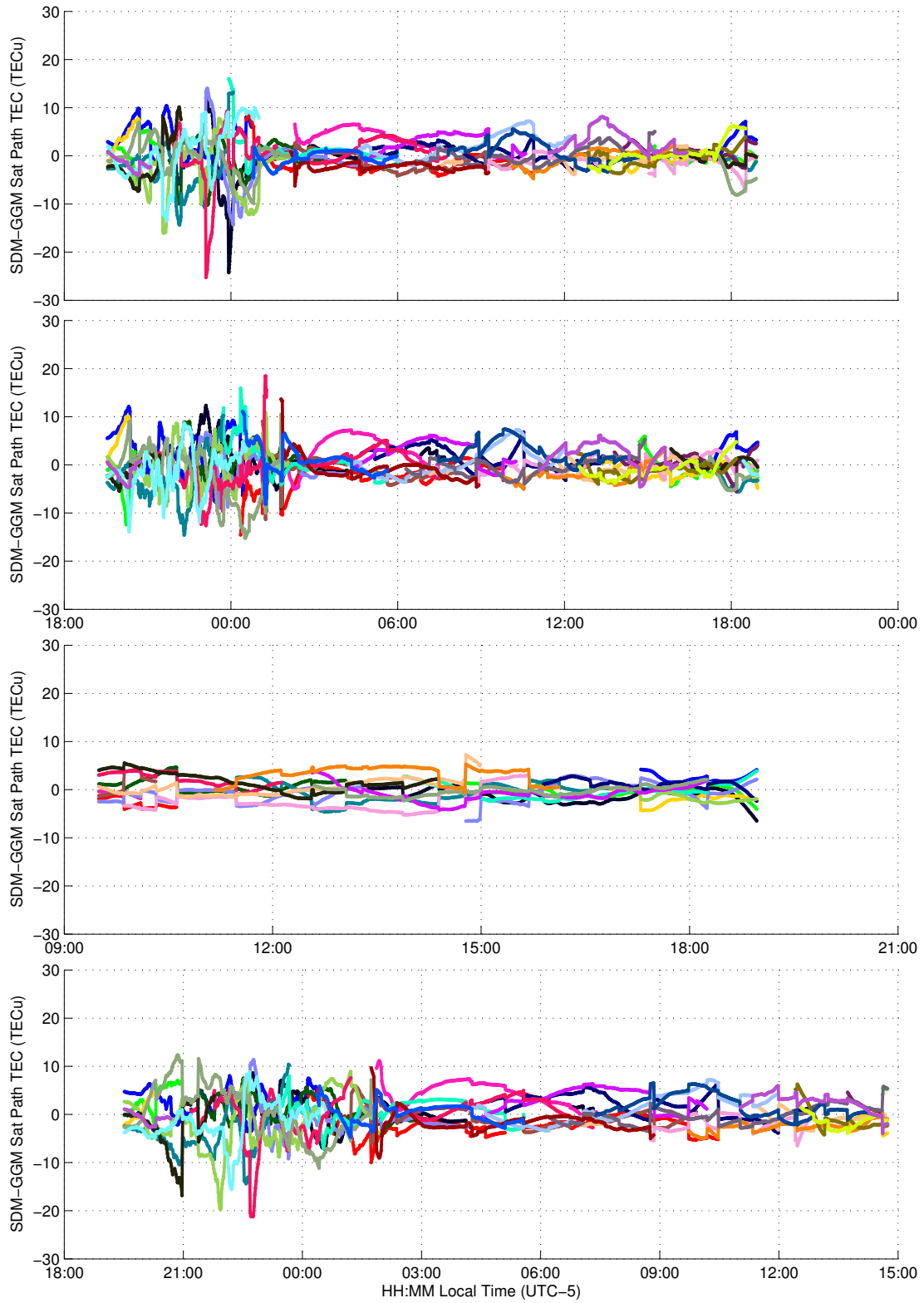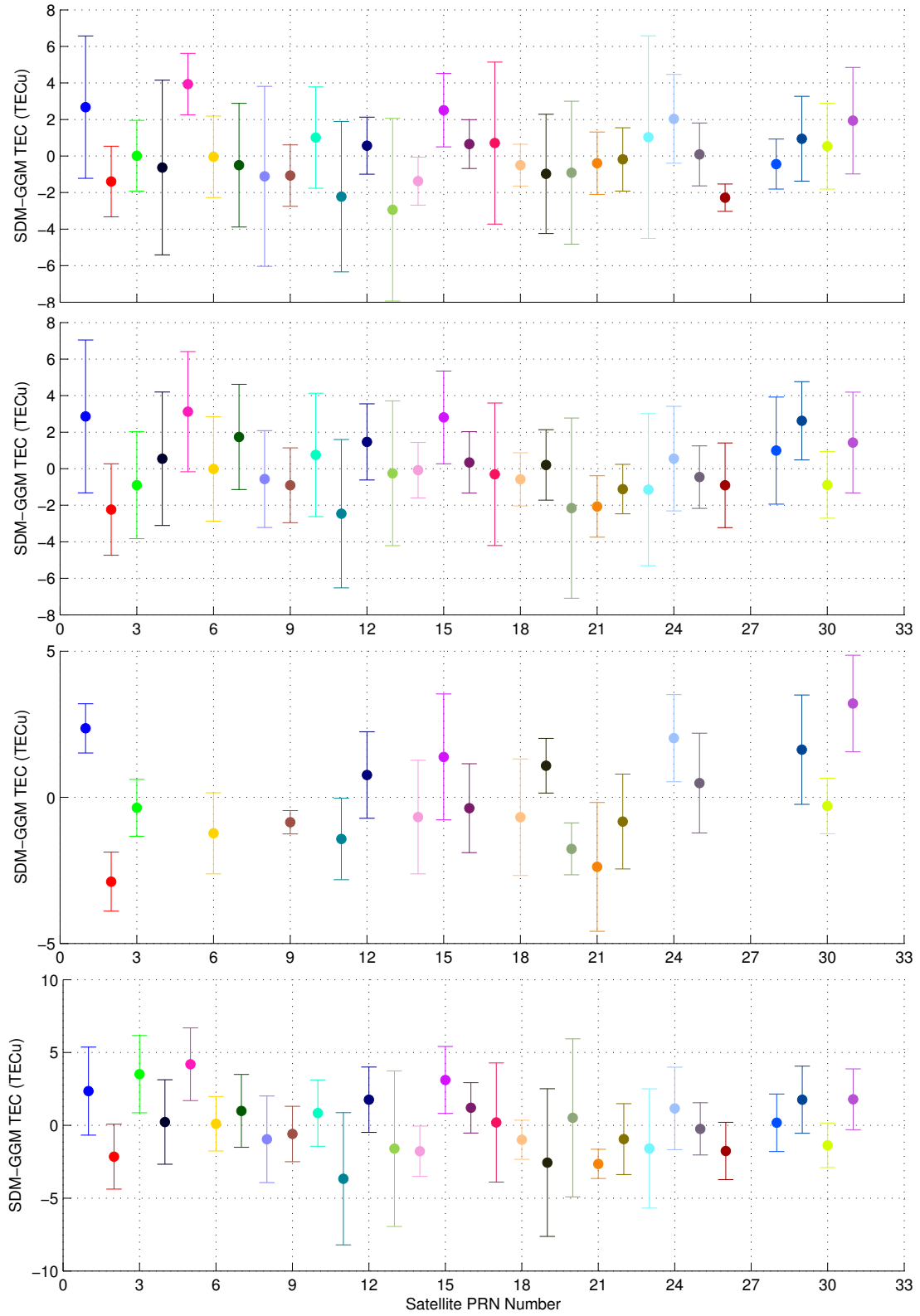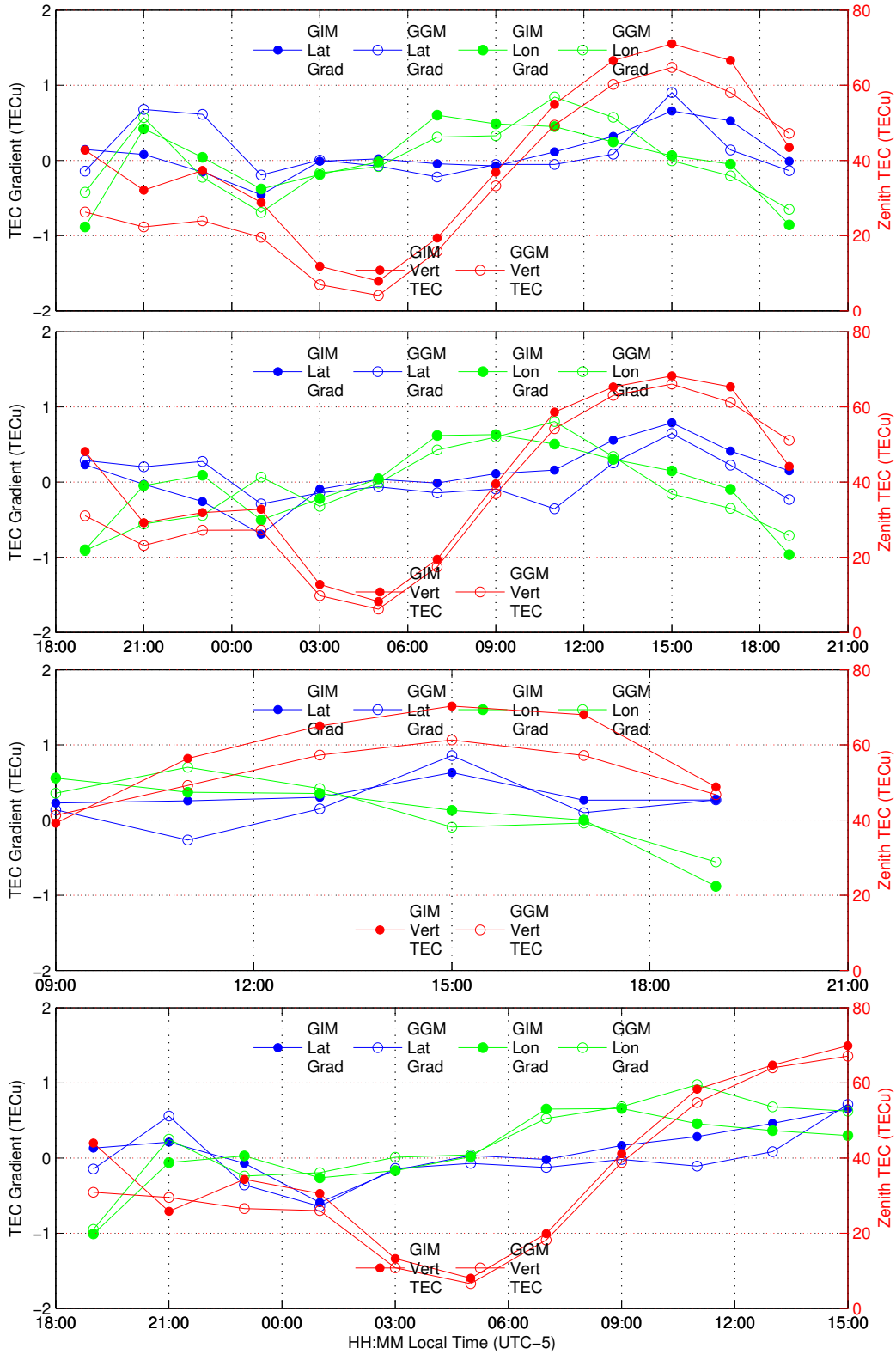
The TEC is an important property of the ionosphere which needs to be measured for use in many communications and remote sensing applications. GPS is a good tool for measuring the ionosphere TEC, as it has global coverage, high temporal resolution, and relatively high spatial resolution. However, GPS based TEC measurements are prone to errors induced by the receiver hardware and multipath, which can be difficult to extract from the measurement. In this thesis a method of mitigating these errors' effect on the TEC estimation was presented, and the corrected TEC was compared to TEC derived from ISR data and GIMs. From the results presented here the following conclusions can be made.

The combination of the CNMP and GGM provides a reasonably accurate estimation of the zenith TEC, and latitude and longitude spatial gradients. However, the method is plagued by spurious fluctuation in the estimate most likely caused by changes in GPS satellite geometry.

Due to the geometry induced fluctuations, it may be preferable to use the IFB estimated as a by-product of the GGM to correct the SDM TEC, instead of using the GGM TEC.

Absolute determination of the accuracy of the method detailed here is difficult, as the GIM is low resolution and uses some modeling, the ISR measurement does not extend high enough, and the SDM TEC must be corrected with the GGM IFB.

To correct the shortcomings of the GGM, as currently implemented, and make a better determination of its effectiveness, significant future work is required.

As discussed in 2.2, determination of the effect of different window lengths on the CNMP estimation is important to insure the best reduction of the multipath contribution. In addition, use of the CNMP bound to weight the corrected measurement to reduce the effect of fluctuations in the measurement, such as those seen in figure 5.10, may provide better results.

The addition of other satellite constellations, such as the Russian GLONASS, may help to reduce the the effect of the satellite geometry on the estimated TEC. Additionally, a larger pool of visible satellites would allow for estimation of higher order spatial derivatives of the TEC. This could make observation of small scale structures possible, and possibly reduce the estimation errors for IPPs further from the receiver.

Additional work is also required to evaluate the GGM TEC over a larger data set. This should include more receiver locations, but more importantly, many more days of data than the few shown here. Because of the relative lack of ISR measurements for longer term comparison, the GIM will have to be the benchmark. GGM TEC should be estimated for atleast a year of data for, at minimum, the three locations used here. This long term study would provide a more statistically significant sense of the GGM performance.

Bibliography

[1] J. Klobuchar, "Ionospheric effects on gps," *Global Positioning System: Theory and applications.*, vol. 1, pp. 485–515, 1996.

[2] S. Jin, J. Park, J. Wang, B. Choi, and P. Park, "Electron density profiles derived from ground-based gps observations," *Journal of Navigation*, vol. 59, pp. 395–401, 9 2006.

[3] M. C. Kelley, *The Earth's Ionosphere: Plasma Physics & Electrodynamics*, vol. 96. Academic press, 2009.

[4] D. Bilitza, "International reference ionosphere 2000," *Radio Science*, vol. 36, no. 2, pp. 261–275, 2001.

[5] E. Kazimirovsky, M. Herraiz, and B. De La Morena, "Effects on the ionosphere due to phenomena occurring below it," *Surveys in Geophysics*, vol. 24, no. 2, pp. 139–184, 2003.

[6] E. L. Afraimovich *et al.*, "A review of gps/glonass studies of the ionospheric response to natural and anthropogenic processes and phenomena," *J. Space Weather Space Clim.*, vol. 3, p. A27, 2013.

[7] E. Calais and J. B. Minster, "Gps detection of ionospheric perturbations following the january 17, 1994, northridge earthquake," *Geophysical Research Letters*, vol. 22, no. 9, pp. 1045–1048, 1995.

[8] J. Artru, V. Ducic, H. Kanamori, P. Lognonn, and M. Murakami, "Ionospheric detection of gravity waves induced by tsunamis," *Geophysical Journal International*, vol. 160, no. 3, pp. 840–848, 2005.

[9] T. Tsugawa, A. Saito, Y. Otsuka, M. Nishioka, T. Maruyama, H. Kato, T. Nagatsuma, and K. Murata, "Ionospheric disturbances detected by gps total electron content observation after the 2011 off the pacific coast of tohoku earthquake," *Earth, Planets and Space*, vol. 63, no. 7, pp. 875–879, 2011.

[10] J. Y. Liu, Y. J. Chuo, S. J. Shan, Y. B. Tsai, Y. I. Chen, S. A. Pulinets, and S. B. Yu, "Pre-earthquake ionospheric anomalies registered by continuous gps tec measurements," *Annales Geophysicae*, vol. 22, no. 5, pp. 1585–1593, 2004.

[11] E. Calais, J. Bernard Minster, M. Hofton, and M. Hedlin, "Ionospheric signature of surface mine blasts from global positioning system measurements," *Geophysical Journal International*, vol. 132, no. 1, pp. 191–202, 1998.

[12] T. Fitzgerald, "Observations of total electron content perturbations on {GPS} signals caused by a ground level explosion," *Journal of Atmospheric and Solar-Terrestrial Physics*, vol. 59, no. 7, pp. 829 – 834, 1997.

[13] H. Dickinson and P. Tamarkin, "Systems for the detection and identification of nuclear explosions in the atmosphere and in space," *Proceedings of the IEEE*, vol. 53, pp. 1921–1934, Dec 1965.

[14] E. Afraimovich, E. Kosogorov, K. Palamarchouk, N. Perevalova, and A. Plotnikov, "The use of gps arrays in detecting the ionospheric response during rocket launchings," *Earth, Planets and Space*, vol. 52, no. 11, pp. 1061–1066, 2000.

[15] E. Calais and J. Bernard Minster, "Gps detection of ionospheric perturbations following a space shuttle ascent," *Geophysical Research Letters*, vol. 23, no. 15, pp. 1897–1900, 1996.

[16] J. Klobuchar, "Ionospheric effects on gps," *Global Positioning System: Theory and applications.*, vol. 1, pp. 485–515, 1996.

[17] P. Misra and P. Enge, *Global Positioning System: Signals, Measurements and Performance Second Edition*. Lincoln, MA: Ganga-Jamuna Press, 2006.

[18] G. Navstar, "Space segment/navigation user interfaces (is-gps-200g)," 2012.

[19] I. C. W. Group *et al.*, "Is-gps-705 revision a: Navstar gps space segment/user segment l5 interfaces."

[20] L. Wanninger, E. Sardon, and R. Warnant, "Determination of the total ionospheric electron content with gps-difficulties and their solution," pp. 13–16, 1994.

[21] R. Warnant, "Reliability of the tec computed using gps measurementsthe problem of hardware biases," *Acta Geodaetica et Geophysica Hungarica*, vol. 32, no. 3-4, pp. 451–459, 1997.

[22] B. Wilson and A. J. Mannucci, "Instrumental biases in ionospheric measurements derived from gps data," 1993.

[23] E. Sardn and N. Zarraoa, "Estimation of total electron content using gps data: How stable are the differential satellite and receiver instrumental biases?," *Radio Science*, vol. 32, no. 5, pp. 1899–1910, 1997.

[24] A. J. Mazzella, "Determinations of plasmasphere electron content from a latitudinal chain of gps stations," *Radio Science*, vol. 47, no. 1, pp. n/a–n/a, 2012. RS1013.

[25] A. J. Mannucci, B. D. Wilson, and C. D. Edwards, "A new method for monitoring the earth's ionospheric total electron content using the gps global network," pp. 1323–1332, 1993.

[26] B. D. Wilson, A. J. Mannucci, and C. D. Edwards, "Sub-daily northern hemisphere ionospheric maps using the igs gps network," 1993.

[27] B. Wilson, A. Mannucci, C. Edwards, and T. Roth, "Global ionospheric maps using a global network of gps receivers," 1992.

[28] F. Arikan, H. Nayir, U. Sezen, and O. Arikan, "Estimation of single station interfrequency receiver bias using gps-tec," *Radio Science*, vol. 43, no. 4, pp. n/a–n/a, 2008. RS4004.

[29] A. Coster, J. Williams, A. Weatherwax, W. Rideout, and D. Herne, "Accuracy of gps total electron content: Gps receiver bias temperature dependence," *Radio Science*, vol. 48, no. 2, pp. 190–196, 2013.

[30] Y. Gao, F. Lahaye, P. Heroux, X. Liao, N. Beck, and M. Olynik, "Modeling and estimation of c1–p1 bias in gps receivers," *Journal of Geodesy*, vol. 74, no. 9, pp. 621–626, 2001.

[31] R. F. Leandro, R. B. Langley, and M. C. Santos, "Estimation of p2-c2 biases by means of precise point positioning," pp. 225–231, 2007.

[32] F. S. K. Xiangyuan, "Gps carrier phase smoothing on code pseudorange based on the hatch filter and its application in point positioning [j]," *Site Investigation Science and Technology*, vol. 4, p. 012, 2007.

[33] B. Park and C. Kee, "Optimal hatch filter with a flexible smoothing window width," pp. 592–602, 2001.

[34] P. J. Teunissen, "The least-squares ambiguity decorrelation adjustment: a method for fast gps integer ambiguity estimation," *Journal of Geodesy*, vol. 70, no. 1-2, pp. 65–82, 1995.

[35] C. Park and P. Teunissen, "A new carrier phase ambiguity estimation for gnss attitude determination systems," vol. 8, 2003.

[36] M. Ge, G. Gendt, M. a. Rothacher, C. Shi, and J. Liu, "Resolution of gps carrier-phase ambiguities in precise point positioning (ppp) with daily observations," *Journal of Geodesy*, vol. 82, no. 7, pp. 389–399, 2008.

[37] K. Shallberg, P. Shloss, E. Altshuler, and L. Tahmazyan, "Waas measurement processing, reducing the effects of multipath," pp. 2334–2340, 2001.

[38] F. Van Graas, "Wide area augmentation system research and development," *Final Report, Prepared under Federal Aviation Administration Research Grant*, 2004.

[39] D. C. Bruckner, F. Van Graas, and T. A. Skidmore, "Algorithm and flight test results to exchange code noise and multipath for biases in dual frequency differential gps for precision approach," *Navigation*, vol. 57, no. 3, pp. 213–228, 2010.

[40] S. Ugazio, F. van Graas, and W. Pelgrum, "Total electron content measurements with uncertainty estimate," in *Satellite Navigation Technologies and European Workshop on GNSS Signals and Signal Processing, (NAVITEC), 2012 6th ESA Workshop on*, pp. 1–8, Dec 2012.

[41] L. Lao-Sheng, "Remote sensing of ionosphere using gps measurements," in *Paper presented at the 22nd Asian Conference on Remote Sensing*, vol. 5, p. 9, 2001.

[42] W. Chen, C. Hu, S. Gao, Y. Chen, X. Ding, and C.-w. K. Simon, "Absolute ionospheric delay estimation based on gps ppp and gps active network," in *2004 International Symposium on GNSS/GPS, Sydney, Australia*, 2004.

[43] N. Jakovvski, E. Sardon, E. Engler, A. Jungstand, and D. Klähn, "Relationships between gps-signal propagation errors and eiscat observations," in *Annales Geophysicae*, vol. 14, pp. 1429–1436, Springer, 1997.

[44] Y. Otsuka, T. Ogawa, A. Saito, T. Tsugawa, S. Fukao, and S. Miyazaki, "A new technique for mapping of total electron content using gps network in japan," *Earth, Planets and Space*, vol. 54, no. 1, pp. 63–70, 2002.

[45] I. Seker, D. Livneh, J. Makela, and J. Mathews, "Tracking f-region plasma depletion bands using gps-tec, incoherent scatter radar, and all-sky imaging at arecibo," *Earth, Planets and Space*, vol. 60, no. 6, pp. 633–646, 2008.

[46] J. J. Makela, S. A. Gonzlez, B. MacPherson, X. Pi, M. C. Kelley, and P. J. Sultan, "Intercomparisons of total electron content measurements using the arecibo incoherent scatter radar and gps," *Geophysical Research Letters*, vol. 27, no. 18, pp. 2841–2844, 2000.

[47] M. J. Nicolls, M. C. Kelley, A. J. Coster, S. A. Gonzlez, and J. J. Makela, "Imaging the structure of a large-scale tid using isr and tec data," *Geophysical Research Letters*, vol. 31, no. 9, pp. n/a–n/a, 2004. L09812.

[48] H. Bourne, Y. Morton, M. Sulzer, M. Milla, and T. Nguyen, "Gps based tec estimation algorithm evaluation using simultaneous incoherent scatter radar measurements," *Proceedings of the ION 2015 Pacific PNT, Honolulu, HI*, pp. 78–84, April 2015.

[49] R. Nikoukar, F. Kamalabadi, E. Kudeki, and M. Sulzer, "An efficient near-optimal approach to incoherent scatter radar parameter estimation," *Radio Science*, vol. 43, no. 5, pp. n/a–n/a, 2008. RS5007.

[50] I. Virtanen, M. Lehtinen, T. Nygrén, M. Orispaa, and J. Vierinen, "Lag profile inversion method for eiscat data analysis," in *Annales geophysicae: atmospheres, hydrospheres and space sciences*, vol. 26, p. 571, 2008.

[51] D. Hysell, F. Rodrigues, J. Chau, and J. Huba, "Full profile incoherent scatter analysis at jicamarca," in *Annales geophysicae: atmospheres, hydrospheres and space sciences*, vol. 26, p. 59, 2008.

[52] D. L. Hysell, "Incoherent scatter experiments at jicamarca using alternating codes," *Radio Science*, vol. 35, no. 6, pp. 1425–1435, 2000.

[53] D. T. Farley, "Incoherent scatter correlation function measurements," *Radio Science*, vol. 4, no. 10, pp. 935–953, 1969.

[54] D. T. Farley, "Faraday rotation measurements using incoherent scatter," *Radio Science*, vol. 4, no. 2, pp. 143–152, 1969.

[55] Astronomical Institute, University of Bern, *Bernese GPS Software Version 5.0*, Jan. 2011. Available at: http://www.bernese.unibe.ch/docs50/DOCU50.pdf.

[56] Astronomical Institute, University of Bern, "AIUB's anonymous ftp server," Nov. 2012.

[57] H. Bourne and Y. Morton, "Gps receiver ionosphere error correction based on spatial gradients and igs satellite dcbs," *Proceedings of the ION 2013 Pacific PNT, Honolulu, HI*, 2013.

[58] S. Schaer, W. Gurtner, and J. Feltens, "Ionex: The ionosphere map exchange format version 1," Feb. 1998. https://igscb.jpl.nasa.gov/igscb/data/format/ionex1.pdf.